LBNL-47196

ERNEST ORLANDO LAWRENCE BERKELEY NATIONAL LABORATORY

Femtosecond Studies of Interband and Intraband Electron Dynamics at Dielectric-Metal Interfaces

Chung Ming Wong

Chemical Sciences Division

December 2000

Ph.D. Thesis

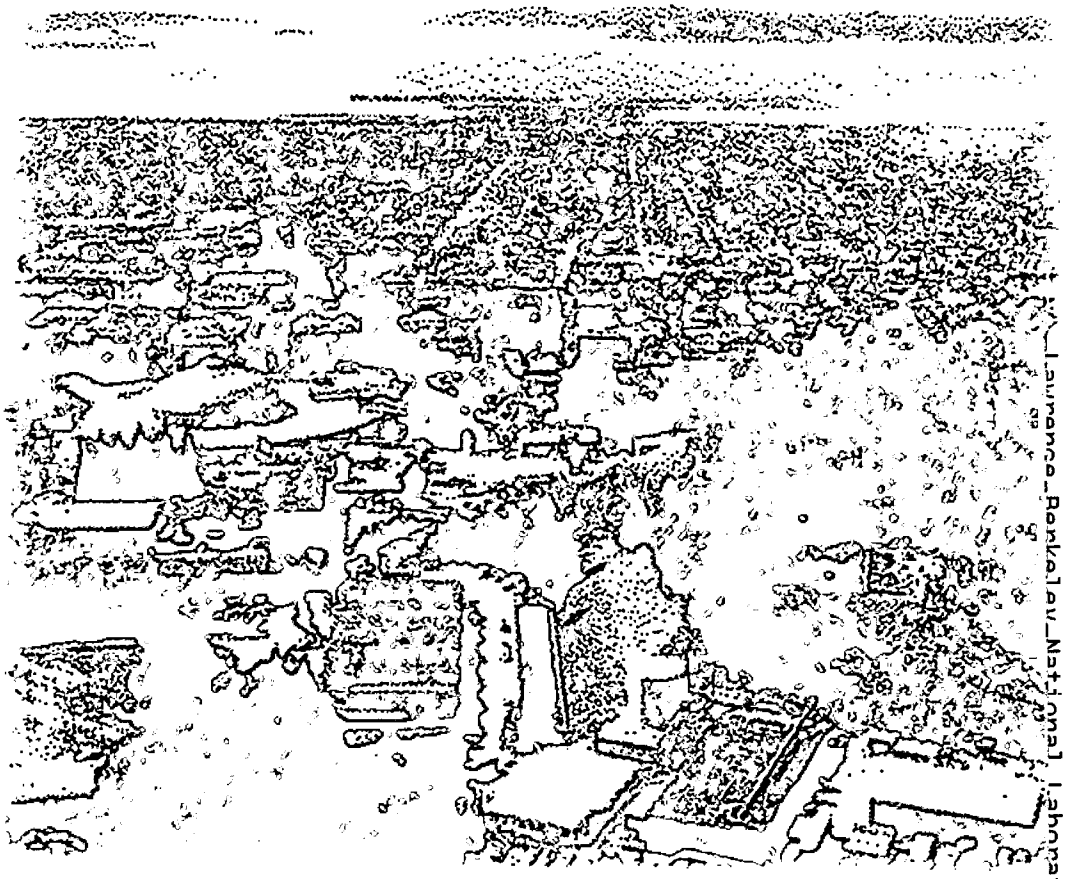

REFERENCE COPY
Does Not
Circulate

LBNL-47196
Copy 1
Annex

DISCLAIMER

This document was prepared as an account of work sponsored by the United States Government. While this document is believed to contain correct information, neither the United States Government nor any agency thereof, nor the Regents of the University of California, nor any of their employees, makes any warranty, express or implied, or assumes any legal responsibility for the accuracy, completeness, or usefulness of any information, apparatus, product, or process disclosed, or represents that its use would not infringe privately owned rights. Reference herein to any specific commercial product, process, or service by its trade name, trademark, manufacturer, or otherwise, does not necessarily constitute or imply its endorsement, recommendation, or favoring by the United States Government or any agency thereof, or the Regents of the University of California. The views and opinions of authors expressed herein do not necessarily state or reflect those of the United States Government or any agency thereof or the Regents of the University of California.

LBNL-47196

Femtosecond Studies of Interband and Intraband Electron Dynamics at Dielectric-Metal Interfaces

Chung Ming Wong
Ph.D. Thesis

Department of Chemistry
University of California, Berkeley

and

Chemical Sciences Division
Ernest Orlando Lawrence Berkeley National Laboratory
University of California
Berkeley, CA 94720

December 2000

This work was supported by the Director, Office of Science, Office of Basic Energy Sciences, Chemical Sciences Division, of the U.S. Department of Energy under Contract No. DE-AC03-76SF00098.

Femtosecond Studies of Interband and Intraband Electron Dynamics at Dielectric-Metal Interfaces

Copyright © 2000

by

Chung Ming Wong

The U.S. Department of Energy has the right to use this document
for any purpose whatsoever including the right to reproduce
all or any part thereof.

Abstract

Femtosecond Studies of Interband and Intraband
Electron Dynamics at Dielectric-Metal Interfaces

By
Chung Ming Wong

Doctor of Philosophy in Chemistry

Department of Chemistry
University of California at Berkeley
Berkeley, California 94720

And

Chemical Sciences Division
E. O. Lawrence Berkeley National Laboratory
University of California
Berkeley, California 94720

Professor Charles B. Harris, Chair

Ultrafast relaxation dynamics of electrons at dielectric-metal interfaces reflect the nature of the electronic interaction with both the substrate and the adsorbed layer. The full understanding of macroscopic electrical transport properties across an interface requires a knowledge of the energies, spatial extents, and scattering lengths of the interfacial electrons. With the femtosecond two-photon photoemission technique, it is possible to directly observe the dynamics of interfacial electrons with specific energy and parallel momentum. Interband and intraband electron relaxation dynamics in excited surface and quantum well states are determined with momentum and time-resolved two-photon photoemission. The study of charge carrier scattering at interfaces and in ultrathin films of Xe on Ag(111) provides a wealth of information on the energy, parallel momentum, and layer thickness dependence of the electron scattering rate. The exclusion of the surface state wavefunction from the interface toward the vacuum by the adsorption of n-

alkane on Ag(111) results in a model system for the study of carrier interactions with the adsorbed layer polarization. The adsorption of these dielectric materials on metal surfaces modifies the interfacial potential and drastically changes the spatial extent of the interfacial electronic wavefunction. The spatial extent of the electronic wavefunction in the direction perpendicular to the interface determines the interband relaxation rate. Oscillations in the interband relaxation time as a function of layer thickness is attributed to a quantum size effect as the higher order image states evolve into quantum well states of the Xe overlayer. The lifetime of the $n = 1$ image surface state shows a strong parallel momentum dependence. This phenomenon is attributed to intraband momentum relaxation. The thickness dependence of intraband relaxation suggests a change in the scattering potential in the direction parallel to the interface for a monolayer, bilayer, and trilayer of Xe. The scattering rate of $n = 2$ increases dramatically after the crossing of the $n = 2$ band into the Ag(111) conduction band. In contrast, image state lifetimes at the n-heptane/Ag(111) interface exhibit an approximately exponential increase as a function of layer thickness. The interband relaxation rate of image electrons at the n-heptane/Ag(111) interface can be modeled with a classical oscillation period. The $n = 1$ dispersion data reveal a spatially localized state, which is attributed to the self-trapping of electrons into a small polaron state at the n-heptane/vacuum junction. Momentum resolved femtosecond two-photon photoemission reveals that electrons initially in the extended image state self-trap into a small polaron within a few hundred femtoseconds.

Contents

1 **Introduction**.....1

2 **Background**.....6

2.1 Image State.....7

2.1.1 Multiple Reflection Theory.....11

2.1.2 Two Band Nearly Free Electron Model.....13

2.2 Image Electron Lifetime.....16

2.3 Two-Photon Photoemission(TPPE).....20

3 **Experimental**.....27

3.1 Time and Angle-Resolved Two-Photon Photoemission Spectroscopy...29

3.2 Sample Preparation.....33

3.3 LEED/Auger Spectrometer.....36

3.4 Turbomolecular Pump System.....40

4 **Electron Dynamics at the Clean Ag(111) Surface**.....46

4.1 Clean Surface Image State Lifetimes.....48

4.2 Classical Oscillation Period.....53

4.3 Image State Electron Wavepacket.....59

4.4 Optical Bloch Equation.....62

5 **Interband Electron Dynamics at Dielectric-Metal Interfaces**.....67

5.1 Dielectric Continuum Approximation.....68

5.2 Interband Electron Dynamics at the n-heptane/Ag(111) Interface.....72

5.3 Interband Electron Dynamics at the Xe/Ag(111) Interface.....81

Two Dimensional Electron Dynamics.....89

6.1 Self-Trapping of Image Electrons.....90

6.2 Intraband Relaxation of Image Electrons at the Xe/Ag(111) Interface..96

6.2.1 Intraband Relaxation Results.....99

6.2.2 Discussion.....106

6.2.3 Electron Scattering Processes.....109

7 Conclusion.....113

List of Figures

2.1 Image electrons and the hydrogenic model....8
2.2 Projected bulk band structure of Ag(111)....10
2.3 Band structure of Ag(100) and Ag(111)....12
2.4 Three step and one step model of photoemission....19
2.5 Symmetry selection rule for photoemission....22
2.6 Schematic diagram of two-photon photoemission....25
3.1 Schematic diagram of the experimental setup....28
3.2 Gaussian instrument function and $n = 1$ dynamics....31
3.3 Growth of Xe on Ag(111)....34
3.4 Auger electron spectroscopy set-up....37
3.5 Auger electron spectrum of clean surface Ag(111)....39
3.6 Turbo pump set-up....41
3.7 Interlock electrical connections....45
4.1 Resonant excitation of higher image states....47
4.2 Dynamics traces of $n \geq 4$ states at various photon energy....49
4.3 Dynamics traces for $n = 1$ to $n = 5$....51
4.4 Schematic diagram of classical oscillations....54
4.5 Logarithmic plot of image state lifetimes....56
4.6 Electron wave packet....60
4.7 Solution to the three-level optical Bloch equation....64
5.1 Dielectric continuum model....69
5.2 Flat potential representation of Xe....71
5.3 Calculated and experimental binding energy for n-heptane....73
5.4 Calculated $n = 1$ wavefunctions for n-heptane....75
5.5 Calculated $n = 2$ wavefunctions for n-heptane....76
5.6 Lifetime of $n = 1$ and $n = 2$ for n-heptane....79
5.7 Calculated and experimental binding energy for Xe....80
5.8 Workfunction change upon adsorption of Xe....82
5.9 Probability densities of image electron at Xe/Ag(111)....83
5.10 Lifetime oscillations at the Xe/Ag(111) interface....85
5.11 Dielectric continuum wavefunction of $n = 1$....87
5.12 One dimensional localization of $n = 1$ in the Xe adlayer....88
6.1 Femtosecond angle-resolved TPPE for n-heptane....91
6.2 Femtosecond time-resolved TPPE for n-heptane....93
6.3 Configuration coordinate diagram for self-trapping....95
6.4 Dynamics of $n = 1$ as a function of parallel momentum....97
6.5 Schematic diagram of intraband relaxation....100
6.6 Linewidth as a function of parallel moment for $n = 1$....102
6.7 Dynamics of $n = 2$ as a function of parallel momentum....103
6.8 Linewidth as a function of parallel moment for $n = 2$....107

List of Tables

4.1 Lifetimes, binding energies of $n = 1$ to $n = 5$ 50
6.1 Momentum resolved $n = 1$ dynamics at Xe/Ag(111) 101
6.2 $\Gamma_{\parallel}$ of $n = 1$ at Xe/Ag(111) 105
6.1 Momentum resolved $n = 2$ dynamics at Xe/Ag(111) 108
6.2 $\Gamma_{\parallel}$ of $n = 2$ at Xe/Ag(111) 108
6.5 Calculated wavefunction overlap for $n = 1$ and $n = 2$ 109

Acknowledgements

I am indebted to many people who made this work possible. Professor Charles B. Harris has taught me the importance of asking big and interesting questions in science and provided me the freedom and the right amount of guidance in conducting independent research. Jason McNeill and Robert Jordan both taught me everything I needed to know about Ultrafast lasers, ultrahigh vacuum systems, data analysis, and computer modeling. They both treated me like a little brother in graduate school. I have worked closely with Nien-Hui Ge and Robert Lingle, Jr. and had many great scientific discussions together. Kelly Gaffney has shared many new and wonderful ideas and provided countless and valuable inputs on all my manuscripts. Simon Liu and André Miller have shown me some new and exciting work that can be accomplished using TPPE. Vijaya Narasimhan helped me with so many administrative problems so that I can concentrate on my research projects. Professor Iu-Yam Chan gave me the first taste of research in Physical Chemistry at Brandeis University.

I would like to thank a number of people who made graduate school both more enjoyable and educational. Haw Yang taught that one should never give up on anything, and I truly take this message to heart. Haw and I had many great discussions together, over our weekend lunches, in all kinds of subject matters. Judy Kim, Melonie Hall, and Travis Taylor all taught me so much about kinetics and are always there whenever I needed a good listener. Michael Tauber never lost his temper when teaching me quantum mechanics. Tim Lian constantly gives me great suggestions and guidance. They are all my lifelong friends.

I would like to thank my parents Kin Han Wong and Jim Siu You Wong for their constant support and encouragement. They often reminded me that I can accomplish anything if I set my mind to it. I would also like to thank my brother Peter Wong, sister Cindy Wong, Anita Lang, and Lenny Chow for being there whenever I needed them. Thank God for creating so much wonderful physics and chemistry for us to enjoy.

This work was supported by the Director, Office of Energy Research, Office of Basic Energy Sciences, and Chemical Sciences Division of the U.S. Department of

Energy, under Contract No. DE-AC03-76SF00098. I would also like to acknowledge National Science Foundation for providing specialized equipment used in some experiments.

Chapter 1

Introduction

Electrons at interfaces provide a unique opportunity to study the importance of reduced dimensionality and spatial extent of surface electronic wavefunctions on carrier dynamics at surfaces and interfaces. Fundamental understanding of the transport properties of electrons at device junctions require the knowledge of electron scattering, relaxation, and recombination processes at surfaces and interfaces. For example, the high mobility of a quantized two-dimensional electron gas at a semiconductor heterojunction is attained by the spatial separation of the electrons from the ionized donors that ultimately reduces electron scattering with the donors[1]. In addition, electron interactions with interfaces govern fundamental aspects of surface chemical and electrochemical processes. The breaking of chemical bonds at surfaces can be induced by electron transfer from the substrate to dissociative states of the surface molecules, which causes fragmentation and/or desorption of adsorbates[2-8]. There are other areas of study in which the interaction of charges with metal-insulator interfaces are important, such as the screening effects of an insulator in ion desorption and the determination of electronic structure of metal-organic device junctions[9,10]. Other active areas of research, such as the study of solar energy conversion with dye-sensitized oxide films, will inevitably require an understanding of electronic interaction at interfaces[11,12].

Xe on a metal surface is a model system for the study of the effects of thin insulating films on a conductor. The structure of a thin Xe film on metal surfaces has been well characterized using X-ray diffraction[13]. The attractive electron affinity of bulk Xe results in quantum well states that confine electrons normal to the surface. Thus, the study of Xe quantum well electron dynamics provides a means for investigating the

effect of quantum confinement on electron transport in a layer-by-layer fashion. The evolution of the electronic wavefunction and the change in the interfacial electron dynamics as a function of layer thickness further elucidate the correlation between the electron relaxation process and the spatial extent of the interfacial electronic state.

Most of the tools in surface science, such as scanning tunneling microscopy, scanning force microscopy, electron energy loss, and Auger emission involve the interaction of electrons with the environment at the surface. These techniques, however, lack the time resolution necessary to directly measure electron dynamics at surfaces and interfaces. The development of femtosecond time-resolved two-photon photoemission (TPPE) spectroscopy and its application to a variety of systems have increased our knowledge of surface electron dynamics. Studies of surface state electrons at metal-dielectric[14], metal-semiconductor[15], and metal-metal[16] interfaces using TPPE have been reviewed. In TPPE spectroscopy, electrons are excited from occupied states of the substrate by a pump pulse into unoccupied surface states and photoemitted from these intermediate states by a probe pulse[16,17]. The photoemission intensity of the unoccupied surface state as a function of time delay between the pump pulse and the probe pulse directly reveals the electron dynamics of the surface state. Early time resolved TPPE studies were mainly focused on semiconductor surfaces, namely Si(111)(2×1) and Ge(111)(2×1), to measure the time decay of antibonding π states[18,19]. This technique combined with angle resolution allows the mapping of the band structure of unoccupied energy bands at interfaces and the study of electron dynamics as a function of electron parallel momentum. Electrons with non-zero parallel momentum exhibit decay pathways that arise from scattering of the electrons with surface defects, phonons, and electrons of the substrate. The scattering rate strongly depends on the electron velocity or momentum in the surface parallel.

Image state electrons can be used as probes of the electronic structure and dynamics at surfaces. The first direct spectroscopic observation of image electrons was accomplished by placing electrons on the surface of liquid helium and by measuring the absorption of microwave radiation which occurs during the transition of a low-order image electron to a higher order image state[20]. Image states are extended states or quasi-free electronic states that exhibit parabolic energy dispersions as a function of the

electron $\boldsymbol{k}$-vector parallel to the surface. At the n-alkane/Ag(111) interface, as will be discussed in Chapter 6, image state electrons become spatially localized in the direction parallel to the surface. This results from the polarization interaction between the electrons and the adsorbed material. Image electrons can also be three-dimensionally localize on Ag islands[21] and two-dimensionally localize on stepped Cu(100)[22]. A spatially localized electron exhibits a flat dispersion, where the energy of the state is constant as a function of $\boldsymbol{k}_{\|}$, and $\boldsymbol{k}_{|}$ in this particular direction is no longer a good quantum number. Angle-resolved femtosecond TPPE results have revealed that an electron initially in an extended image state self-traps into a spatially localized small polaron within a few hundred femtoseconds at the n-alkane/Ag(111) interface[23,24]. The energy dependence of the self-trapping rate has been modeled with a theory analogous to electron transfer theory. Coulomb crystallization on bulk helium[25] and the polaronic transition on a helium film[26] were experimentally observed, while electron localization at thin insulator-metal interfaces remains poorly understood. In addition to the study of the spatial localization process of electrons at interfaces, a series of experiments utilizing time-resolved TPPE have measured hot electron decay[27-32], excited quantum well state lifetimes[33,34], charge carrier dynamics in semiconductors[35,36], coherent oscillations[37,38], and spin-resolved electron relaxation in ferromagnetic systems[39]. These experimental findings have significantly increased our understanding of the importance of the substrate and adsorbate band structure on electron relaxation processes.

Recently, femtosecond TPPE has been widely utilized in the study of hot electron dynamics at crystallographically oriented metal surfaces[27-30] . Thermal relaxation of the electronic distribution had been measured earlier with ultrafast TPPE on amorphous metal samples[31,32]. Absorption of photons at metal surfaces results in a transient non-thermal distribution of electrons, *i.e.* hot electrons. Ogawa *et al.* have recently studied hot electron dynamics at the Cu(100), Cu(110), and Cu(111) surfaces[27]. Their results on the energy dependence of the lifetimes deviate from the Fermi liquid theory for free electron metals. Fermi liquid theory has the functional form of $\tau \propto (E - E_F)^{-2}$ for the relaxation time, where E_F is the Fermi level and E is the energy of the hot electrons with respect to the Fermi level. Their electron-electron scattering calculations, assuming a Thomas-Fermi screening length, gave lifetimes that were a factor of 6 shorter than those

measured. These discrepancies were attributed in part to the *d*-band electrons at about 2 eV below E_F, which can participate in both scattering and screening of hot electrons. Schmuttenmaer *et al.* and Cao *et al.* independently observed similar results on Cu(100)[29]. In addition, the recent development of interferometric time-resolved two-photon photoemission by Ogawa *et al.* provides the opportunity to measure decoherence times of electrons at metal surfaces that occur in tens of femtoseconds[40]. Coherence between the excitation electric field and the optically induced electron-hole polarization may have considerable effects on the experimentally measured dynamics for hot electron lifetimes that are <100 fs. Coherence effects in the optical excitation of metals were recently reviewed by Petek and Ogawa[41]. As mentioned by the authors of the review, coherence effects in the optical excitation of metals in the femtosecond time scale is still a young field of study with many unsettled questions and a number of controversies that remain unresolved.

Femtosecond laser pulses exhibit bandwidths on the order of tens of meV, which are sufficient to excite a coherent superposition of several high quantum number image states($n \geq 4$). The coherent superposition of these states results in wavepackets that oscillate between the image potential barrier and the metal surface barrier. Höfer *et al.* have shown that the electron wavepackets travel more than 200 Å away from the surface and oscillate back and forth in the potential well, which was created by the potential barrier at the surface and the Coulomb potential in the vacuum, with a period of 800 fs at the Cu(100) surface[37]. The photoemission intensity increases as the wavepackets move closer to the surface since the metal substrate provides the necessary momentum for photon absorption. Upon adsorption of CO on the Cu(100) surface, the coherent oscillations diminish. The loss of coherence was attributed to the scattering of the surface electrons with the superlattice of the adsorbed CO molecules[42]. These studies are only a few examples of the fascinating physics that governs the electron dynamics at surfaces and interfaces.

The primary focus of the present work consists of the study of the electronic relaxation processes at metal surfaces in the presence of thin layers of insulating or wide energy gap materials. The ability to grow thin insulating films on metals allows us to determine the change in the electronic properties at the metal-dielectric interface and the

modification of the bare metal surface states upon adsorption of dielectric materials in a layer-by layer fashion. Using femtosecond TPPE, the lifetimes of image states at the Xe/Ag(111) and n-heptane/Ag(111) interfaces were measured. In this dissertation, it will be shown that the perpendicular spatial extent of the electronic wavefunction in the metal substrate determines both the interband relaxation and intraband relaxation rate of surface electrons. Interband relaxation involves the transition of a surface electron to the metal bulk bands. For intraband or momentum relaxation, the Xe overlayer acts merely as a spacer layer, which reduces the interaction of the surface electron with that of the bulk. Factors that influence the spatial extent of the interfacial electronic states include the nature of the interfacial potential barrier and the electronic properties of the two materials comprising the interface. Bulk Xe has a positive(attractive) electron affinity which allows surface state wavefunctions to reside in the Xe layer if the state is energetically above the electron affinity level. Materials with a negative(repulsive) electron affinity such as n-alkanes, however, will exclude the surface state wavefunction from the layer. This ultimately reduces the interaction of the surface electron with both the substrate and the adsorbate. The interaction of the surface electron, in this case, is mainly a polarization interaction with the n-alkane layer at the adsorbate/vacuum junction.

Chapter 2
Background

The binding energy, decay rate, and the two dimensional scattering rate of an electron residing on a surface are primarily governed by the band structure of the crystal for a particular crystallographic face. In the limit where a crystal is infinite, the energy band is continuous. The continuity of the band is broken when N atoms are cut from this hypothetical infinite crystal. The Born-von-Kármán boundary conditions immediately tell us that the continuous allowed band becomes a sequence of N discrete states that are pseudo continuous in the limit of large N. Another important result of a finite crystal is the presence of surfaces that permits quantized surface states to reside in the forbidden energy gap of the crystal. The forbidden energy gap, however, is not a required condition for the existence of surface states. As will be discussed later, surface states that are degenerate with the bulk continuum do exist and are referred to as surface resonances. Surface resonances are broadened by the interaction of the state with those of the bulk states[43]. Historical background and basic surface state theories have been extensively covered in a text by Davison and Stęślicka[44] and in a review article by Memmel[45].

Image states are a class of surface states that arise from the abrupt change in polarizability at an interface. The wavefunction of an image state can be solved in a piece-wise manner. The matching conditions are determined by the logarithmic derivatives of the wavefunction in different parts of the potential. An image state wavefunction is hydrogenic-like in the vacuum while its wavefunction must decay into the substrate. For an image state residing at a clean metal surface, its wavefunction in the metal can be approximated using the two-band nearly free electron(NFE) approximation. In the NFE approximation, one assumes that the potential energy of an electron is small compared with its total energy. Whereas in the tight binding model, the potential energy of an electron is assumed to account for nearly all the total energy, and the allowed

energy bands are narrow compared with the forbidden energy gap. Smith has evaluated wavefunctions for image states by matching at the surface the boundary conditions of an NFE wavefunction in the metal with a hydrogenic-like wavefunction in the vacuum[46]. With this method, it is possible to deduce the wavefunction overlap of the image state electron with the metal, which mainly determines the image state lifetime and the two dimensional scattering rate.

2.1 Image States

An electron near a surface induces an effective image charge of $+\beta q$ by polarizing the substrate as shown in Figure 2.1a. The value of β is determined by the static dielectric constant, ε, of the material and is explicitly equal to $(\varepsilon-1)/(\varepsilon+1)$. For a metal, the assumption of ε equal to infinity can be made, resulting in $\beta = 1$. This elementary electrostatic problem can be solved by the method of images[47,48], in which the electron at a distance z from the surface interacts with a fictitious image charge located at $-z$. This simple charge configuration satisfies all boundary conditions for an electric field in the presence of a perfect conductor and provides a unique solution to Poisson's equation: a $-\frac{1}{4}\left(\frac{q^2}{4\pi\varepsilon_0 z}\right)$ Coulomb potential in SI units. The Coulomb potential gives rise to a series of Rydberg-like bound states that converges toward the vacuum energy, as shown in Figure 2.1b. The wavefunction of an image state electron can be approximated by z times the radial part of the hydrogenic wavefunction scaled for the factor of $\frac{1}{4}$ as shown in the figure. This simplest representation of image state wavefunctions is the so-called hydrogenic approximation. Image states, like all surface states, have a characteristic wavefunction maximum at the surface that renders surface electrons sensitive to changes in the electronic properties at the surface upon adsorption of thin films.

The eigenvalues of image states in the presence of a perfect conductor is exactly $\frac{1}{16}$ the eigenvalues of the hydrogen atom and is given by

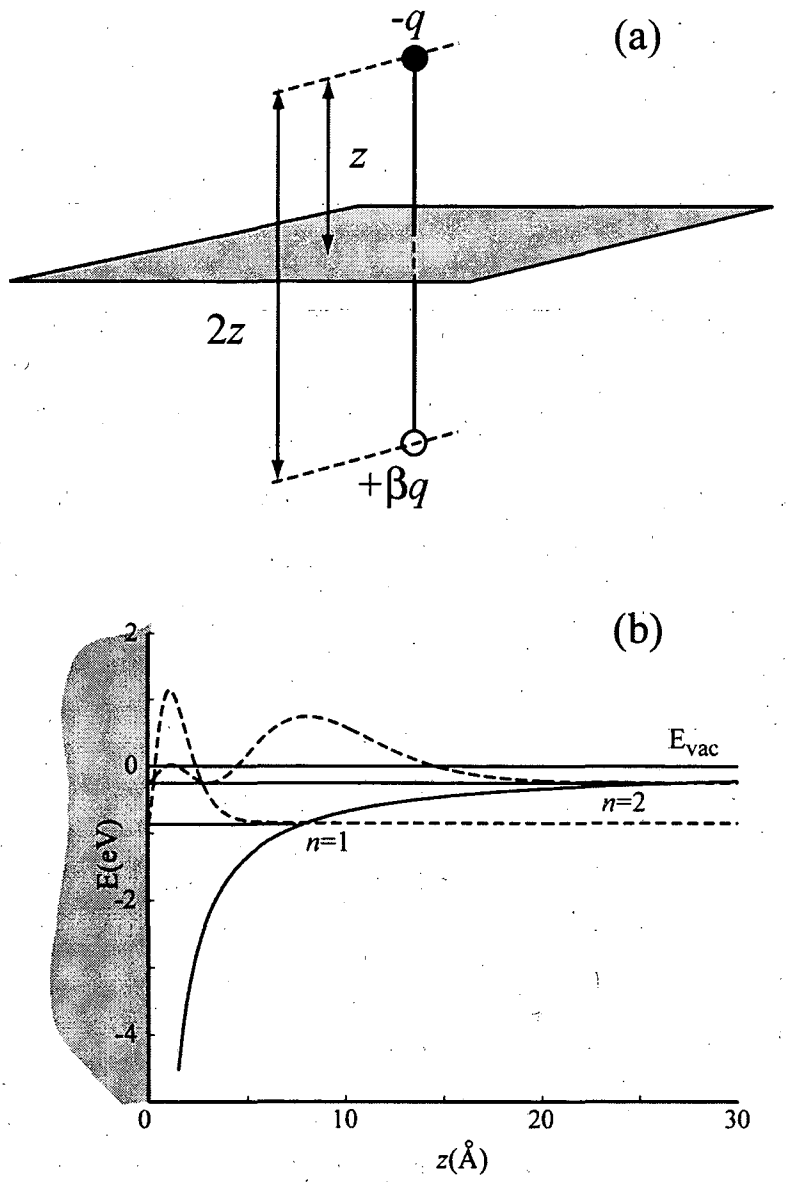

Figure 2.1. (a) An electron near a surface polarizes the material. This induced polarization binds the electron to the surface by forming a potential well that consists of the image potential. The induced polarization can be represented by an image charge that is at an equal distance away from the surface plane as the electron. (b) Solving an analogous 1-D hydrogen atom problem gives rise to Rydberg-like or image states that converge toward the vacuum energy level E_{vac}.

$$E_n = -\frac{1}{16}\frac{m_e e^4}{2n^2\hbar^2} = -\frac{0.85}{n^2}\,\text{eV}, \tag{2.1}$$

where m_e is the free electron mass, e is the elementary charge, and n is the quantum number of the image state whose values are $n = 1, 2, 3,\ldots$ As shown in Figure 2.1b, the maximum of the image state wavefunction is further away from the surface as the quantum number n increases. In the hydrogenic approximation, the expectation value of the image state electron from the surface is $\langle z \rangle = 6a_0 n^2$, where a_0 is the Bohr radius. The location of the wavefunction with respect to the surface normal is an important parameter to consider when we discuss two-dimensional scattering and intraband relaxation of image state electrons.

The surface band structure of a crystal is represented by a projection of the three-dimensional bands in the direction perpendicular to the surface, which is referred to as the projected bulk band structure. This description of the surface bands accounts for the electronic properties of different crystallographic faces. In three dimensions, the crystal band structure is characterized by the band index number and the three-dimensional $\boldsymbol{k}$ vector. In two dimensions, however, the wave vector parallel to the surface $\boldsymbol{k}_{\parallel}$ characterizes the surface band structure. For an ordered surface, $\boldsymbol{k}_{\parallel}$ is a good quantum number and is conserved in the photoemission process as will be discussed later in this chapter. The projected bulk band structure for the L-gap of Ag(111)[49] is shown in Figure 2.2. Projecting the three-dimensional Brillouin zone yields the surface Brillouin zone. The zone center of the surface Brillouin zone is labeled as the symmetry point $\bar{\Gamma}$. In Figure 2.2, the surface state and the $n = 1$ image state are shown. Both of these states reside in the gap near the zone center and disperse from the zone center into the bulk electronic states. The wavefunctions that describe these surface states are factored into two components, namely the perpendicular and the parallel components[50]. The parallel part of the wavefunction is a free-electron-like plane or Bloch wave, since in the parallel direction the periodicity is still retained. The perpendicular part of the wavefunction is an evanescent wave decaying both in the vacuum and in the bulk of the material.

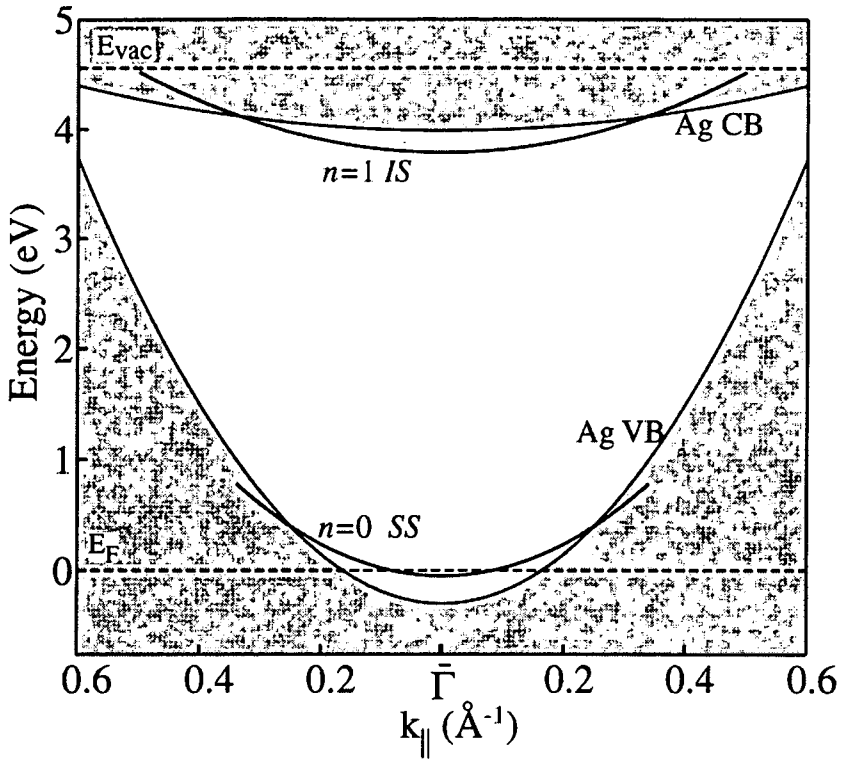

Figure 2.2. Projected bulk band structure of Ag(111). The zone center is labeled as $\bar{\Gamma}$ with increasing $\boldsymbol{k}_{\parallel}$ away from the zone center. CB and VB denote the conduction band and the valence band, respectively. The shaded areas represent possible $\boldsymbol{k}$ states that arise from projecting the 3-dimensional band structure into two dimensions. E_F is the Fermi level and E_{vac} represents the vacuum level. The boundary conditions at the surface allow the surface state(*SS*) and the $n = 1$ image state to reside in the *L*-gap.

2.1.1 Multiple Reflection Theory

As previously mentioned, the hydrogenic model is the simplest model for image states. Its solution is obtained by solving Schrödinger's equation for an analogous one-dimensional hydrogen atom with the wavefunction vanishing at the surface. Because this model assumes that the electron is bound by an infinite potential at the surface, the hydrogenic model is not sensitive to the band structure of a particular crystallographic face. For more realistic metal surfaces, the penetration of the image state wavefunction in the substrate is important in determining the binding energies and decay rate. Image state electrons interact with the many body system of the substrate, which perturbs their motion in the direction parallel to the surface. As a result, image state electrons are quasiparticles with "effective" or "renormalized" masses that are different from that of a bare electron. An elegant description of the effect of the metal surface projected band structure on image state effective mass has been detailed in an account by Giesen *et al.*[51]. Image state binding energies, and effective masses have been determined experimentally by both inverse photoemission and two-photon photoemission[16,52,53]. It has been shown that the (111) crystallographic face of noble metals exhibit higher binding energies for image state electrons than the (100) face[16].

The multiple reflection theory[54] or phase-shift analysis does take into account the effect of the substrate band structure. The image states are represented as plane waves that propagate between the reflecting barriers at the metal crystal band gap and the image potential in the vacuum. Bound states occur when the total accumulation of the phase is $\Phi_c+\Phi_b=2n\pi$, where Φ_c and Φ_b are the phase shifts accumulated at the crystal and image potential barrier, respectively. In the WKB approximation[55], the energy dependence of the phase at the image potential barrier is given by $\Phi_b(E)=(2Z/\sqrt{-2E}-1)\pi$, where E is the energy measured from the vacuum level and Z is equal 1/4 for a conductor. For energy levels near the tail of the image potential or near the vacuum level, Φ_b increases rapidly with energy, yielding a Rydberg-like series that converges toward the vacuum. For image states that appear in a band gap of a metal which is *s-p* inverted, *i.e.* the wavefunction at the conduction band is *s*-like while at the valence band is *p*-like, the phase Φ_c is approximately equal to π when the energy level is close to the

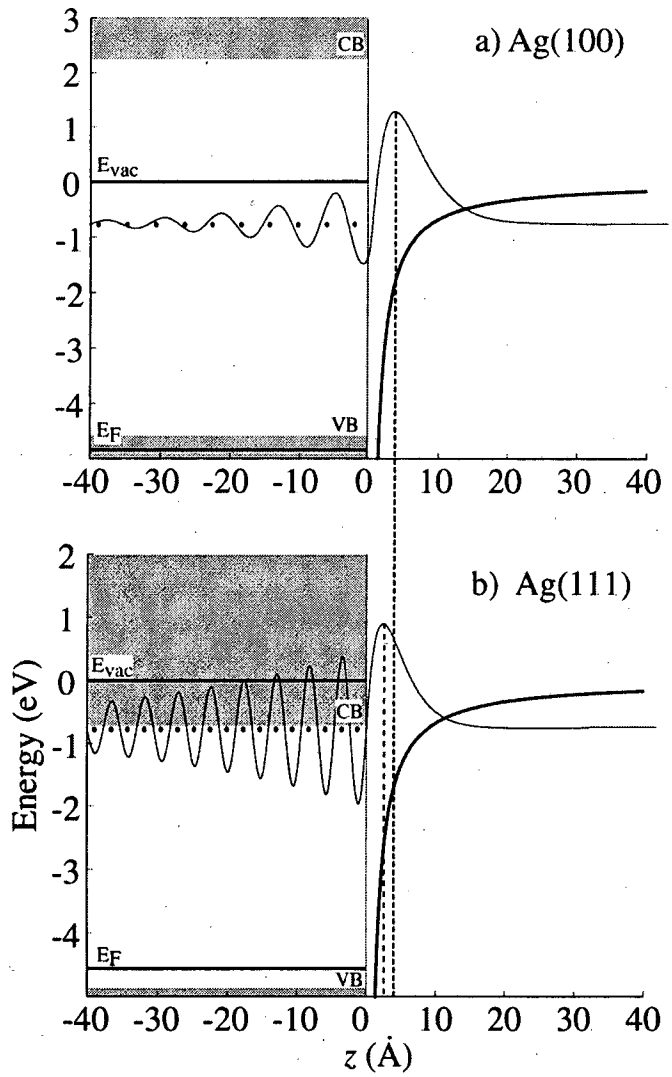

Figure 2.3. Band gap at $k_{\parallel} = 0$ for (a) Ag(100) and (b) Ag(111). The $n = 1$ image state wavefunction at the Ag(111) surface has $\Phi_c = 0.9\pi$, which results in the maximum of the image state electronic wavefunction being closer to the metal and closer to the steep part of the image potential as compared to the electronic wavefunction at Ag(100) where $\Phi_c = 0.5\pi$. The calculated $n = 1$ state binding energies for Ag(111) and Ag(100) are –0.76 and –0.54 eV, respectively. The image potential close to the surface ($z = 0$) is set to a constant to avoid a singularity. The calculated electron probability density in the metal are 0.54 and 0.10 for the Ag(111) and Ag(100) surfaces, respectively. The dots inside the metal represent the position of the silver atoms.

conduction band and 0 when it is near the valence band[16]. The MRT formalism is a way to solve the matching conditions between the substrate wavefunction and the solution to the Coulomb potential in the vacuum. The matching conditions will determine the maximum of the wavefunction in the image potential. When Φ_c is equal to π, the maximum of the wavefunction is closer to the surface and resides in the steep part of the Coulomb potential well. Thus, the image electron will be more bound. For the (111) crystallographic face of noble metals, the vacuum level resides in the conduction band. Since image states converge toward the vacuum level, the phase accumulated at the metal substrate for the image states will be $\Phi_c \cong \pi$, resulting in image states that are more bound for the (111) crystallographic face of noble metals, as shown for the case of $n = 1$ for silver in Figure 2.3[56-58]. The crystal phase shift of $\Phi_c = 0.9\pi$ and $\Phi_c = 0.5\pi$ were calculated for Ag(111) and Ag(100), respectively, by representing the band structure of silver with the two-band nearly-free electron model.

2.1.2 Two Band Nearly Free Electron Model

The two-band nearly-free electron(NFE) model effectively factors in the essential physics that determines the electron wavefunction overlap with the bulk. Maue[59] was the first to use the NFE approximation to study surface states while Goodwin[60,61] made its use more general and prominent. In the effective mass approximation, the one dimensional Schrödinger's equation is given by

$$\left[-\frac{\hbar^2}{2m_\perp^*}\nabla^2 + V(z)\right]\Psi_k(z) = E_k\Psi_k(z), \tag{2.2}$$

where $m_\perp^*$ is the effective mass of the electron moving in the $V(z)$ potential normal to the surface, and $\Psi_k(z) = e^{ikz}u_k(z)$ is the Bloch wave. Since both $V(z)$ and $u_k(z)$ are periodic with the lattice, these functions can be expanded as Fourier series by

$$V(z) = \sum_g V_g e^{2\pi i(b_g z)}, \tag{2.3}$$

$$u_k(z) = \sum_h a_h e^{2\pi i(b_h z)}, \tag{2.4}$$

where V_g and a_h are the expansion coefficients, and b_g and b_h are the reciprocal lattice vectors. Without loss of generality, V_0 can be set to zero. For crystals with inversion symmetry, V_g is equal to V_{-g}. Substitution of Equations 2.3 and 2.4 into Equation 2.2 leads to the following expression[44]:

$$\sum_h e^{2\pi i(b_h z)}\left[a_h[E_k-(k+2\pi b_h)^2-\sum_{g\neq 0}V_g a_{h-g}\right]=0. \tag{2.5}$$

Equation 2.5 is an infinite homogeneous set of equations. The a_h expansion coefficients have non-zero values if the determinant condition is satisfied. If the potential is weak so that V_g's are small, it is reasonable to neglect second order terms in Equation 2.5 and the result is the following equation:

$$a_h[E_k-(k+2\pi b_h)^2]-V_h a_0=0. \tag{2.6}$$

Equation 2.6 leads to the following expression for a_h:

$$a_h=-\frac{1}{4\pi}\left[\frac{V_h}{\pi b_h^2+(b_h k)}\right], \tag{2.7}$$

where $h\neq 0$. The second order energy correction can then be easily determined to be

$$E'=-\frac{1}{4\pi}\sum_{g\neq 0}\frac{|V_g|}{\pi b_g^2+(b_g k)}. \tag{2.8}$$

When the wave vector of the electron is at a Brillouin zone boundary, in which case Bragg reflection of the electron occurs and the denominator of Equation 2.8 is equal to zero, this last equation for the energy correction will no longer be satisfactory. Analogous to solving a degenerate perturbation theory problem[62], Equation 2.5 reduces to the following two equations by setting, respectively, $h = g$ and $h = 0$:

$$a_g\left[E_k-(k+2\pi b_g)^2\right]-V_g a_0=0 \tag{2.9}$$

$$a_0(E_k-k^2)-V_{-g}a_g=0. \tag{2.10}$$

The determinant condition of Equations 2.9 and 2.10 results in the energy as a function of the wave vector and V_g as shown by the following equation:

$$\left[E_k-(k+2\pi b_b)^2\right](E_k-k^2)=\left|V_g\right|^2. \tag{2.11}$$

At the first Brillouin zone boundary where $k = \pi/a$ the roots to Equation 2.11 is given by

$$E^{\pm}=(\pi/a)^2\pm|V_1| \tag{2.12}$$

with their corresponding wavefunctions equal to

$$\Psi^{\pm} = e^{i\pi z/a} \pm (V_1/|V_1|)e^{-i\pi z/a}, \tag{2.13}$$

respectively. Equation 2.12 shows the well-known splitting of the energy bands as a result of Bragg reflections at the zone boundary. It is important to note that the sign of V_1 determines the symmetry of the wavefunction as shown by Equation 2.13. The solution to the bottom of the gap(Ψ^-) is a cosine function(*s*-like) while the solution to the top of the gap(Ψ^+) is a sine function(*p*-like) for a negative V_1. When V_1 is positive, the wavefunctions at the top and bottom of the gap are *p*-like and *s*-like, respectively. For the latter conditions, the forbidden energy gap is described as *s-p* inverted.

As mentioned earlier, the wavefunction of a surface state is an evanescent wave decaying both in the direction of the vacuum and the bulk of a material[50]. In order to satisfy this condition, the wave vector of a surface state wavefunction is assumed to be a complex quantity given by

$$k = \rho + i\eta, \tag{2.14}$$

where ρ and η are the real and imaginary part of the wave vector *k*, respectively. The *s* and *p* characteristics of the wavefunction between the top and bottom of the band imply that a phase factor of $\pi/2$ is introduced to the wavefunction upon crossing the entire gap. In the direction normal to the surface, the wavefunction in the crystal has the following form:

$$\Psi_c(z) = e^{\eta z}\cos(\rho z + \delta), \tag{2.15}$$

where δ is the phase shift upon crossing the gap. Equation 2.15 is a representation of a mixture of $\Psi^{\pm}(z)$ as given by Equation 2.13 with δ being the mixing parameter[44]. Matching the boundary conditions of an incident plane wave with energy *E* to Equation 2.15 results in Φ_c from the MRT analysis of section 2.1.1, as given by the following equation:

$$\Phi_c = 2\arctan\left(\frac{\rho}{\kappa}\tan[\rho z + \delta] - \frac{\eta}{\kappa}\right), \tag{2.16}$$

where κ is the wave vector of the plane wave. The eigenvalues of the image states can be further refined by including a quantum defect parameter which leads to the following expression for the eigenvalues:

$$E_n = -\frac{0.85}{(n+a)^2}\,\text{eV}, \tag{2.17}$$

where a is the quantum defect parameter. The quantum defect parameter is determined by Φ_c and can be calculated using the following equation:

$$a = \frac{1}{2}\left(1 - \frac{\Phi_c}{\pi}\right). \tag{2.18}$$

At the Ag(111) surface $\Phi_c = 0.9\pi$ for $n = 1$, which results in a quantum defect parameter of a=0.05. The binding energy of $n = 1$ from Equation 2.17 is equal to –0.76 eV which is the value determined experimentally by Straub and Himpsel[63]. With Φ_c equal to 0.5π, the quantum defect and binding energy of $n = 1$ on Ag(100) were determined to be 0.25 and -0.54 eV, respectively. This binding energy compares well with the experimentally determined value of $-0.53 \pm 0.02\,\text{eV}$ by Giesen, Hage, Himpsel, Riess, and Steinmann[64].

2.2 Image Electron Lifetime

The primary decay pathway for $\boldsymbol{k}_{\|} = 0$ electrons is via electron-hole pair excitation in the metal substrate for image electrons residing both at the clean metal surface and at the dielectric/metal interface. Under this assumption, the lifetimes scale with the overlap of the wavefunction with the metal[65]. This is an interband relaxation process in which electrons in the image state band decay into the bulk states of the metal. The overlap of the wavefunction P is determined by integrating in the metal substrate the normalized interfacial state wavefunction, which we shall denote as Ψ_n. The integral is written as,

$$P = \int_{-\infty}^{0} \Psi_n^* \Psi_n \, dz\,, \tag{2.19}$$

where n is the quantum number and the limit of integration is from the bulk of the metal at $z = -\infty$ to the surface of the metal at $z = 0$. The interfacial state wavefunction is comprised of a wavefunction in the crystal determined by Equation 2.15 and a hydrogen-like wavefunction in the vacuum. The lifetime broadening linewidth, Γ, of the

interfacial state can be related to the linewidth of the bulk state with the same energy $\Gamma_b(E)$ by setting $\Gamma = P \cdot \Gamma_b(E)$. In the limit where an interfacial state has zero penetration in the metal substrate, the linewidth approaches zero, which indicates an infinitely long lifetime. With proper field settings, image electrons can last for hours on a liquid helium surface where the electron wavefunction cannot penetrate into the bulk helium as a result of the exclusion principle[20]. The linewidth Γ is related to the lifetime τ by $\Gamma \cdot \tau = 660$ meV·fs. Xenon quantum well states and image state lifetimes can be reproduced by theoretical calculations of the lifetimes based on independent photoemission values of $\Gamma_b(E) = 0.13(E\text{-}E_F)$ which were measured by Goldman, Altmann, and Dose for both Ag and Cu[66]. Wolf *et al.* were the first to apply this method to account for the lifetimes of $n = 1$ and 2 for a monolayer of Xe on Cu(111)[67]. Later, McNeill *et al.* applied this method to model the oscillations in the lifetime of $n = 2$ and 3 as a function of Xe layer thickness on Ag(111)[33].

There are two important factors that affect the wavefunction penetration in the metal and therefore affect the interfacial state lifetime. The first factor corresponds to the relative position of the interfacial state with respect to the metal band structure. The penetration increases as the energy approaches the band edges and decreases as the energy is moved closer to the middle of the gap. This is demonstrated by the wavefunction determined for Ag(111) and Ag(100) in Figure 2.3, which shows a significant decrease of the wavefunction probability density in the metal for the Ag(100) $n = 1$ state. The wavefunction probability densities in the metal for Ag(111) and Ag(100) are calculated to be 0.54 and 0.10, respectively. Lifetimes of $n = 1$ and 2 image states have been measured for the Ag(111) and Ag(100) surfaces by Schoenlein *et al.*[68-70] using femtosecond TPPE, and they reflect the wavefunction overlap picture in determining image state lifetimes. It should be noted that their measurements were done at room temperature and with an electron energy detector(cylindrical mirror analyzer) that has a relatively large energy width of 100 meV[68-70]. Both conditions result in a measured lifetime that may be shorter than what we would acquire in our laboratory as will be explained in a later chapter.

Lifetimes for $n = 1$ and 2 were determined to be <20 fs for the Ag(111) surface[70]. The degeneracy of $n = 2$ with the conduction band at the Ag(111) surface

significantly shortens its lifetime[56-58]. The Ag(100) $n = 1$ and 2 lifetimes, however, were determined by the same workers to be 25 ± 10 and 180 ± 20 fs, respectively. It is important to note that intrinsic surface states and the location of the valence band with respect to the Fermi level play significant roles in determining image state lifetimes. For Ag(111), the presence of the surface state introduces an extra decay channel for the image state electrons. The surface state has approximately 40% contribution to the $n = 1$ image state linewidth, as theoretically determined by Chulkov *et al.*[71]. The extension of the Ag(111) band gap below the Fermi level, however, offsets the effect of the surface state by reducing the available phase space for electron decay.

The second factor that affects the wavefunction penetration in the metal is the adsorption of dielectric materials[14]. The addition of layers of dielectric thin films will either push the electronic wavefunction further away from the metal substrate or allow the electron to move into the layer to form a quantum well electron. These processes are governed by the electronic structure of the adsorbed layer, *i.e.* whether the conduction band minimum or the electron affinity level is above or below the energy of the state of interest. At the onset of forming a quantum well state in the layer, the image state lifetime will decrease since the electronic wavefunction is pulled in by the adlayer[33]. The result is a closer wavefunction to the surface and a higher wavefunction overlap with the metal substrate. As the quantum well size increases by growing more layers on the surface, the increase in width allows the electronic wavefunction to spread in the overlayer. The pushing of the electron out toward the vacuum by an adlayer and the spreading of the electron wavefunction inside an overlayer increase the interfacial state lifetime. These effects will be discussed extensively in Chapter 5.

The adsorption of dielectric materials with a negative electron affinity results in the decoupling of the image state electron from the metal substrate. A tunneling model is more appropriate in determining the lifetimes of image state electrons residing at dielectric/metal interfaces where the dielectric material has a negative electron affinity[72]. The electron motion parallel to the interface is governed by the polarization interaction with the dielectric material and results in self-trapping of the initially delocalized image state electrons[23,24]. This self-trapping process inhibits the motion of an image electron in the direction parallel to the surface. The self-trapping of an

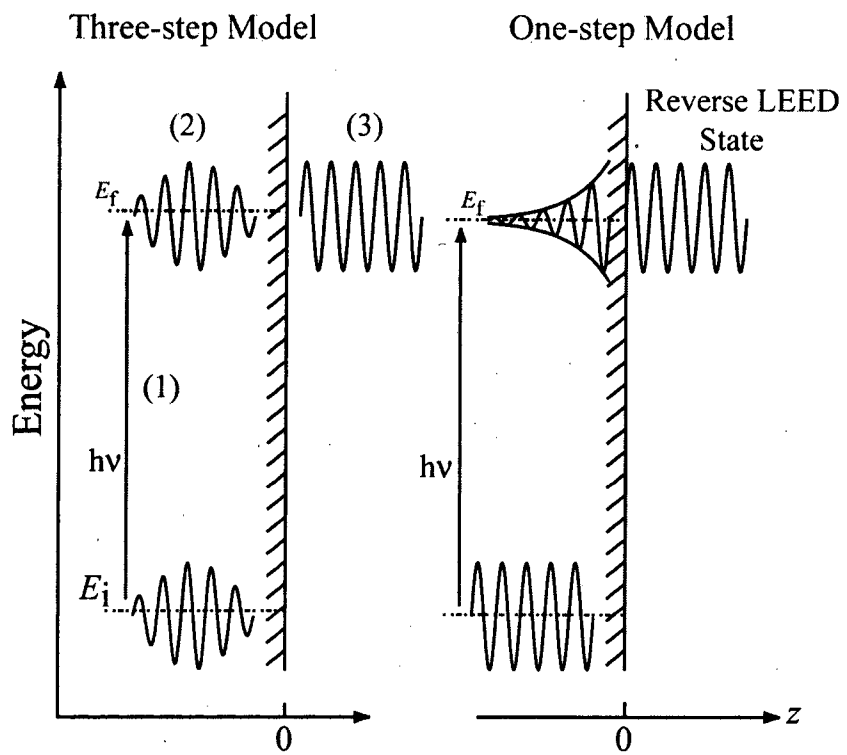

Figure 2.4. Three step model(Left) and one step model(right) of photoemission in solids. In the three step model, step 1 represents the excitation from an initial state(E_i) into a final state(E_f). The last two steps represent the transport of the electron to the surface and finally escaping into the vacuum. In the one step model, the final state is represented as a damped state in the bulk, which accounts for the photoemission yield limited by the mean free path of the electron in the material.

image electron at the n-alkane/metal interface results in the formation of small polarons and will be discussed in the Chapter 6.

2.3 Two-Photon Photoemission(TPPE)

Before two-photon photoemission, inverse photoemission(IPE) was a widely used technique to study the unoccupied image states[52,53]. In IPE, an electron with known kinetic energy(E_i) impinges on a sample. The de-accelerated electron emits a photon whose energy is E_i-E_f, where E_f is the energy of the empty final state which is, in this case, the energy of the image state. Johnson and Smith were one of the first to use IPE to study image potential states on transition metal surfaces[73]. Their use of angle resolved IPE provided the opportunity to distinguish between energy loss satellites and the dispersive image states on the Ni(100) and Cu(100) surfaces. It was Straub and Himpsel[63], however, who later took higher resolution IPE spectra for Cu(100) and Au(100) to rule out the possibility of peaks originating from energy loss satellite peaks, since the image state peaks were shown to be as narrow as a few hundred meV. The narrowness of the image state peaks was restricted by the relatively low resolution of the IPE technique owing to the thermal spread of the incoming electron of about 0.25 eV and the electron energy detector. Straub and Himpsel furthered their investigation of image potential states on the Cu(111), Cu(110), Ag(111), Au(111) metal surfaces, and on the Sb(100) semimetal surface[74].

Image electrons cannot be observed by direct methods such as single-photon photoemission and electron scattering techniques since the electrons are bound in the Coulomb potential and cannot leave the surface. As an aside, it is interesting to note that image states can be observed using STM. Oscillations in the $\frac{dI}{dV}$ versus V STM spectra corresponding to the hydrogenic image-state spectra were observed[75]. Steinmann and co-workers were the early pioneers in using the high resolution two-photon photoemission technique to study image states on noble metal surfaces such as Cu and Ag[76-78]. An excellent account by Fauster and Steinmann has reviewed some of the most important experimental and theoretical studies of image state binding energies and

lifetimes[16]. Image state peaks as narrow as 20 meV have been observed for image states at dielectric/metal interfaces in our laboratory using the TPPE technique along with a time-of-flight electron energy detector[79]. It was Schoenlein *et al.* who later extended the TPPE technique to directly probe image electron dynamics by using femtosecond TPPE[68].

Before discussing the TPPE process, it is helpful to review some of the basic concepts of photoemission[80,81]. Chiang and coworkers have recently used a high resolution photoemission techniques to study metal quantum well states[82-84]. Photoemission in solids can be interpreted using the so-called three-step model as depicted in Figure 2.4. In this model, step 1 represents the excitation of an initial state(E_i) into a final state(E_f). The states are represented as wavepackets to account for the fact that the electromagnetic field has a certain penetration depth. Step 2 represents the transport of the electron to the surface and reaching the surface with energy E_f. Electron scattering mechanisms, mainly electron-electron scattering for metals, reduce the number of photoexcited electrons in reaching the surface. The final step is the escape of the electron into the vacuum. In the one step model, the photoemission process is represented by an excitation from an initial Bloch wave in the crystal into a damped final state. The damped final state is referred to as the reverse LEED state. The mean free path of the electron in the solid determines the damping of the final state wavefunction in the bulk. The transition probability between the initial and the final state is given by Fermi's Golden Rule, which is

$$w_{fi} = \frac{2\pi}{\hbar}\left|\langle f|H^{\text{int}}|i\rangle\right|\delta(E_f - E_i - \hbar\omega). \tag{2.20}$$

The interaction Hamiltonian between an electron and the electromagnetic radiation with the vector potential $\vec{A}$ is written as

$$H^{\text{int}} = \frac{1}{2mc}\left(\vec{A}\cdot\vec{p} + \vec{p}\cdot\vec{A}\right) \approx \frac{e}{m}\vec{A}\cdot\vec{p}. \tag{2.21}$$

Equation 2.20 reveals the importance of the wavefunction overlap between the initial and the final state in determining the photocurrent[85]. According to Equation 2.21 the matrix element has the form $m_{fi} = \frac{e}{m}\langle f|\vec{A}\cdot\vec{p}|i\rangle$, where $\vec{p}$ is the momentum operator.

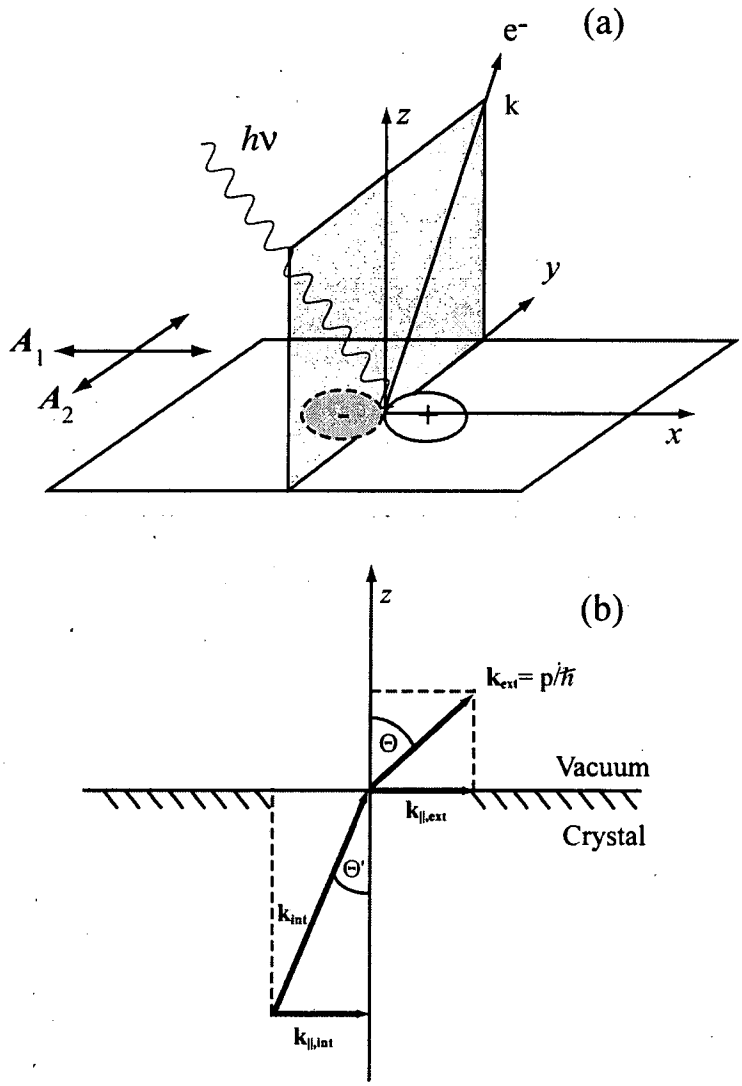

Figure 2.5. (a) Symmetry selection rule for photoemission is shown. The mirror plane is the (yz) plane. (b) The momentum relations at the solid-vacuum interface are shown. The wave vector of the electron in vacuum is denoted as $\boldsymbol{k}_{ext}$, $\boldsymbol{k}_{\|,ext}$ is the parallel component of the photoexcited electron with wave vector $\boldsymbol{k}_{ext}$, and $\boldsymbol{k}_{\|,\mathrm{int}}$ is the parallel momentum of the electron in the bulk. The conservation of parallel momentum requires $\boldsymbol{k}_{\|,\mathrm{int}} = \boldsymbol{k}_{\|,\mathrm{ext}}$.

The experimental geometries and the symmetry of the electronic states involved determine the selection rules of the photoemission process[86]. We assume that the direction of incidence of the exciting light and the detection of the photoemitted electrons are in the mirror plane(yz) as shown in Figure 2.5a. The initial state can be classified as even or odd with respect to the reflection across the mirror plane. In order for electron detection to occur, there cannot be a node in the mirror plane for the final state wavefunction, which restricts the final state to be classified as even with respect to reflection across the mirror plane. In Figure 2.5a, the vector potential can be either perpendicular to the mirror plane $(\vec{A}_1)$ or parallel to the mirror plane $(\vec{A}_2)$. For vector potential $\vec{A}_1$, Equation 2.21 restricts the momentum operator to have a $\partial/\partial x$ component, which is odd with respect to the reflection across the mirror plane. For vector potential $\vec{A}_2$, however, the interaction Hamiltonian will contain both the $\partial/\partial y$ and $\partial/\partial z$ components, which are even functions. In order to detect a photoemission signal, the matrix element cannot be zero, which restricts the integrand of the integral $\langle f|\vec{A}\cdot\vec{p}|i\rangle$ to have an even parity. To obtain photoemission from an initial state with an odd symmetry, excitation light with the $\vec{A}_1$ component must be used. Thus, wavefunctions that are *p*-type oriented along the x-axis, as shown in the figure, will be detected using excitation light with the $\vec{A}_1$ component. The parallel component of the image state wavefunction with respect to the surface is free electron like and is classified as even. Thus, excitation light with the $\vec{A}_2$ component will allow image state electrons to be photoemitted. The readers are referred to a more extensive study by Wolf and co-workers on selection rules and polarization dependence in the photoemission intensity of states with specific symmetries and photoexcitation processes, that is, whether the excitation was direct or indirect[87].

For a well-ordered surface, the momentum component parallel to the surface is conserved during the photoemission process. In the UV regime, the photon momentum is insignificant and the transition is described as a vertical transition. The vertical transition is made possible by the crystal, which can supply momentum equal to $n\hbar G$ to allow electron momentum conservation during the excitation process. Figure 2.5b depicts the

momentum relations at the solid-vacuum interface. In the figure, $\boldsymbol{k}_{ext}$ represents the wave vector of the electron in vacuum, and $\boldsymbol{k}_{\|,\mathrm{ext}}$ is the parallel component of the photoexcited electron with wave vector $\boldsymbol{k}_{ext}$. The conservation of parallel momentum requires $\boldsymbol{k}_{\|,\mathrm{int}} = \boldsymbol{k}_{\|,\mathrm{ext}}$. The figure reflects Snell's law and reveals the momentum components that determine the direction of the photoemitted electron. An equation that can immediately be derived from Figure 2.5b, determines the parallel momentum as a function of angle and measured electron kinetic energy by

$$k_{\|} = \sin\theta\left(\frac{2m}{\hbar^2}E_{kin}\right)^{1/2} = \sin\theta'\left(\frac{2m}{\hbar^2}(E_f - E_i)\right)^{1/2}, \qquad (2.22)$$

where $k_{\|}$ is equivalent to $\boldsymbol{k}_{\|,\mathrm{ext}}$, E_f is the energy of the final state with respect to the energy of the initial state E_i, and E_{kin} is the kinetic energy of the photoemitted electron. The terms in the square roots are similar to the index of refraction in Snell's law. Equation 2.22 shows that the angle of escape is larger outside the crystal than inside. The angle θ in both Equation 2.22 and Figure 2.5 can be varied in our laboratory by changing the angle of the sample with respect to the detector. The dispersion relation in the effective mass approximation is given by

$$E(k_{\|}) = \frac{\hbar^2 k_{\|}^2}{2m^*} + E_0, \qquad (2.23)$$

where m^* is the effective mass of the electron parallel to the surface, and E_0 is the energy of the state at $k_{\|} = 0$. The effective mass of the photoemitting state is readily determined by fitting a parabolic energy dispersion with the measured $E(k_{\|})$. The effective mass is dependent on the coupling of the electron with the material at the interface. For example, the effective mass for the clean surface Ag(111) n = 1 state is about $1.3\,m_e$, as determined by TPPE[51,88]. After dosing four layers of Xe, the effective mass of the n = 1 state decreases to $0.6\,m_e$, which is closer to the bulk Xe value of $0.57\,m_e$ [89]. This indicates that the state does have considerable overlap with the Xe layer. For a localized state, however, the effective mass will be large and results in a non-dispersive state as a function of parallel momentum.

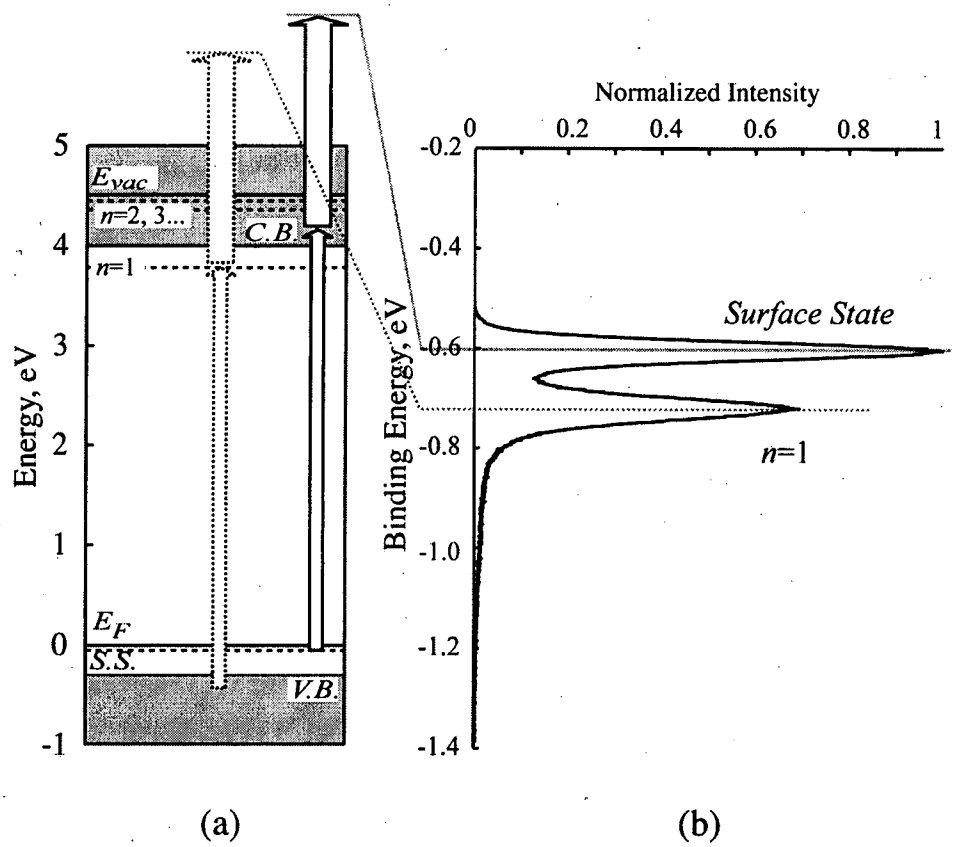

Figure 2.6. Schematic diagram of the TPPE process is shown in (a). The width of the arrow represents the intensity of the pump and probe pulse. Excitation of *S.S.* is through a virtual intermediate state. A static TPPE spectrum taken at 610 nm fundamental is shown in (b).

In TPPE, a pump pulse excites electrons from the bulk below the Fermi level into an image state(Figure 2.6). The photoemission intensity from the image state as a function of time delay between the pump pulse and the probe pulse directly reveals the electron dynamics of an image state. It is advantageous to use two-color TPPE to distinguish between the pumping and the probing process. With two-color TPPE, it is also possible to reduce background signal and eliminate space charge broadening, while maintaining a high electron count by reducing the intensity of the pump pulse and increasing the intensity of the probe pulse. In monochromatic TPPE, the signal is proportional to $I^2(\hbar\omega)$, where I is the intensity of the laser at $\hbar\omega$. In bichromatic TPPE, the signal is proportional to $I(\hbar\omega_1)\times I(\hbar\omega_2)$, where $\hbar\omega_1$ represents the pump photon and $\hbar\omega_2$ represents the probe photon energy[16]. Space charge broadening can be reduced to a minimum by decreasing the intensity of the pump pulse $I(\hbar\omega_1)$ while the signal can be kept constant by increasing the intensity of the probe pulse $I(\hbar\omega_2)$. Frequency doubling of visible light is especially suited for exciting electrons from bulk occupied and occupied surface states into image states residing at noble metal surfaces with work functions of about 5 eV. The residual fundamental can be used as the probe pulse. The intensity of the pump pulse is automatically reduced due to the low doubling efficiency. In Figure 2.6, the fundamental photon energy is about 2 eV(610 nm). The width of the arrows represents the intensity of the pump and the probe pulse. Excitation from the occupied surface state is a coherent two-photon absorption through a virtual intermediate state. The instrument function can be determined from the surface state dynamics as will be discussed in the next chapter.

Chapter 3
Experimental

The experimental results presented in this thesis were acquired using an optical parametric amplifier(OPA) that was pumped by an 800nm Ti:sapphire regenerative amplifier seeded by a Ti:sapphire oscillator. The Ag(111) sample is wedged by 9.4° on a manipulator, which has an angular range between ±12°. The wedging of the sample provides a higher angle of about 21° for the study of angle and time resolved photoemission. This higher angle is important in the study of electron localization at the n-heptane/Ag(111) interface as will be discussed later in Chapter 6. The time-of-flight electron energy detector has been described in detail in Walt Merry's thesis[90]. The energy resolution is limited by the error in the path length Δl traveled by the electron and the error Δt in the flight time. Due to these limitations, the resulting resolution of our energy detector is about 20 meV for electrons with kinetic energy of about 1 eV. As mentioned earlier, features as narrow as 20 meV have been observed for a monolayer of Xe/Ag(111)[79]. This is an important comparison to the experimental setup of Steinmann and co-workers where their smallest energy width is about twice our energy resolution[16]. With our energy resolution, we can easily resolve $n = 1$ to 4, which is important in determining the shape of the potential that results from the adsorption of materials on surfaces. With a new turbo pump system and LEED/Auger electron spectroscopy, both sample cleanliness and characterization have been tremendously improved in the past few years. In this chapter, we will discuss the angle-resolved femtosecond TPPE experimental technique. First, an overview of the laser system along with some important measurements of the autocorrelation and bandwidths of each laser components will be given. Then the new LEED/Auger electronics and setup will be described. Finally, the last section of this chapter will detail the recently installed turbo pump setup and its interlock system.

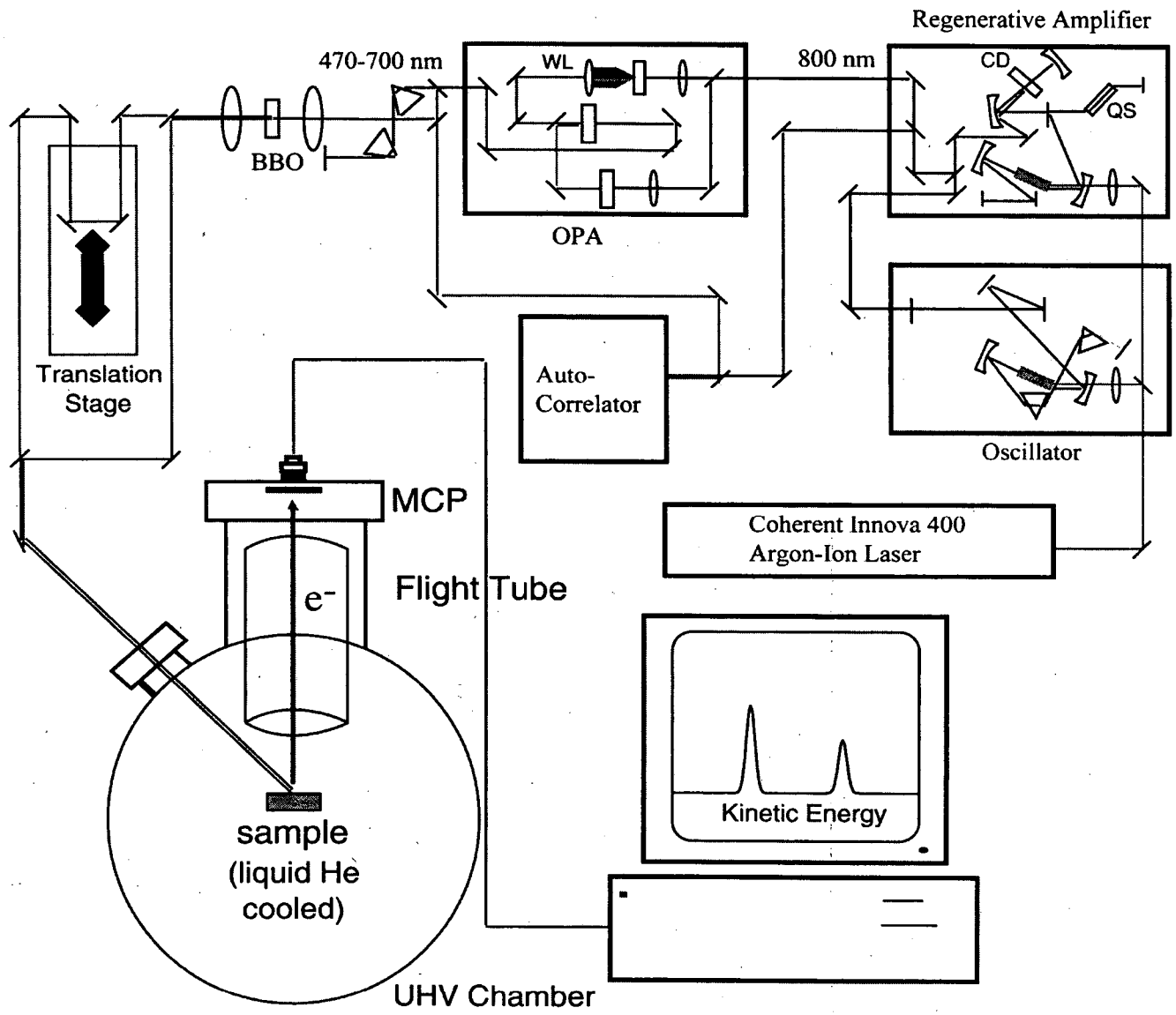

Figure 3.1. Schematic diagram of the experimental setup.

3.1 Time and Angle-Resolved Two-Photon Photoemission Spectroscopy

A schematic diagram of the time and angle resolve TPPE experimental setup is shown in Figure 3.1. The laser system consists of an Ar-ion laser, a Ti:Sapphire Oscillator, a Ti:Sapphire regenerative amplifier[91], and an optical parametric amplifier(OPA)[92]. The Coherent Innova 400 Ar-ion laser operates at around 48 Amps in multi-line mode with an output power of 22 Watt. About 37% of the Ar-ion power is split off to pump the Coherent Mira 900-F Ti:Sapphire oscillator, and 63% of the power is used to pump the Coherent RegA 9000 Ti:Sapphire regenerative amplifier. The Innova 400 Ar-ion laser is equipped with PowerTrack that provides a servo-controlled alignment mechanism for the output coupler to maximize the output power. The laser is set on light regulation mode in which the laser will attempt to maintain the user set output power by varying the current.

The use of Ti:Sapphire as a gain medium allows the Coherent Mira 900-F oscillator to have tunable wavelength ranging from 710 to 1000 nm. The wavelength to be amplified is restricted mainly by a birefringent filter and is currently set to pass 800 nm. The bandwidth of the oscillator fitted to a Gaussian must be between 9 to 12 nm centered at 800 nm in order to obtain the shortest laser pulses throughout the rest of the laser system. The oscillator is passively mode locked via Kerr Lens Modelocking. The index of refraction of the Ti:Sapphire crystal is altered by the intense laser pulse which causes a focusing of the pulse. The intensity of the laser beam profile is less intense at its edges as compared to the center. This results in a gradient index lens or a Kerr lens. It is this mechanism that causes the mode locked pulse to have a smaller spatial profile. The more focused pulse can then pass through a slit while the continuous wave is blocked. The repetition rate of the oscillator is 76Mhz with an output power of 1.2 W mode locked. The autocorrelation of the oscillator is 198 fs with a width of 140 fs. Before the light is injected into the regenerative amplifier, the Mira power is reduced to about 380mW mode locked power. The regenerative amplifier operates optimally at 200 kHz with wavelength centered at 800nm. A cubic polarizer in the amplifier further reduces

the Mira power to about 70mW before the light is injected into the cavity of the amplifier. The input beam from the Mira then passes through a Faraday Isolator and a single pulse is injected into the amplifier by a SiO_2 cavity dumper. The injected pulse passes through 20 to 30 round trips in the amplifier cavity and acquires an amplification of a few hundred times. The TeO_2 Q-switch stretches out the pulse to about 30 ps during amplification. Group velocity dispersion compensation with a single holographic grating in a 4-pass configuration compresses the pulse width to 260 fs. Without the seed pulse from the Mira and with the cavity dumper off in the regenerative amplifier, the cavity CW power that leaks out from the first end mirror should be between 2.4 to 2.6 W. Further detail is found in the Coherent laser manuals in our laboratory. The CW dumped power can be as high as 1.3 to 1.5 W if the cavity dumper alignment is optimized. The output power from the regenerative amplifier should be higher than 730 mW at 200 kHz repetition rate in order to generate enough second harmonics in the OPA.

Inside the OPA, the 800 nm light from the regenerative amplifier is split evenly in power. The OPA uses half of the 800 nm beam to generate a white light continuum and the other half to generate 400 nm second harmonic. The second harmonic power at 200 kHz should be at least 150 mW in order to obtain a sufficiently stable OPA output of the visible light. The second harmonic power is affected by both the output power and the pulse width of the 800 nm light from the regenerative amplifier and the spatial mode of the laser pulse. The white light is generated with a Sapphire crystal and the resulting light has a range of wavelengths between 460 nm to 1200 nm. Through optical mixing in a second BBO crystal, it is possible for two beams with different frequencies to generate a third beam at the difference or the sum frequency. The outcome of the optical mixing results in two new wavelengths that are termed the signal wave and the idler wave. By rotating the BBO mixing crystal, the signal wavelength can be tuned from 500 nm to 700 nm and the idler simultaneously varies from 2000 nm to 933 nm. The autocorrelation of the signal wave after dispersion compensation is about 100 fs. At 600 nm, the measured output power of the signal wave is approximately 20 mW that corresponds to around 100 nJ per pulse. The signal wave is frequency doubled through a BBO crystal and the UV pump and visible probe are separated with one millimeter thick dichroic mirrors to minimize pulse broadening. The probe pulse traverses through a translation stage to

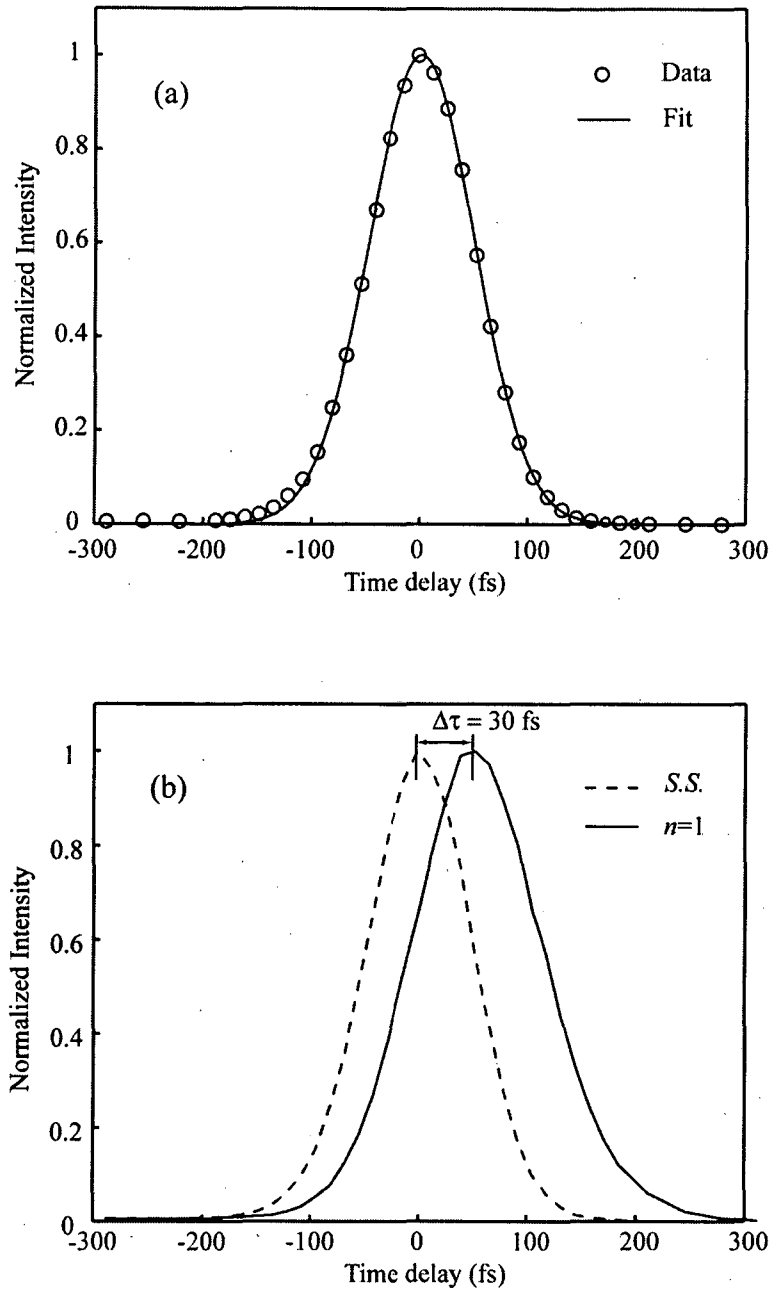

Figure 3.2. (a) Instrument function obtained from the dynamics of *S.S.* The fit to the dynamics is a Gaussian function with a width of 115 fs. The wavelengths of the pump and probe pulses are 300 nm and 600 nm, respectively. (b) The dynamics of the $n = 1$ image state is plotted along with the Gaussian instrument function. The delay in the excited population of $n = 1$ ($\Delta\tau$) is about 30 fs.

acquire a time delay. The stage has a minimum step size of 1μm, which corresponds to a time delay of 6.6 fs after double passing, as shown in Figure 3.1. Finally, the pump and the probe pulses are spatially overlapped onto the sample in the ultrahigh vacuum chamber.

The instrument function is determined most accurately by fitting the dynamics of the occupied surface state denoted as *S.S.* in Figure 2.6. Assuming that the dephasing of the photon-induced electronic polarization is short compared to the pulse width, a cross correlation of the UV-visible pulses can be derived from this state since excitation from this state is a coherent two-photon absorption through a virtual intermediate state. This process is revealed in Figure 2.6 for 610nm fundamental light. At a wavelength of about 540nm, it is not possible to determined the instrument function using this procedure due to the resonant excitation from the surface state to the higher order image states($n \geq 3$). The dynamics of the surface state fits extremely well to a Gaussian function with a width of 115 fs as shown in Figure 3.2a for a 300 nm pump and 600 nm probe pulses. With a direct determination of t_0 (time delay at which the UV and the visible pulses are directly overlapped) and the Gaussian instrument function, it is possible to fit the measured kinetic traces to a convolution of the Gaussian instrument function with exponential decay functions to determine lifetimes that are considerably shorter than the instrument function. The lifetime of $n = 1$ is determined to be 36 ± 8 fs. The normalized dynamics trace of $n = 1$ is shown in Figure 3.2b, which reveals that the $n = 1$ state has a considerable time delay in its dynamics with respect to the instrument function. The shift in the maximum of the excited state population is $\Delta\tau = 30$ fs. The origin of the shift can be explained as coherence effects or intraband relaxation of the image state electrons and will be discussed in Chapter 4. Whether the coherence effect or the intraband relaxation dominates the image state dynamics remains a controversy at the time of writing[41].

3.2 Sample Preparation

In order to obtain a well-ordered and clean sample, the Ag(111) surface was sputtered with Ar^+ at 500 K for 20 minutes and annealed at 725 K for another 20 minutes before an experimental run. The pressure of the Ar gas was maintained at 5×10^{-5} Torr uncorrected pressure reading during the sputtering process. The process of growing Xe on Ag(111) requires the use of high-purity gas and an ultrahigh vacuum (UHV) chamber to minimize contamination of the layer. The sample was cooled by a liquid helium cryostat to temperatures as low as 45 K. The UHV chamber background pressure was less than 1×10^{-10} Torr. Xenon grows in a layer-by-layer fashion on the Ag(111) surface(Figure 3.3). Layers can be grown by back filling the chamber with Xe gas at pressures and sample temperatures specified by the phase diagram of Xe on Ag(111)[93]. At a Xe pressure of about 2×10^{-6} Torr and at temperatures between 82 and 68 K, a monolayer of Xe forms, while at temperatures between 67 and 66 K, a bilayer forms. Xenon layers were grown by metered dosing of the cooled sample at 70 K for a monolayer and at 45 K for multilayers. The number of layers was determined by using TPPE spectroscopy. As the layer grows on the surface, patches of the adsorbate form. The workfunction change from the adsorption process is local to these patches[94]. Steinman, Fauster, and coworkers used the fact that image state binding energies are pinned to the local workfunction to observe the growth mode of Ag, Au, and Co on Cu(111) and Pd(111)[95-97], where they also studied the evolution of metallic quantum wells for Au on Pd(111)[96]. The adsorption of Xe changes the workfunction Φ at the metal surface. The workfunction shift $\Delta\Phi$ was accurately determined by analyzing the convergence of the image state series to the vacuum level using the quantum defect formula as shown in Equation 2.17. The binding energies of the image states with respect to the vacuum level can be determined by solving the quantum defect parameter a for the image state series. We observed most of the workfunction change in our TPPE spectra for the first layer($\Delta\Phi$ = -0.5 eV) with a small shift for the second layer($\Delta\Phi$=-0.04 eV) and no experimentally discernible shift for the third layer.

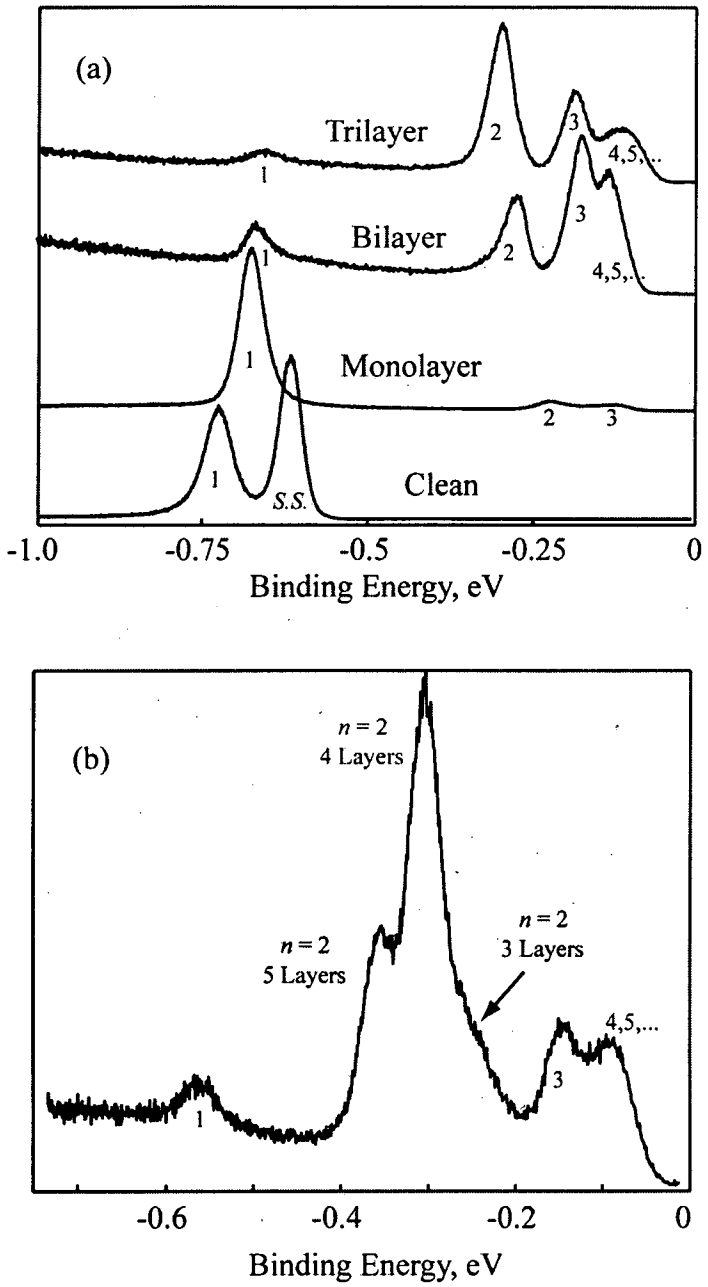

Figure 3.3. (a) Layer-by-layer growth of Xe on Ag(111) is shown. The image state quantum numbers are labeled beneath the features corresponding to the states. *S.S.* is the occupied surface state. (b) The $n = 2$ state is shown after an attempt to grow four layers of Xe. This spectrum reveals that patches with different layer thickness are interspersed on the surface with four-layers being the dominant coverage.

Static TPPE spectra taken with 610nm fundamental at different coverage of Xe on Ag(111) are shown in Figure 3.3a. As the dosage increases, a new peak corresponding to an image state of the newly grown layer becomes prominent. The surface state feature is no longer discernible after a layer of Xe is grown on the clean surface. The surface state is occupied at the Ag(111) surface since it resides below the Fermi level at the zone center. Its wavefunction is also within a few Angströms away from the surface. After growing a layer of Xe onto the surface, the surface state is pushed up in energy by quantum confinement and is no longer occupied. The binding energy of $n = 1$ decreases with layer thickness. The intensity of the $n = 1$ state decreases as its wavefunction is pushed out toward the vacuum, which causes a decrease in the wavefunction overlap between the image state and the initial bulk state. This decreases the transition probability in the excitation step. On the other hand, the binding energy of $n \geq 2$ increases as the states move into the Xe layer to form quantum well states. Both the workfunction shift and the change in the binding energy of the image states can be observed and allow the characterization of the coverage. The higher order image states cannot be populated with 305 nm pump pulse on the clean surface until a layer of Xe lowers the workfunction to about 4.06 eV. Peaks corresponding to the higher order image states grow in while dosing a monolayer. These observations confirm that Xe grows in patches and that the image electrons residing on these patches sample the local workfunction and layer potential. After three layers, the Xe coverage is no longer uniform and peaks corresponding to more than one coverage are visible in a given spectrum as shown in Figure 3.3b. At this coverage the $n = 2$ state is at the onset of becoming a quantum well state of the Xe layer. Its energy change, therefore, is most sensitive to further layer growth and provides an accurate characterization of the coverage.

Layers of n-heptane is grown in a similar fashion as Xe on Ag(111), except the temperatures at which n-heptane layers form is higher. Liquid n-heptane was degassed by three cycles of freeze-pump-thaw before introducing n-heptane vapor into the UHV chamber[98]. For n-heptane on Ag(111), a monolayer will stick at 180 K. By lowering the temperature to 140 K, a bilayer of n-heptane begins to stick to the surface. To grow a

trilayer of n-heptane, temperatures below 135 K must be maintained. After growing layers of n-heptane onto the Ag(111) surface, the sample is cooled to a lower temperature to maintain the integrity of the interface. The lowest attainable sample temperature is 120 K when cooled with a liquid nitrogen cryostat. LEED studies have confirmed that n-alkanes grow ordered layers on Ag(111) with the carbon-carbon bonds parallel to the surface[99]

3.3 LEED/Auger Spectrometer

The order and cleanliness and sample orientation of the Ag(111) surface were determined by LEED/Auger. It should be noted that the broadness of the image state peaks is a much better indication of the surface order. The physisorption nature of n-heptane and Xe on Ag(111) renders the use of LEED/Auger in characterizing their structure and growth difficult. Sharp transient LEED patterns, however, often confirm the well-ordered growth of these materials and other physisorbed materials. The OMICRON LEED/Auger spectrometer consists of the SPECTALEED electron optics, NGLEED S:LEED/Auger controller, and the PC PEN LEED which includes the DAT 100 data acquisition software and LIAC control software. The 4-grid SPECTALEED optics is rear viewed which gives high visibility of the LEED pattern. The NGLEED control unit supplies the optics with the filament heating current and voltages for the lens apertures of the electron gun, the grids, and the LEED screen. In LEED, only the SPECTALEED optics and the NGLEED controller are used. The electron gun unit consists of a heated thoriated tungsten filament in a Wehnelt cylinder followed by an electrostatic lens made up of four apertures. The electron energy is determined by the potential difference between the cathode and apertures 1 and 3 inside the electron gun. The Wehnelt cylinder itself is set to a negative bias with respect to the cathode to collimate the electron beam. The optics consists of a fluorescent screen with four grids. The first grid, last grid, and the sample are all grounded. The fluorescent screen has a positive bias of a few kV to accelerate the electrons. The advantage of a 4-grid setup is the ability to reduced inelastically scattered electrons by applying a small negative bias to

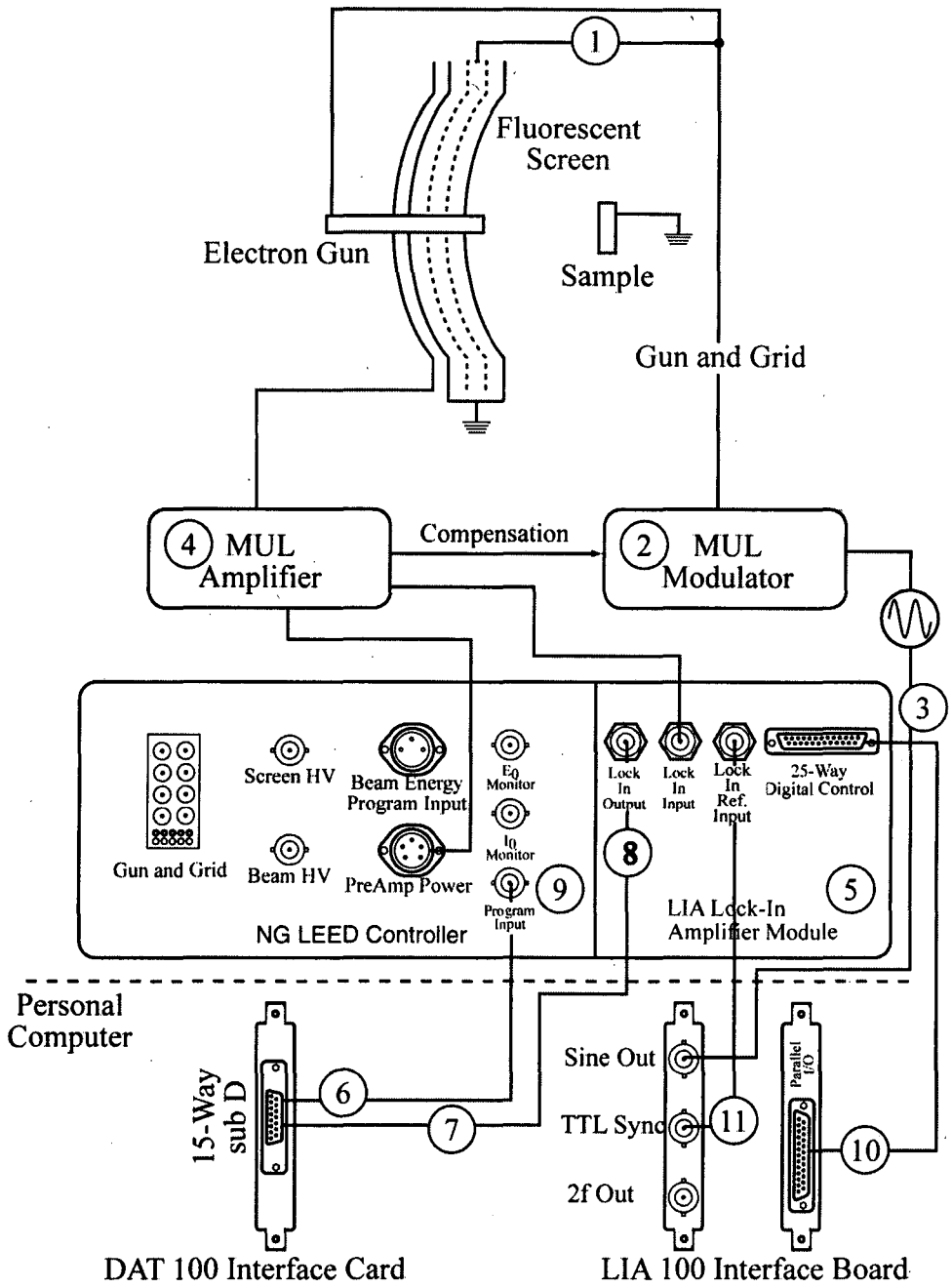

Figure 3.4. Auger electron spectroscopy set-up

the middle grid. Inelastically scattered electrons result in a relatively homogeneous background illumination. A schematic of the LEED optics is shown in Figure 3.4.

The LEED procedures are documented in the laboratory notebook. The high-voltage screen is connected to the NGLEED controller during LEED operation. The I_{fil} current should be increased to a reading of 1.5 Amps in about one minute. In order to check the emission current(I_E), which should be in the range of 0.1 to 0.3 mA, the Wehnelt must be turned off. Once I_E is in the correct range, the Wehnelt can be set to –9.3V to collimate the electrons. The lens apertures should be set when the beam energy is at 1000 eV. The screen voltage is set to 2, which corresponds to 2 kV. LEED spots are observable at about 45 eV in electron kinetic energy for Ag(111). The suppresser can be set if the screen background is too bright as a result of inelastically scattered electrons.

Two additional components for Auger spectroscopy are incorporated into the NGLEED controller. They are the LIA Lock-In Amplifier and the matching unit for LEED(MUL). The MUL consists of a preamplifier and a voltage modulator. An oscillating voltage is added to the retarding voltage during data acquisition. Retarding voltage is delivered via grids 2 and 3. A schematic diagram of the retarding field Auger spectrometer is shown in Figure 3.4. The MUL modulator controls the power to the electron gun and the retarding voltage(1) as shown in Figure 3.4. The MUL modulator(2) via the Gun and Grid of the NGLEED controller drives the retarding voltage while incorporating a sine function from the LIA 100 interface board(3). The screen becomes an electron collector in the Auger mode and the signal is preamplified by the MUL amplifier(4). The signal finally becomes amplified by the LIA lock-in(5). The DAT 100 program controls the Auger measurements by driving the ramp generator through the retarding control voltage(6-9) and collecting the analogue data from the amplifier(7-8). Inside the personal computer, the DAT 100 interface board requires a single 8-bit ISA compatible expansion slot. The LIA 100 interface board occupies two full slots, one for the digital interface for the lock-in amplifier(10) and one for the sine wave and TTL reference output(11) for the lock-in amplifier. Both the DAT 100 software and LIA 100

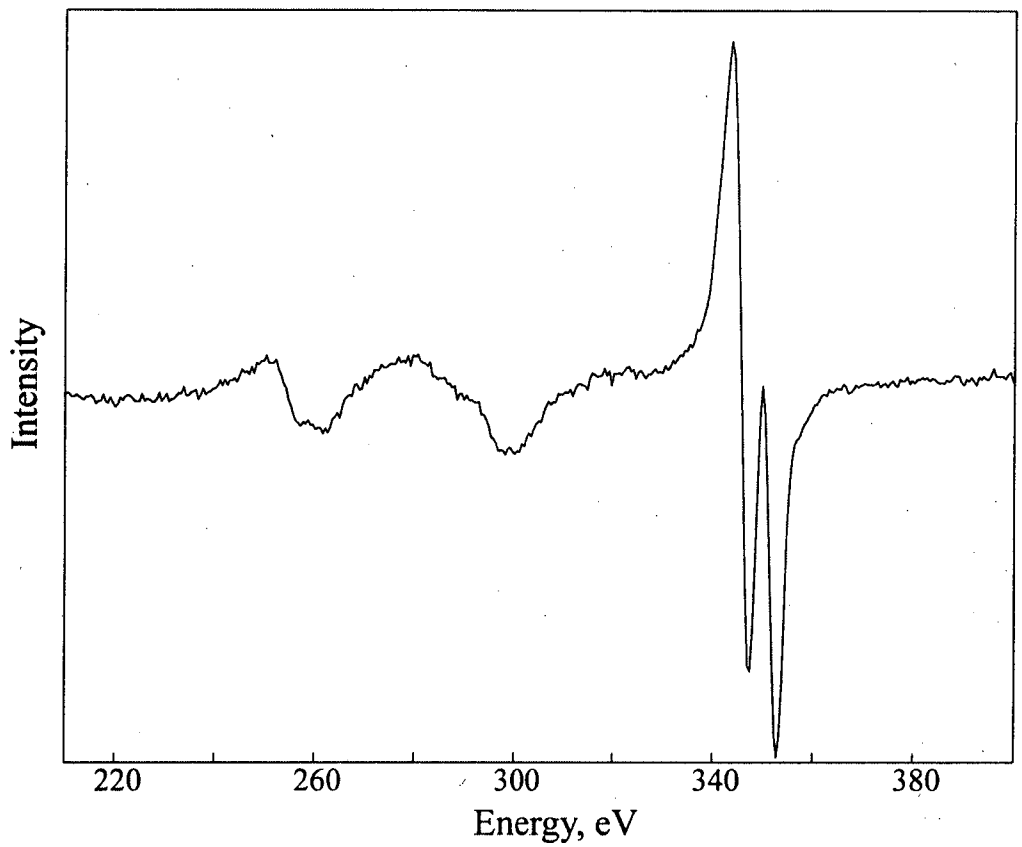

Figure 3.5. Auger electron spectrum of a clean surface Ag(111) with the settings described in the text.

software are installed under Windows 95. All settings relevant for Auger electron spectroscopy are controlled by the LIA 100 software through the parallel I/O PC LIAC board connected by cable 10. These settings are stored in a file called defaults.txt under the AES directory in our laboratory computer*. An Auger spectrum of our Ag(111) sample acquired using these parameters is shown in Figure 3.5.

3.4 Turbomolecular Pump System

The upgraded turbo pump system is essential in maintaining a clean ultrahigh vacuum chamber, though the ultimate pressure of 1×10^{-10} Torr is obtained by using an ion-pump. It is important to utilize the turbo pump when flowing sample into the chamber during dosing and for pumping out noble gases such as Ar during Ar-ion sputtering. The theory of operation of the turbo pump is discussed in detail in the Edwards EXT Turbomolecular Pumps Instruction Manual. Only the interlock system that was implemented in our laboratory will be discussed in this section. Figure 3.6 is a schematic diagram of the Turbomolecular pump setup and electrical connections of the interlock system. The EXT250 turbo pump has a pumping speed of about 200 L/s for N_2 gas and an ultimate pressure of $< 5\times10^{-10}$ torr when using a conflat inlet flange. The nominal rotational speed is 60,000 rpm with a starting time of about 100 seconds. In an event of a power failure, the vacuum chamber is protected from contaminants by the

---

* The current content of defaults.txt are the following:
BaseAddress=0x308
LockinPhase=15
LockinTimeConstant=10 ms
LockinSensitivity=10 mV
LockinDynamics= Low Drift
OscillatorAmplitue=5.0 Vpp
LockinFilter=12 dB/Octave
OscillatorFrequency=4.7 kHz LEED
LockinInput=Voltage

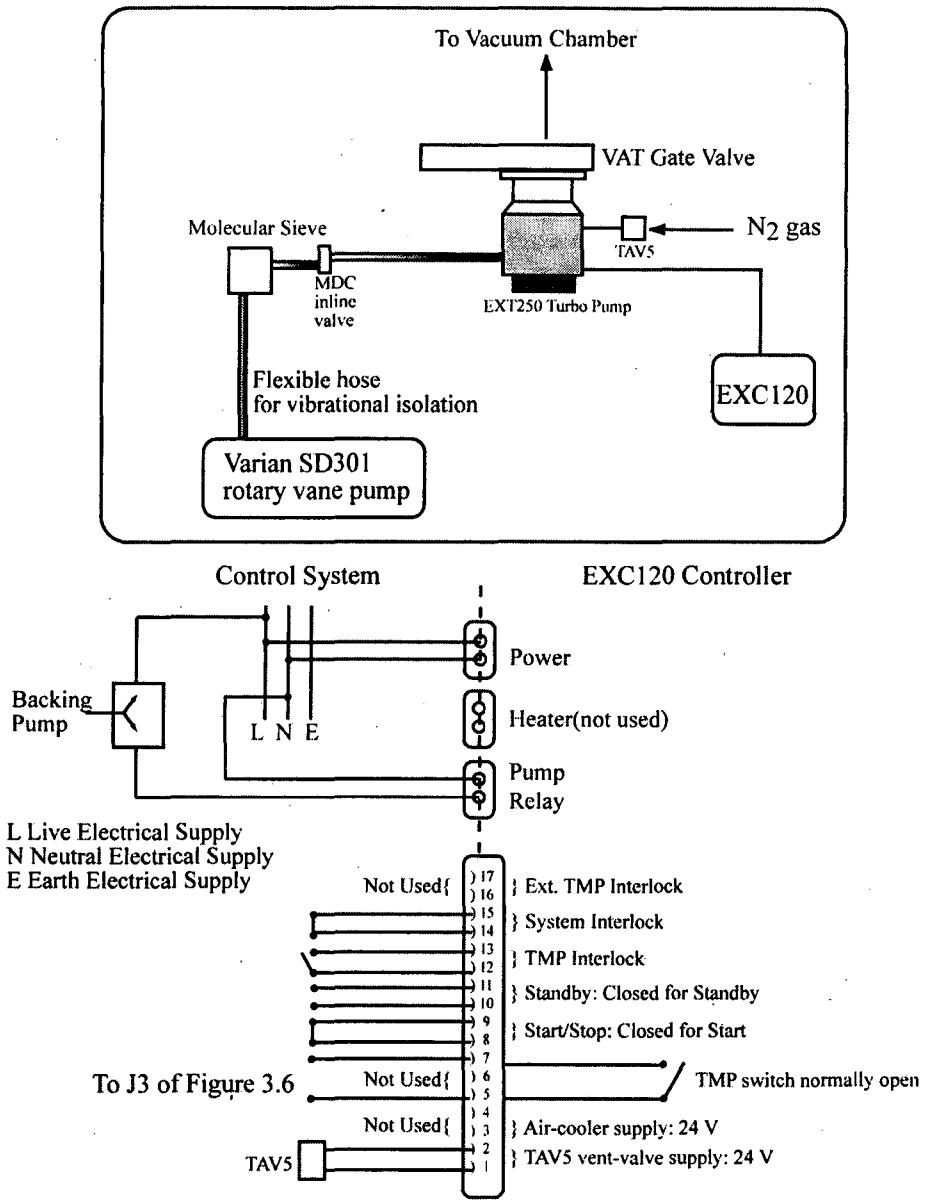

Figure 3.6. Turbo Pump setup and EXC120 controller electrical connections.

VAT pneumatic gate valve and the MDC pneumatic in-line valve. Power to the SD301 Varian backing pump is also cutoff. The EXC120 turbo pump controller is used to implement these safety features.

The SD301 Varian backing pump is not intended for the use of pumping corrosive gases. It is advisable to purge the pump through the gas ballast for such applications. It should be noted that purging would increase the ultimate pumped pressure. During compression, the pressure may increase to above the maximum vapor pressure causing condensation. Purging also reduces condensation in the backing pump. In the application where a gas mixture containing more than 21% O_2 is pumped, it is advisable not to use mineral-origin pump oil to avoid the possibility of self-ignition. Oxygen can also oxidize the mineral oil, which will quickly destroy its lubricating properties. In case of 21% or higher oxygen level, perfluorinated synthetic oil should be used to prevent these problems. One may even purge the pump through the gas ballast with nitrogen when pumping out a large amount of O_2 gas.

The TAV5 solenoid valve is set to vent the turbo pump with nitrogen gas when the rotational speed of the EXT pump has fallen below 50% of the full rotational speed. This will prevent any back streaming of hydrocarbons from the backing pump into the vacuum chamber. The TAV5 valve is closed during operation by maintaining power to the solenoid valve. During power failure, the TAV5 power is still maintained by the secondary regenerative supply that uses the DC motor of the EXT pump as a generator. The speed of the pump is indicated on the EXC120 controller by 4 LED lights where each represents a 25% range of the full speed. When the first LED is lit, the speed of the pump is in the range of 0 to 25% of the full speed. After start-up, it is possible to check whether full speed is reached by witnessing the lighting of the fourth LED and the Bake-out light by selecting Heater-On. The Heater-On feature cannot be enabled until the pump is at full speed. When a heater band is connected, the turbo pump can be baked out at temperatures above 70° C. It is important to make sure that the inlet flange does not exceed 100° C. Four hours is usually sufficient to bake out the pump itself.

The bottom of Figure 3.6 depicts the electrical connections of the EXC120 controller. The legends define some of the electrical connections. The heater band is currently not in use. The EXC120 logic interface has 17 pins. Pin 1 and 2 are the

electrical supply for the 24V TAV5 vent valve. Pin 3 and 4 are the electrical supply for the air-cooler, which is not used since the pump is currently cooled by water. Pins 5, 6, and 7 make up the TMP status output signal. Linking pin 8 and 9 together defeats the Start/Stop interlock. In order to allow the backing pump to turn on when Start is selected, the SYS interlock must be defeated by linking pin 14 and 15 together. Pin 16 and 17 give the analogue signal output of the pump speed. The pump relay controls the roughing pump and closes when the Start on the EXC120 controller is selected even if the TMP interlock(pin 12 and 13) is not closed. During initial rough pumping of the vacuum chamber after bringing the chamber to atmospheric pressure, the TMP interlock connection should be opened to allow the backing pump to pump the chamber below 500 mtorr before allowing the turbo pump to start. The turbo pump will start upon closing the TMP interlock connection. Pin 5 and 7 are connected to the solenoid valve switchbox, which closes both the inline valve and the gate valve during power failure. For the sake of completeness, the solenoid valve electrical connections are shown in Figure 3.7. The EXC120 controller TMP output switch(Pin 5 and 7) has a low current and voltage rating of 1A and 25VDC, respectively. The controller relay is electrically isolated from the electrical supply to both the inline and the gate valve by using an external relay as shown in Figure 3.7. The relay between pin 5 and 7 is normally open. Normally open is defined as the switch being open when there is no electrical supply. When the pump reaches 100% of the full speed, pin 5 and 7 become continuous and are used to control the electrical supply to both the VAT gate valve and the MDC inline valve.

Figure 3.7 depicts four switches that are used to control the MDC inline and the VAT gate valve. Switches S2 and S3, which are normally open, are necessary when switching between Open and Protect since S1 and S4 will go through the Shut position. The external relay has a rating of 5 A 10 VDC. It is currently powered by a 12V AC adapter. When there is no electrical power going into J2, the solenoid valve in the VAT Gate Valve will allow high-pressure N_2 gas to pneumatically close and protect the chamber. Loss of power at J1 will release high-pressure gas in the MDC inline valve which shuts and protects the turbo pump from hydrocarbon contamination from the backing pump. The higher pressure N_2 is set at about 90 psi in order to have enough

pressure to control the valves. Pressure below 70 psi will inadvertently cause the MDC inline valve to close, which ultimately causes damage to the turbo pump.

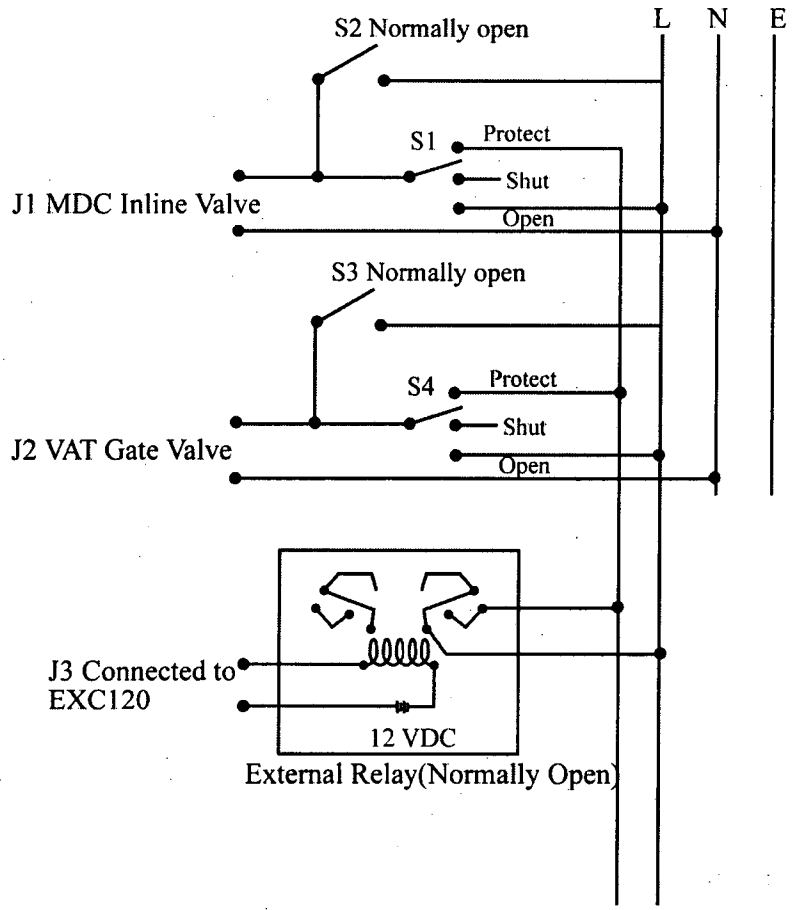

Figure 3.7. Switch box to Turbo-Pump interlock system. J1 and J2 are connected to the Inline Valve and Gate Valve, respectively. J3 is connected to Pins 5 and 7 as shown in Figure 3.6.

Chapter 4

Electron Dynamics at the Clean Ag(111) Surface

Before discussing the population dynamics of image electrons at dielectric/metal interfaces, an investigation of the clean surface dynamics is in order. Although the relaxation dynamics of charge carriers in metals can be deduced through the analysis of linewidths measured by photoemission, this method only gives an upper limit for the relaxation of the electron and hole[41,100,101]. Both surface contamination and disorder contribute to inhomogeneous spectral broadening, a broadening with a Gaussian functional form, which complicates the extraction of the relaxation dynamics of the surface electrons via linewidth analysis. Our time-of-flight electron energy detector also poses a limitation to the lifetime determination of image electrons, even for image electrons in states that are degenerate with the conduction band and should exhibit considerably shorter lifetimes. The instrument function of our time-of-flight detector has a Gaussian width of 20 meV. The time-energy uncertainty relation, $\Gamma \cdot \tau = 660$ meV·fs, gives us an estimate of the upper limit of the lifetime of about 30 fs that can be accurately determined through linewidth analysis. Lifetimes longer than 30 fs may be washed out by the detector instrument function itself, regardless of surface contamination and disorder. If the width of the instrument function is comparable to the intrinsic linewidth, the lifetime may still be determined by fitting the photoemission result with a convolution of the instrument function and a Lorentzian function whose width is determined by the lifetime of the state.

Time resolved TPPE is a more versatile technique in the study of surface electron dynamics. The lifetime of image state electrons that are discussed in this chapter can be as long as a few hundred femtoseconds for the higher order image states. The population dynamics of image electrons up to $n = 5$ at the Ag(111) surface have been experimentally

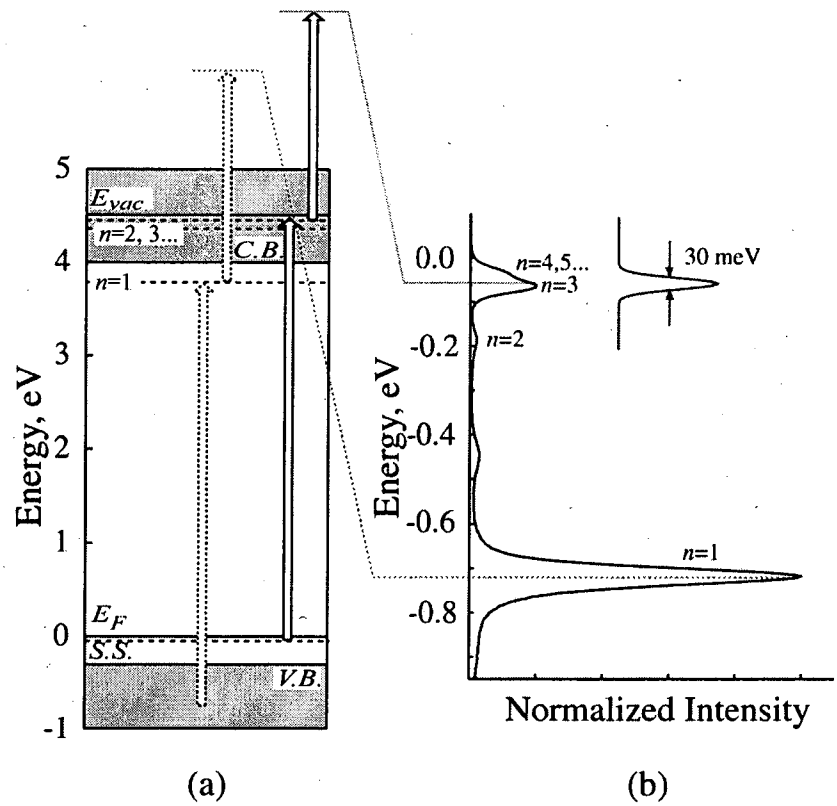

Figure 4.1. Projected band structure of Ag(111) at the Brillouin zone center with the excitation scheme of two photon photoemission. (a) Dashed lines represent surface states and solid lines represent bulk states. The excitation of $n = 1$ is off resonance with the occupied surface state(*S.S.*) (b) Static two photon photoemission spectrum taken at 540 nm probe and 270 nm pump. The higher intensity of $n = 3$ as compared to $n = 2$ is a result of resonant excitation from *S.S.*

determined by femtosecond TPPE in combination with the coherent excitation of a superposition of states. The degeneracy of the $n \geq 2$ image states with the conduction band results in an efficient decay channel for electrons residing in these higher image potential states, since these image states can strongly hybridize with the conduction bands having the same energy and parallel momentum. The lifetimes of these surface resonances are shown to follow a classical oscillation attempt rate where the lifetimes of the states scale as n^3 and correspond to the duration of a few round trips for a particle moving in a $\frac{1}{r}$ potential. Despite the strong interaction of the surface states with the bulk electronic states, the image electrons in the higher image potential states spend most of their time out in the vacuum which is manifested by their relatively long lifetimes.

4.1 Clean Surface Image State Lifetimes

The femtosecond pulses, which were generated by an optical parametric amplifier pumped by an 800 nm Ti:sapphire regenerative amplifier exhibit sufficiently broad bandwidth of 30 meV to excite a coherent superposition of several high quantum number image states($n \geq 4$) as shown in Figure 4.1. The spectrum shown in Figure 4.1b was taken with 4.60 eV pump and 2.30 eV probe pulse. With the pump photon energy at 4.60 eV, the higher image states($n \geq 4$) are resonantly excited from the occupied surface state. The higher intensity of these image states as compared to $n = 2$ is also witnessed. The instrument function for 4.60 eV pump/2.30 eV probe pulses cannot be determined from the surface state dynamics trace since excitation from this state is resonant with the higher image states. Instead, the instrument function can be determined by summing over several bins in the background of the static spectra at each time delay. At 4.60 eV pump and 2.30 eV probe, the instrument function was determined to be 170 fs. Since the $n = 1$ state can be populated with lower photon energies, the lifetime of $n = 1$ was determine using 4.14 eV pump and 2.07 eV probe with an instrument function of 115 fs.

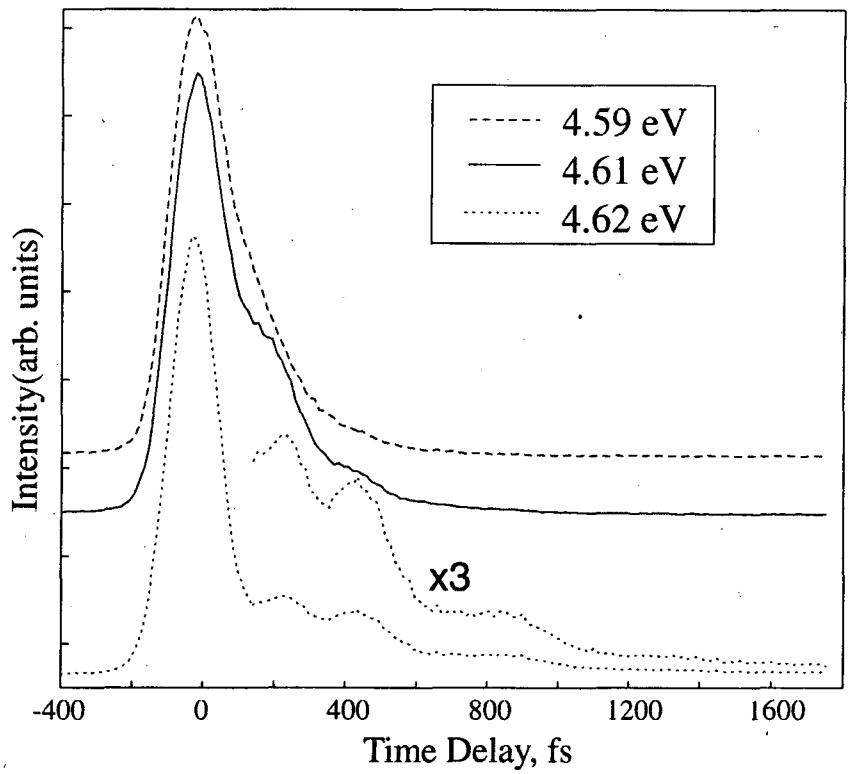

Figure 4.2. The dynamics traces for $n \geq 4$ states at varying pump photon energies. As the photon energy increases from 4.59 eV(dashed line) to 4.61 eV(solid line), the frequency component corresponding to the energy difference between $n = 4$ and $n = 5$ becomes prominent in the dynamics trace. At higher photon energy of 4.62 eV(dotted line), the frequency component corresponding to the energy difference between $n = 5$ and $n = 6$ becomes slightly noticeable as shown by the small increase in signal at around 850 fs.

Quantum number n	E_b (eV)	Lifetime (fs)	CTP (Å)	T_{cl} (fs)	Round Trips
1	0.77	36±8	4.68	1.8	20
2	0.22	26±8	17.14	12.6	2
3	0.10	60±5	38.11	38.1	1.4
4	-	177±7	67.77	67.8	1.8
5	-	290±50	105.89	105.9	1.5

Table 4.1: Lifetimes, binding energies, and classical turning point(CTP), Classical Oscillation Period, Round Trips.

The dynamics traces of the $n \geq 4$ states are shown in Figure 4.2 with the corresponding pump photon energies. As the pump photon energy increases from 4.59 eV to 4.61 eV, the frequency component which corresponds to the energy difference between $n = 4$ and $n = 5$ becomes prominent in the dynamic traces. The period of this frequency component is about 243±10 fs. At a slightly higher photon energy of 4.62 eV, the frequency component corresponding to the energy difference between $n = 5$ and $n = 6$ results in an oscillation period in the dynamics trace of about 470±30 fs. The oscillation periods were deduced using single value decomposition[102]. Coherent oscillation between $n = 3$ and $n = 4$ was not observed. The dynamics traces were taken at the resonant excitation peak maximum around $n = 4$ in Figure 4.1b. The binding energies for $n = 1$ to $n = 3$ were determined directly from the TPPE static spectrum and are exhibited in Table 4.1. The quantum beat only gives us the energy difference between the higher order image states and does not give a direct measure of the binding energy.

The lifetimes of the image states were determined by fitting a convolution of a Gaussian instrument function with an exponential function[103,104]. The dynamics traces up to $n = 4$ are shown in Figure 4.3a. In order to obtain a good fit to the dynamics traces, the exponential function must posses both a rise time and a decay time. The image state is assumed to be populated at a rate of $k_1 = \tau_1^{-1}$ and decay at a rate of $k_2 = \tau_2^{-1}$. The rate equation has the functional form of

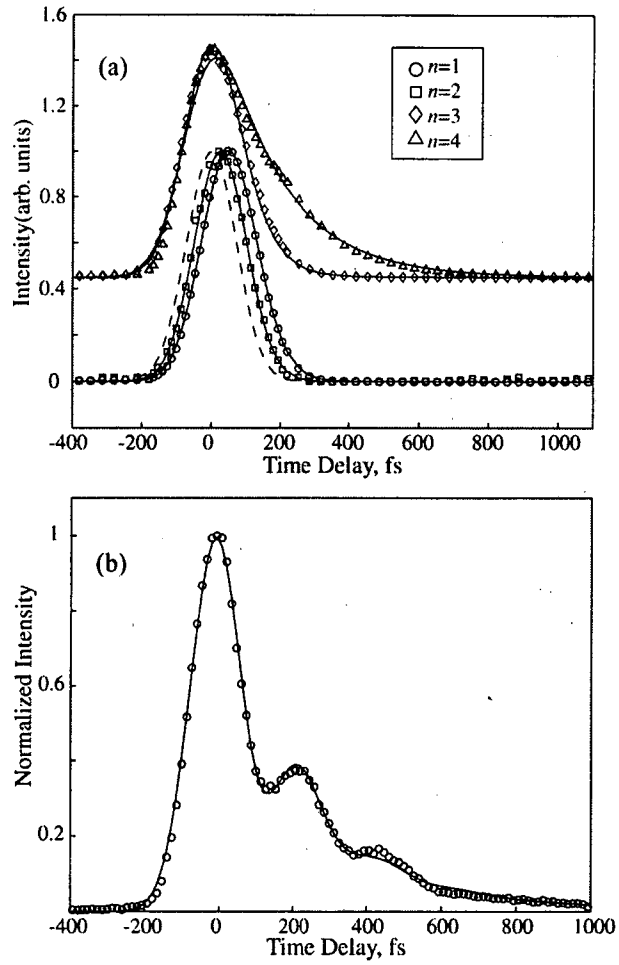

Figure 4.3. The dynamics traces for $n = 1$ to $n = 5$. The solid lines in (a) are fits obtained by convolving a single exponential function with a Gaussian instrument function for $n = 1$ to $n = 4$. The $n = 1$ requires an exponential rise of about 30 fs. The solid line (b) is a fit obtained by convolving Equation 4.2 with a Gaussian instrument function while holding the $n = 4$ lifetime constant in order to obtain the lifetime of $n = 5$ and a pure dephasing time.

$$n(\tau_1,\tau_2,t) \propto \frac{k_1}{k_2-k_1}\left[\exp(-k_1(t-t_0))-\exp(-k_2(t-t_0))\right], \qquad (4.1)$$

where t_0 is the time delay at which the UV and the visible pulses are directly overlapped. The lifetimes for $n=1$ and $n=2$ were measured to be 36±8 and 26±8 fs, respectively. These lifetimes are slightly longer than the lifetimes measured at room temperature by Schoenlein *et al.* The lifetimes for $n=3$ to $n=5$ were determined to be 60±5, 177±7, and 290±50 fs, respectively. In order to accurately determine the lifetime of $n=4$, a pump pulse energy of about 4.59 eV was used to minimize population of $n=5$. Since $n=3$ and $n=4$ are extremely close in energy, their dynamics traces were extracted by fitting the peaks to a double Voight function in the energy spectrum at each time delay. Despite careful fitting and selection of the pump photon energy, there is still contribution to the $n=4$ lifetime from $n=5$ as shown by a slight oscillation at around 200 fs in the $n=4$ dynamics trace.

To minimize the number of parameters, the $n=5$ lifetime was determined by holding the $n=4$ lifetime constant while fitting the dynamics trace shown in Figure 4.3b with a functional form that comprises three exponential decay functions of which one has a cosine oscillation component. Explicitly, the fit to Figure 4.3b is a convolution of a Gaussian instrument function with a function that has the following form:

$$n(t) = A_1 \exp\left(-\frac{t}{\mathrm{T}_{14}}\right) + A_2 \exp\left(-\frac{t}{\mathrm{T}_{15}}\right) + A_3 \exp\left(-\frac{t}{\mathrm{T}_2}\right)\cos(\omega t+\delta), \quad (4.2)$$

where A_1, A_2, and A_3 are the amplitudes, T_{14} is the $n=4$ lifetime, T_{15} is the $n=5$ lifetime, ω is set to $\frac{2\pi}{243}\,\mathrm{fs}^{-1}$ as determined from single value decomposition, δ is an arbitrary phase shift, and $\mathrm{T}_2 = \frac{1}{2\mathrm{T}_{14}} + \frac{1}{2\mathrm{T}_{15}} + \frac{1}{\mathrm{T}^*}$ with T^* representing a relative pure dephasing time between the two states. The pure dephasing time is determined to be about 400 fs. The lifetime of $n=4$ was set to the experimentally determined value of 177 fs. All the lifetime measurements are recorded in Table 4.1.

Höfer and coworkers have recently shown that the pure dephasing time in the loss of coherence in quantum beats has a direct correlation to the surface order[42]. The

lifetimes of the image states describe the population decay by inelastic scattering events. The pure dephasing time is attributed to quasi-elastic scattering processes which do not change the population of the image state but rather destroy the coherence between the superposition of states. Höfer and coworkers studied the change in the dephasing time between $n = 3$ and $n = 4$ as a function of CO exposure on Cu(100). The dephasing time was determine to be 280, 60, 40 fs for a clean Cu(100), 0.04 ML of CO on Cu(100), and 0.08 ML of CO on Cu(100), respectively. The change in the dephasing time was attributed to the scattering of the image-state electron by the reciprocal lattice vectors of the CO overlayer.

4.2 Classical Oscillation Period

The lifetime of an image electron is primarily determined by the coupling of the electronic state with the bulk states. This coupling can be approximated by the overlap of the image state wavefunction with the substrate. For image electronic states that reside in the bulk band gap, such as the image states on the (100) surface of noble metals, the electron penetration can be calculated using the two band NFE model which results in an evanescent wavefunction in the metal substrate. Image states that are close to the band edges or degenerate with the bulk continuum will have significant electron penetration into the bulk which renders faster electron decay[74,105]. At the (111) surface of noble metals, the image states are either close to or degenerate with the conduction band. The degeneracy of the higher image states with the conduction band precludes the use of the two-band NFE model in calculating the wavefunction overlap with the metal substrate. The imaginary part of the wavevector in the metal is zero within this formalism which results in a wavefunction that extends indefinitely into the bulk. Without imposing an artificial cut-off on the wavefunction in the substrate for image states that are degenerate with the conduction band, the normalized wavefunction would result in an overlap of $P \approx 1$. This model would predict a progressively shorter lifetime for the higher image states since the decay rate would be proportional only to the energy of the state as discussed in Section 2.2.

In an attempt to model the clean surface image state lifetimes, a classical model which treats the image state electron as a particle oscillating between the surface and the

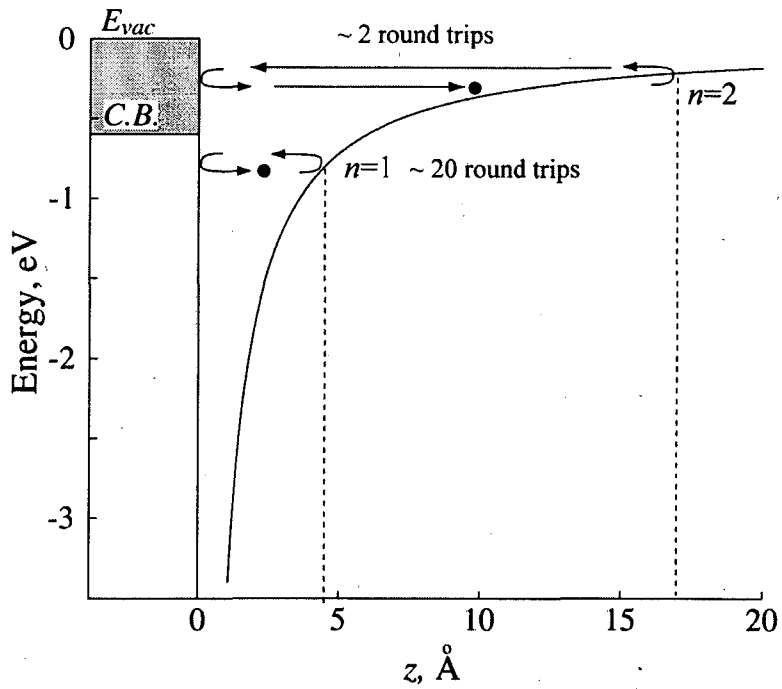

Figure 4.4. The above schematic diagram shows the classical oscillations of image state electrons between the surface and the Coulomb potential. According to the model, the $n = 1$ electron oscillates about 20 times while the $n = 2,3,...$ image electrons decay into the metal after 2 round trips. The dotted lines in the figure depict the classical turning points of the electrons.

Coulomb potential clearly illustrates the image state lifetimes as shown in Figure 4.4. The classical period of motion has been utilized by Cole to model the lifetime of image electrons residing on the dielectric-metal interface[106]. The classical oscillation period represents an "attempt rate". As illustrated in Figure 4.4, at every instance where the electron oscillates back toward the metal surface, the image electron has a finite probability of decaying back into the metal. The classical oscillation period is given by an integral over the classically allowed range:

$$T_{cl} = 2\int_0^{z_m}\left(\frac{m}{2[E-V(z)]}\right)^{1/2} dz, \tag{4.3}$$

where the classically allowed range is between the surface of the metal at $z = 0$ and at $z = z_m$, the classical turning point at the Coulomb potential. The variable m is taken as the free electron mass. The factor of two in Equation 4.3 is necessary since each oscillation requires the electron to travel twice the distance between the classically allowed regions. Since it is difficult to determine the form of the potential $V(z)$, especially close to the surface of the metal, the integral cannot be solved without making further assumptions. Cole has determined the limits of the classical oscillation period by using two functions, namely, $V_u(z)$ and $V_l(z)$ which are the upper (u) and the lower (l) bounds for $V(z)$ and permits the integration of T_{cl} [106]. The two functions are defined as follows:

$$V_l(z) \equiv -\frac{e^2}{4z}, \tag{4.4}$$

$$\begin{aligned} V_u(z) &\equiv V(z_m) - V'(z_m)(z_m - z) \\ &= E - V'(z_m)(z_m - z) \end{aligned} \tag{4.5}$$

where the prime denotes differentiation. The upper and lower bounds of the classical oscillation period are then given by the following equations:

$$T_{cl}^u = \left(\frac{2mz_m}{V'(z_m)}\right)^{1/2} \tag{4.6}$$

$$T_{cl}^l = \left[\frac{me^4}{32|E|^3}\right]^{1/2}\left[\left(u+u^2\right)^{1/2} - \ln\left(\left(1+u\right)^{1/2} + u^{1/2}\right)\right], \tag{4.7}$$

where $u = 4|E|z_m/e^2$.

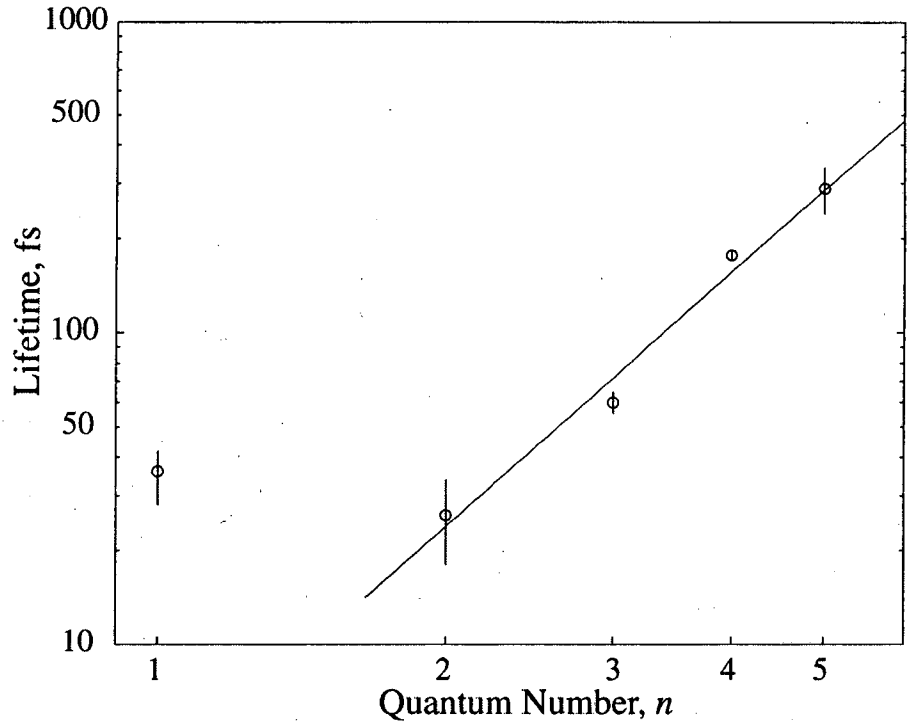

Figure 4.5. The logarithms of the lifetimes of the image states are plotted versus n. The error bars that correspond to each data point indicate the 95% confidence limits. The line is the best fit through the $n = 2$ to $n = 5$ data points with a quantum number dependence of $(n + a)^{2.7}$.

Equations 4.6 and 4.7 illustrate the essential physics that determines the image state lifetimes. According to Equation 4.6, the classical oscillation period is governed by the differential of the potential with respect to the distance evaluated at the classical turning point of the image electron. The differentiation of the potential simply gives the restoring force for the electron, where the force becomes weaker for electrons residing in the higher order image states as illustrated by a smaller slope in the Coulomb potential at the classical turning point for the $n = 2$ electron in Figure 4.4. The progressively weaker restoring force results in a longer lifetime for the higher order image electrons. Equation 4.7 illustrates the lifetime dependence of an image electron as a function of its quantum number. The lower limit of the classical oscillation period is inversely proportional to $|E|^{3/2}$. With the eigenvalues of the image states determined by Equation 2.17, the classical oscillation period or the lifetime of the image state should scale as $(n+a)^3$.

In Figure 4.5, the line represents the best fit through the $n = 2$ to $n = 5$ lifetimes with a quantum number dependence of $(n+a)^{2.7\pm0.4}$, where $a = 0.05$. The intercept of the fit at $n = 1$(not shown in the figure) would predict a $n = 1$ lifetime of about 3.7 fs if $n = 1$ were degenerate with the conduction band. It has been shown for $n = 1$ at the Cu(111) surface that increasing the sample temperature will decrease the band gap, resulting in a higher faster decay of the electronic state[105]. The lifetime of the $n = 1$ image state on Ag(111) deviates more significantly from the power dependence than for Ag(100) since it is the only state in the image state progression that resides in the band gap. The measured lifetimes for $n = 2$ to $n = 5$ give a relative measure of the surface reflectivity for electrons in states that are degenerate with the bulk continuum. The reflectivity of electrons at surfaces is inversely proportional to the density of states of the bulk material at the energy of the electrons[107]. It is useful to compare the experimentally determined lifetimes with the classical oscillation period. According to Equation 4.6 and 4.7, the most important parameters that determine the classical period of motion are the energy of the electron and its classical turning point. The classical turning points as determined by the binding energy of the image states are shown in Table 4.1. The binding energies of $n = 4$ and $n = 5$ were assumed to follow the hydrogenic model with the quantum defect parameter equal to 0.05. Comparison between T_{cl}^{u} and T_{cl}^{l}

reveals that the upper limit of the classical oscillation period is about a factor of 4 larger. For convenience of discussion, the lifetime determined by the classical oscillation period is taken as T_{cl}^{u}, which is shown in the second to last column in Table 4.1. The number of round trips is equal to the measured lifetime divided by the oscillation period. The $n=2$ to $n=5$ image states decay after about 2 round trips in the image potential according to this classical model. Within this model, the number of round trips for the $n=1$ state is calculated to be 20, which is an order of magnitude larger than for $n=2$ to $n=5$ and is attributed to the increase in surface reflectivity when the energy of the state lies within the band gap.

Höfer *et al.* have measured the higher order image state lifetimes for the Cu(100) surface where all the image states reside in the band gap. The image state lifetimes for $n=2$ to $n=6$ and $n=2$ to $n=3$ on the Cu(100) and the Ag(100) surfaces, respectively, where shown to scale with the $(n+a)^3$ power law since all the states at these surfaces reside in the band gap. Although the $n=1$ also reside in the band gap at these surfaces, measured $n=1$ lifetime of 55±5 fs for Ag(100) and 40±6 for Cu(100) by Shumay *et al.* deviate by almost a factor of two from the $(n+a)^3$ power dependence as compared to the higher order image state lifetimes[108]. This result may be attributed to a significantly different surface potential experienced by $n=1$ due to its larger binding energy difference of about 0.5 eV and the proximity of its wavefunction to the surface as compared to the rest of the image state progression. The lifetime of the image state should be highly sensitive to the shape of the image state wavefunction which is governed by the surface potential. Theoretical calculations of the $n=1$ lifetime of 26.5 fs for Ag(100) and 30 fs for Cu(100) by Chulkov *et al.* also confirm this discrepancy in the $n=1$ lifetime. Their calculation uses a realistic model potential and evaluates the lifetimes from the self-energy of the excited quasi-particle within the *GW* approximation[109]. A more detailed analysis of the potential close to the surface and other possible contributions to the damping rate of the $n=1$ state will be required in order to resolve these issues.

Despite the increasing sophistication of theoretical studies of image state dynamics, the effect of the degeneracy with the substrate band structure on image state

dynamics remains undetermined [109,110]. Fundamental aspects of surface mediated chemical processes, photodesorption, and vibrational relaxation are involved with the transfer of electrons between the surface and the adsorbed molecules[111-113]. The relaxation of an electron from an excited state at the surface depends highly on the energy of the state with respect to the substrate bands. On metal surfaces, resonant charge transfer(RCT) is the most probable transfer mechanism when the electronic state is degenerate with the bulk continuum. The abrupt change in the surface potential at the surface, however, may result in a finite surface reflectivity which hinders RCT. The significant role of the substrate band structure and surface reflectivity on charge transfer between an ion and a noble metal surface has recently been demonstrated by H^- and F^- ion-surface collision experiments[112,113].

In this section we have shown that the degeneracy of the higher image states with the conduction band results in an efficient decay channel for the electrons where the lifetime results from the oscillation period in the image potential. Even though the higher image states can strongly hybridize with the conduction band states, the electrons in these states spend most of their time out in the vacuum. The number of round trips for these electrons is about 2 according to the classical oscillation model. In contrast, the $n = 1$ image electron oscillates around 20 times, an order of magnitude higher, before decaying back into the metal substrate.

4.3 Image State Electron Wavepacket

The coherent excitation of a superposition of several quantum states results in an interference between the states and the creation of electron wave packets [37]. As mentioned earlier, coherent photoelectron spectroscopy offers additional information regarding the phase relaxation of the image state wavefunctions. This phenomenon was first observed by Höfer *et al.* for the higher order image states on Cu(100) and sheds light on the dynamical evolution of the excited electrons in space and time[37,42]. The oscillations of the electron dynamics as shown in Figure 4.2, mainly reflect the beating

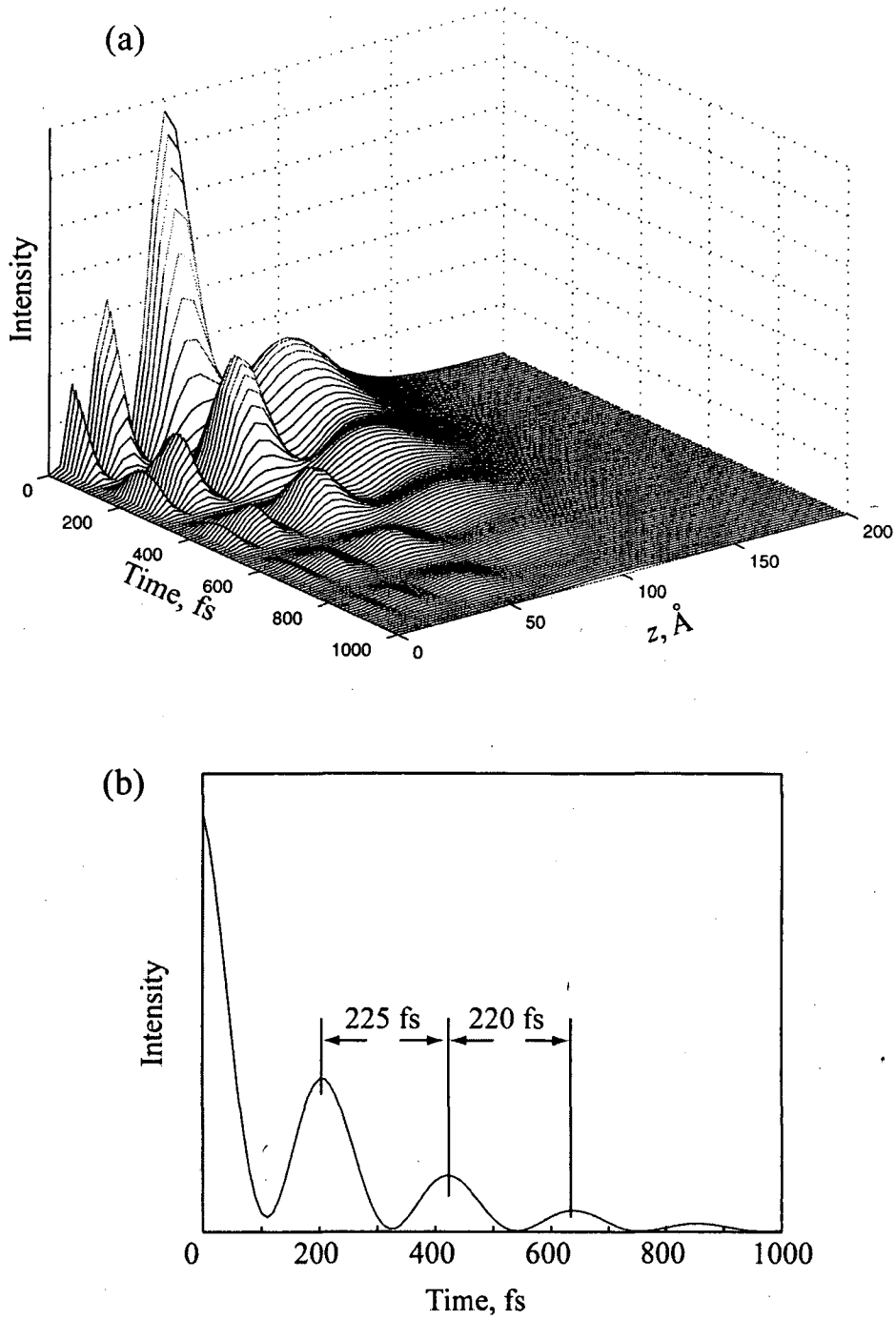

Figure 4.6. (a) Electron wave packet resulting from the interference between $n = 4$ and $n = 5$. The wave packet can travel as far as a 100 Å away from the surface. (b) The profile of the wave packet as a function of time determined by summing the intensity between the range of $z = 0$ and $z = 10$ Å.

between $n = 4$ and $n = 5$. In such a simple case, the wave function of the electron wave packet is represented by the following expression:

$$\Psi_n(t) = a_4(t)|4\rangle \exp(-i\omega_4 t) + a_5(t)|5\rangle \exp(-i\omega_5 t), \tag{4.8}$$

where $a_4(t)$ and $a_5(t)$ are exponentially decaying coefficients, $\omega_4 = \frac{E_4}{\hbar}$, and $\omega_5 = \frac{E_5}{\hbar}$. The square modulus of the above expression results in the following expression for the TPPE intensity when there is no loss of coherence:

$$I(t) = a_4^2 + a_5^2 + 2a_4 a_5 \cos(\omega_{4,5} t)\langle 4|5\rangle, \tag{4.9}$$

where $\omega_{4,5} = \frac{(E_5 - E_4)}{\hbar}$. Equation 4.9 has the same functional form as Equation 4.2, except in Equation 4.2, an arbitrary phase shift and a pure dephasing time has been incorporated into the last term. The general form of the wave packet in space representation is, therefore, given by the following expression after Höfer *et al.*[37]:

$$\Psi_{WP}(z,t) = \sum_n a_n z R_n^{l=0}(z/4) \exp(-i\omega_n t). \tag{4.10}$$

To get a qualitative understanding of the origin of the quantum beat observed in the time resolved TPPE experimental results an electron wave packet has been modeled using Equation 4.10 with the assumption that only $n = 4$ and $n = 5$ are coherently excited with no loss of coherence. The result of the calculation is depicted in Figure 4.6a, where the electron wave packet can travel as far as a 100 Å for the superposition of $n = 4$ and $n = 5$. The profile of the wave packet as a function of time is shown in Figure 4.6b by summing the intensity in Figure 4.6a between the range of $z = 0$ and $z = 10$ Å. The period of the oscillation as shown in the figure is about 220 fs, which compares extremely well with the experimentally determined value of 240±10 fs. The population decay times of the image states were included in the calculation and are set to the experimentally determined values as discussed Section 4.2. The interpretation of the photoemission intensity for the quantum beat of the image states has been discussed by Höfer *et al.* and can be explained by the following description[37]. After the coherent excitation of a superposition of image states, the wave packet evolves in time and oscillates between the substrate and the Coulomb potential. When the electron wave packet is far away from the surface, the electron is nearly free and cannot conserve

energy and momentum upon absorbing a photon. The substrate is able to provide the necessary momentum for the electron to absorb a photon only when the electron wave packet is close to the surface. This is analogous to the Rydberg wave packets of atomic physics[114].

4.4 Optical Bloch Equation

Coherence between the excitation and photoemission electric field and the optically induced electron-hole polarization need to be considered when modeling surface state and hot electron lifetimes that are <100 fs[41]. Coherent effects, within the context of our study, refer to the shorter excitation pulse as compared to the phase memory of the excited electrons. In the limit where the lifetime of the state is significantly longer than the excitation pulse width, the coherence effects will be washed out and become insignificant in the determination of the lifetime of the state of interest. When this is true, rate equations may be used to model the electron dynamics. The rate equations that were used above to describe the TPPE kinetics data may be inadequate in describing the $n=1$ and $n=2$ dynamics due to their short lifetimes. The time shift observed in the image state dynamics as shown in Figure 3.2b may be caused by coherence effects. Other features such as quantum beats due to interference between two or more states, the surface state dynamics, and the narrowing of the spectral linewidth at longer time delays can be properly described by using the Optical Bloch Equations[115-117]. The optical Bloch equations are similar to equations derived by Bloch to describe the motion of a spin in an oscillatory magnetic field[118]. The equations of motion of the density matrix in a three state model for a pump-probe process are given by

$$\frac{\partial \rho_{00}}{\partial t} = -\frac{i\mu_a E_a(t)}{\hbar}(\tilde{\rho}_{01} - \tilde{\rho}_{10}), \tag{4.11}$$

$$\frac{\partial \rho_{11}}{\partial t} = +\frac{i\mu_a E_a(t)}{\hbar}(\tilde{\rho}_{01} - \tilde{\rho}_{10}) - \frac{i\mu_b E_b(t-t_p)}{\hbar}(\tilde{\rho}_{12} - \tilde{\rho}_{21}) - \Gamma_1 \rho_{11}, \tag{4.12}$$

$$\frac{\partial \rho_{22}}{\partial t} = -\frac{i\mu_b E_b(t-t_p)}{\hbar}(\tilde{\rho}_{12} - \tilde{\rho}_{21}), \tag{4.13}$$

$$\frac{\partial \tilde{\rho}_{01}}{\partial t} = +\frac{i\mu_a E_a(t)}{2\hbar}(\rho_{11} - \rho_{00}) - \frac{i\mu_b E_b(t-t_p)}{2\hbar}\tilde{\rho}_{02} - \Gamma_{01}\tilde{\rho}_{01}, \tag{4.14}$$

$$\frac{\partial \tilde{\rho}_{12}}{\partial t} = +\frac{i\mu_b E_b(t-t_p)}{2\hbar}(\rho_{22} - \rho_{11}) + \frac{i\mu_a E_a(t)}{2\hbar}\tilde{\rho}_{02} + -\Gamma_{12}\tilde{\rho}_{12}, \tag{4.15}$$

$$\frac{\partial \tilde{\rho}_{02}}{\partial t} = +\frac{i\mu_a E_a(t)}{2\hbar}\tilde{\rho}_{12} - \frac{i\mu_b E_b(t-t_p)}{2\hbar}\tilde{\rho}_{01} - \Gamma_{02}\tilde{\rho}_{02}, \tag{4.16}$$

where t_p is the time delay between the pump and the probe pulse and ρ_{mm}'s are the diagonal elements with linewidths of $\Gamma_m = 1/T_m$, which is related to the population decay rate. The index $m = 0$, $m = 1$, and $m = 2$ denote the initial occupied bulk state, the image state, and the final free electron state. The off-diagonal terms, $\rho_{mm'}$, have a linewidth of $\Gamma_{mm'} = \Gamma_m^* + \Gamma_{m'}^* + \frac{\Gamma_m}{2}$, where $\Gamma_m^* = 1/T_m^*$ is the pure dephasing time of the state $|m\rangle$. The lifetime of the final state, a free electron state, is assumed to be infinite and results in $\Gamma_2 \to 0$. The radiation field is introduced in Equations 4.11 through 4.16 by $E_a(t)$ and $E_b(t)$ which are the square root of the intensity and represent the pump and probe pulses, respectively. The radiation field profiles are assumed to have a Gaussian functional form. Finally, the μ_a and μ_b are the transition dipole moments and are assumed to be small for our low laser flux.

Using interferometric TPPE, Petek and coworkers have shown that the dephasing time of the initial state increases near the Fermi level[41]. At about 0.2 to 1.2 eV below the Fermi level, the dephasing time of the initial state is about 5 fs for Cu(111) and increases to about 10 fs near the Fermi level. No measurements, however, were done on the Ag crystal. In an attempt to understand the importance of coherence effects on our lower image state electron dynamics, Equations 4.11 through 4.16 were solved with the following parameters. The dephasing time of the initial state is assumed to be 5 fs since the 4.14 eV pump photon used in the study of the $n = 1$ dynamics will populate the state

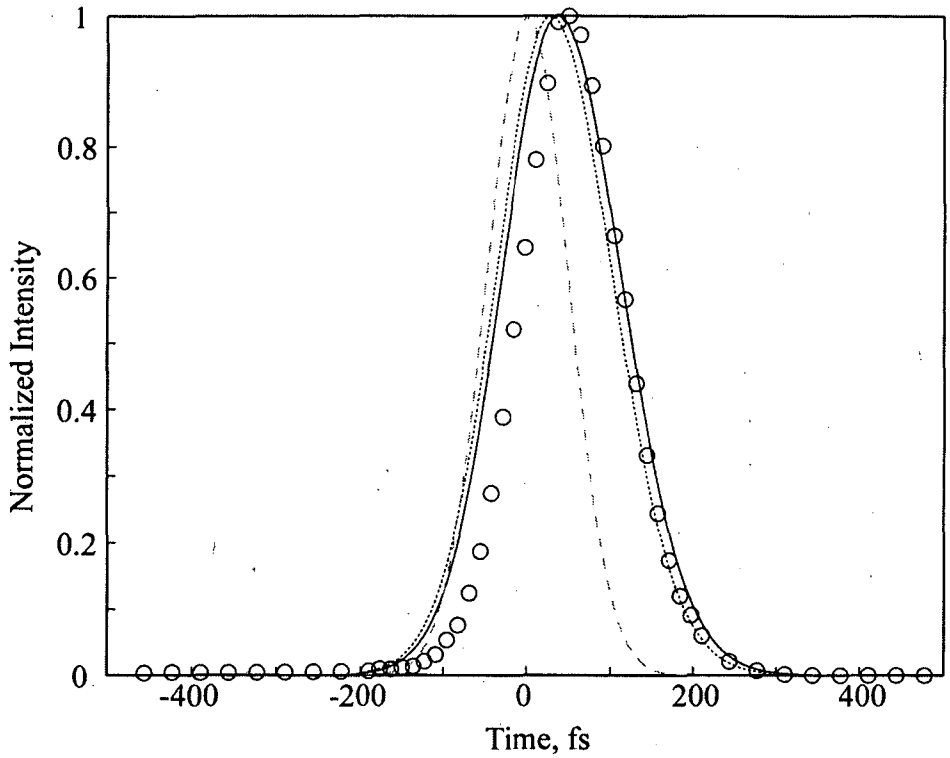

Figure 4.7. Solution of the three-level optical Bloch equation for ρ_{22} as a function of time delay(Solid line) assuming no detuning. The circles are the experimental data point of $n = 1$. The dashed line is the Gaussian instrument function. The solid line represents the best fit through the data points with the lifetime of the image state determined to be 25 fs and a pure dephasing time of 350 fs. The dotted line is also a solution of the three-level optical Bloch equation for ρ_{22} as a function of time delay with a lifetime of the image state equal to 25 fs and a pure dephasing time of 30 fs.

from initial states about 0.34 eV below the Fermi level. It should be noted that the calculated dynamics is not sensitive to the dephasing time of the initial state. The initial state lifetime and final state lifetime and the dephasing time of the final state are assumed to be infinite. The parameters that require further analysis are the pure dephasing time of the intermediate state and its lifetime. The pure dephasing time of the intermediate state should be considerably long. As shown by Petek and Ogawa, even the occupied surface state has a dephasing time of about 20 fs. The wavefunctions of image states extend further into the vacuum, which results in a weaker coupling of the states with the metal substrate, and therefore a longer dephasing time of the states as compared to the occupied surface state.

The calculated ρ_{22} as a function of time delay(t_p) between the pump and the probe pulse can be fitted to the experimental results as shown in Figure 4.7. The lifetime and dephasing time of the intermediate state as determined by the best fit through the experimental data points are 25 fs and 350 fs, respectively. This result entails that the linewidth should be at least 15 meV. The fit of the $n = 1$ linewidth to a convolution of a Lorentzian and a Gaussian results in a Lorentzian width of about 40 meV. This is deduced by assuming that the Gaussian width of the time-of-flight electron energy detector is 20 meV. The linewidth measurement results in a reasonable total dephasing time of the intermediate state of about 16 fs. For comparison, the optical Bloch equation was also solved with the dephasing time of the intermediate state equal to 30 fs. It is clear from the figure that the rise is faster when the dephasing time is short. In the limit where the field envelope is slowly varying with respect to the total dephasing time of the intermediate state, the optical Bloch equations reduce to the standard rate equation. It is clear from Figure 4.7 that the solution to the optical Bloch equations does not fit well through the data points. Even with a longer pure dephasing time of the intermediate state, this formalism cannot account for the rise time of the $n = 1$ dynamics. In Equations 4.11 through 4.16, the rate of change of each matrix element is proportional to the dipole moment multiplied by the electron field intensity. For a small field strength as satisfied by the low fluence of our laser pulses, this factor has little effect on the calculated dynamics. The condition as mentioned by Wolf and co-workers must be

$\int_{-\infty}^{\infty}(\mu E(t)/\hbar)dt << \pi$ [117]. It is confirmed in our laboratory that by varying the laser intensity with a filter does not affect the dynamics of the states.

In determining the best fit through the kinetics traces assuming a simple rate equation model, a rise time of 30 fs and 0 fs were required for $n=1$ and $n=2$, respectively. According to the optical Bloch formalism, the pure dephasing time of the $n=2$ state must be shorter than the $n=1$ state. This rapid dephasing of $n=2$ may be the result of its degeneracy with the conduction band. Since $n=2$ and $n=1$ have very similar lifetimes, their coupling with the metal substrate should not differ by as much as an order of magnitude. A better explanation of the lack of rise time for $n=2$ requires the understanding of parallel momentum relaxation of the image state electrons. The description of possible contributions to the rise time in image state dynamics are as follows. Upon excitation of the image state band as shown in Figure 2.2, electrons with different parallel momentum can decay into states that are near the surface Brillouin zone center where the states have parallel momentum close to zero. As will be discussed in Chapter 6, the penetration of the wavefunction into the substrate causes rapid parallel momentum relaxation, which is the case for $n=2$ and results in a faster rise time. Another important aspect to consider is the extent of the excitation of the image state band. Per pump photon energy, less states of higher parallel momentum of the $n=2$ band is excited as compared to $n=1$. Further experimental investigation of the rise time as a function of the pump photon energy will shed light on these issues. The Ag(111) band structure, however, is inadequate for this study since the band gap extends below the Fermi level and complications arise from the presence of the occupied surface state. The Ag(100) band structure does not have an occupied surface state and has states extending above the Fermi level. The more simplistic Ag(100) band structure will give a better control of the population of the image state bands as a function of pump photon energy. These experiments are currently underway in our laboratory.

Chapter 5

Interband Electron Dynamics at Dielectric-Metal Interfaces

The energies and relaxation dynamics of image electrons at a dielectric/metal interface reflect the nature of the electronic interaction with both the substrate and the adsorbed layer. In section 2.1, it was mentioned that the expectation value of the image state wavefunction is given by $\langle z \rangle = 6a_0 n^2$ in the hydrogenic approximation for a perfect conductor. For the $n = 1$ state, the expectation value is about 3 Å away from the surface. Because of the proximity of the image state wavefunction to the surface, the adsorption of materials onto the surface will drastically alter the binding energy, lifetime, and relaxation dynamics of an image electron. Thus, image electrons are very sensitive probes to the changes of the interfacial band structure as materials are grown in a layer-by-layer fashion. The interband relaxation dynamics of image electrons can be model through the use of a dielectric continuum model, which approximates the interfacial potential using bulk parameters even for a few layers of noble gas or n-alkane on a metal substrate[106]. The readers are reminded that the image state electron wavefunction is in fact bulk like in the direction parallel to the interface.

Two different dielectric materials have been introduced onto a Ag(111) surface. Specifically they are Xe and n-heptane, which have been studied extensively in our laboratory. These materials are inert and will physisorb onto the Ag(111) substrate. Thus, the band structure of the substrate and adsorbates are only weakly perturbed. Bulk Xe has a positive electron affinity as measured by Schwentner, Himpsel, Saile, Skibowski, Steinmann, and Koch to be 0.5 eV[119]. Comparison to other n-alkanes gives us an approximate electron affinity for bulk n-heptane of –0.2 eV. The positive

electron affinity of bulk Xe allows higher quantum image states to move into the Xe layer to form quantum well states. The decay of the delocalized $n = 1$ and $n = 2$ states at the Xe/Ag(111) interface shows a strong angular dependence or parallel momentum dependence. These results can be explained by a parameterization method in which the overlap of the wavefunction in different parts of the potential is utilized to model the two-dimensional scattering rate of image electrons at the Xe/Ag(111) interface. At the n-heptane/Ag(111) interface, delocalized electrons self-trapping into a small polaron state has been observed. The energy of the localized state with respect to the bottom of the image state band is constant as a function of layer thickness, which demonstrates that the image electrons mainly interact with the dielectric material at the adsorbate/vacuum interface. This is a valid assumption since the probability density of the image state wavefunction is concentrated at the n-heptane/vacuum interface owing to the negative electron affinity of the alkane layer. Results of electron dynamics in the degrees of freedom parallel to the dielectric/metal interface are discussed in Chapter 6. This chapter deals with the interband relaxation of image electrons at both the Xe/Ag(111) and n-heptane/Ag(111) interfaces, where interband relaxation refers to the transition of an image electron to the metal substrate bands.

5.1 Dielectric Continuum Approximation

The physisorption characteristics of both Xe and n-heptane on the Ag(111) surface validate the use of the two-band NFE approximation to model the band structure of Ag. Outside the metal, the simple Coulomb potential of an excess electron at a metal surface is altered significantly by the adsorption of materials that change the dielectric susceptibility of the interface. Cole was the first to model the potential near the surface of metals in the presence of adsorbed dielectric materials, such as He, Ne, and H_2 films, by using the dielectric continuum approximation[106,121]. The dielectric continuum approximation treats the overlayer as a dielectric continuum in which the electronic structures of the individual atoms or molecules are ignored. The potential felt by an electron depends on the location of the electron, namely inside or outside the dielectric

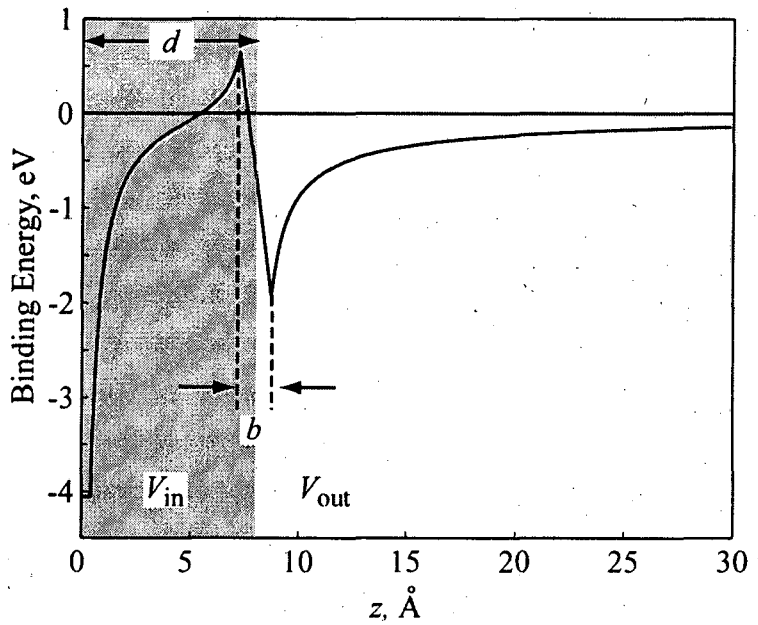

Figure 5.1. Dielectric continuum model for two layers of n-heptane is shown. The thickness of the layer is denoted by d. The potential inside and outside the layer are denoted by V_{in} and V_{out}. Close to the layer boundary at the vacuum-layer interface, a singularity in the potential curve is avoided by using an artificial parameter b and interpolating the potential curve between $d - b/2$ and $d + b/2$. The parameter b is considered an adjustable parameter in determining the binding energy of the image states and is usually on the order of 1 Å.

overlayer near the overlayer/vacuum interface(Figure 5.1). Upon adsorption of a dielectric material on a metal surface, the potential felt by an electron located near the dielectric/vacuum interface can be represent by the following expression:

$$V_{out}(z,d) = \frac{-\beta e^2}{4(z-d)} + \frac{(1-\beta^2)e^2}{4\beta}\sum_{n=1}^{\infty}\frac{(-\beta)^n}{z-d-nd}, \qquad d+b/2<z, \quad (5.1)$$

where z is the distance from the metal, d is the layer thickness, b is an artificial cutoff to avoid a singularity at the dielectric/vacuum interface, ε is the dielectric constant of the adsorbed material, and $\beta = \frac{(\varepsilon-1)}{(\varepsilon+1)}$. The overlayer thickness, d, is equal to the interplanar distance of the bulk material times the number of layers adsorbed. In the limit of an infinite overlayer thickness, an electron in the vacuum outside the layer will only polarize the dielectric material, which gives rise to a Coulomb potential equal to the first term of Equation 5.1. Reducing the number of layers introduces additional terms that result from the proximity and interaction of the electron with the metal. The additional terms are represented as an infinite series in Equation 5.1. The potential inside the overlayer as given by Professor J.D. Jackson[122] is represented by the following equation:

$$\begin{aligned} V_{in}(z) &= -\frac{e^2}{4\varepsilon z} + \frac{e^2(\varepsilon-1)}{4\varepsilon(\varepsilon+1)(d-z)} - \frac{e^2(\varepsilon-1)(d+2z)}{4\varepsilon(\varepsilon+1)d(d+z)} + \delta V_i(z) + V_0 \\ \delta V_i(z) &= -\frac{e^2 z^2}{2\varepsilon d^3}\sum_{n=2}^{\infty}\frac{(-1)^n}{n(n^2-z^2/d^2)}\left(\frac{\varepsilon-1}{\varepsilon+1}\right)^n \end{aligned} \qquad ,0<z<d-b/2, (5.2)$$

where the additive constant V_0 is the electron affinity of the adsorbed layer. The first term in Equation 5.2 represents the potential of an electron that results from its image charge in the metal substrate that is screened by the presence of the dielectric material. The potential for two layers of n-heptane is shown in Figure 5.1. The parameters used to calculate this potential are $\varepsilon = 2.0$, $V_0 = 0.2$ eV, and d = 8Å that were determined from bulk n-octane values[120]. In Figure 5.1, artificial cut-offs are imposed on the potential to avoid singularities at both the metal-dielectric junction and at the dielectric-vacuum junction. At the dielectric-vacuum interface, singularities in the potential curve are avoided by setting an artificial parameter b. The potential curve is approximated by

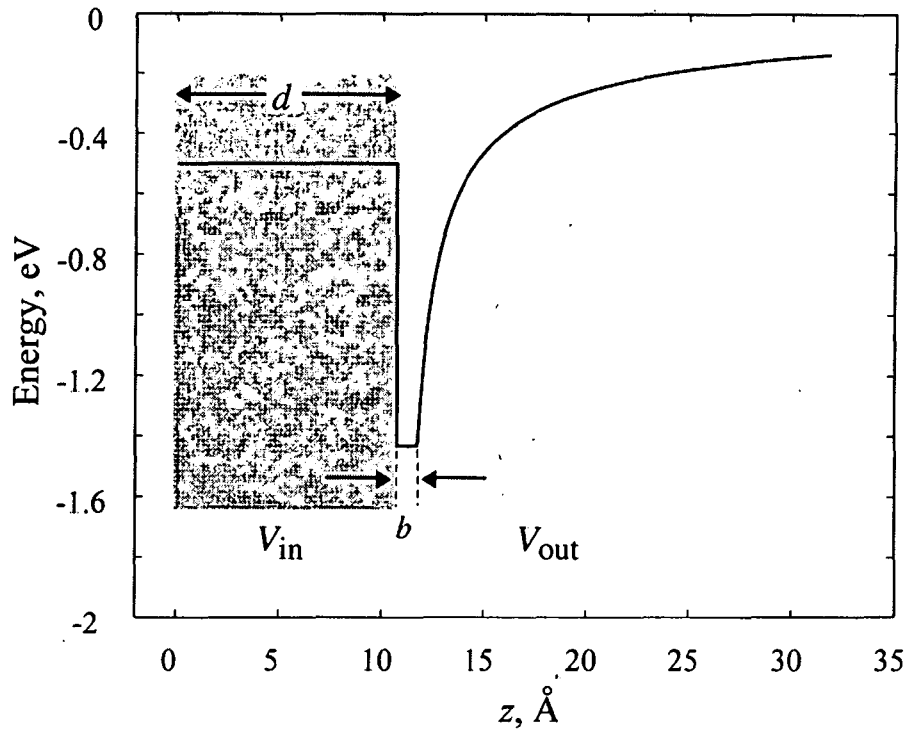

Figure 5.2. A flat potential representation for three layers of Xe is shown. The thickness of the layer is denoted by d. V_{in} and V_{out} denote the potential inside and outside the layer. An artificial parameter b is introduced to avoid a singularity close to the overlayer/vacuum interface.

interpolation between $d-b/2$ and $d+b/2$ as shown in the Figure 5.1. It should be noted that $z = 0$ Å always represents the surface of the metal substrate.

The form of the potential experienced by an electron inside the overlayer depends on the energy of the image electron with respect to the electron affinity level of the overlayer. A flat potential representation of the Xe overlayer potential is more effective in reproducing the binding energy for the higher order image states. For $n \geq 2$, the energies of these states are above the Xe conduction band and a flat potential of

$$V_{in}(z) = V_{CB,Xe}, \qquad 0 < z < d \qquad (5.3)$$

is used, where $V_{CB,Xe}$ is the conduction band minimum of bulk Xe. The attractive electron affinity or conduction band minimum of $V_{CB,Xe}$ = -0.50 eV of Xe allows the higher order image electrons to reside in the Xe overlayer. The conduction band minimum, in this case, is referenced to the vacuum level which is set to 0 eV. The potential experienced by the higher order image electrons is shown in Figure 5.2 for three layers of Xe. The interplanar distance of 3.577 Å is taken from x-ray diffraction data for Xe adsorbed on Ag(111)[13]. The lifetime of the $n = 1$ state as a function of layer thickness is overestimated when using the flat potential. Experimentally determined lifetimes of $n = 1$ for up to six layers of Xe approach an asymptotic value of about 800 fs[33]. Since the energy of $n = 1$ is below the Xe conduction band minimum, the $n = 1$ will see a square potential barrier which results in an exponential increase in its lifetime as a function of layer thickness.

5.2 Interband Electron Dynamics at the n-heptane/Ag(111) Interface

Increasing the layer coverage of n-heptane on Ag(111) results in a monotonic decrease in the binding energy of the image electrons. Upon growing a layer of n-heptane onto the Ag(111) surface, the workfunction decreases from 4.56 eV to about 4.06eV. It should be noted that the binding energy of image states are pinned to the vacuum level. The energy of image states, therefore, become closer to the middle of the

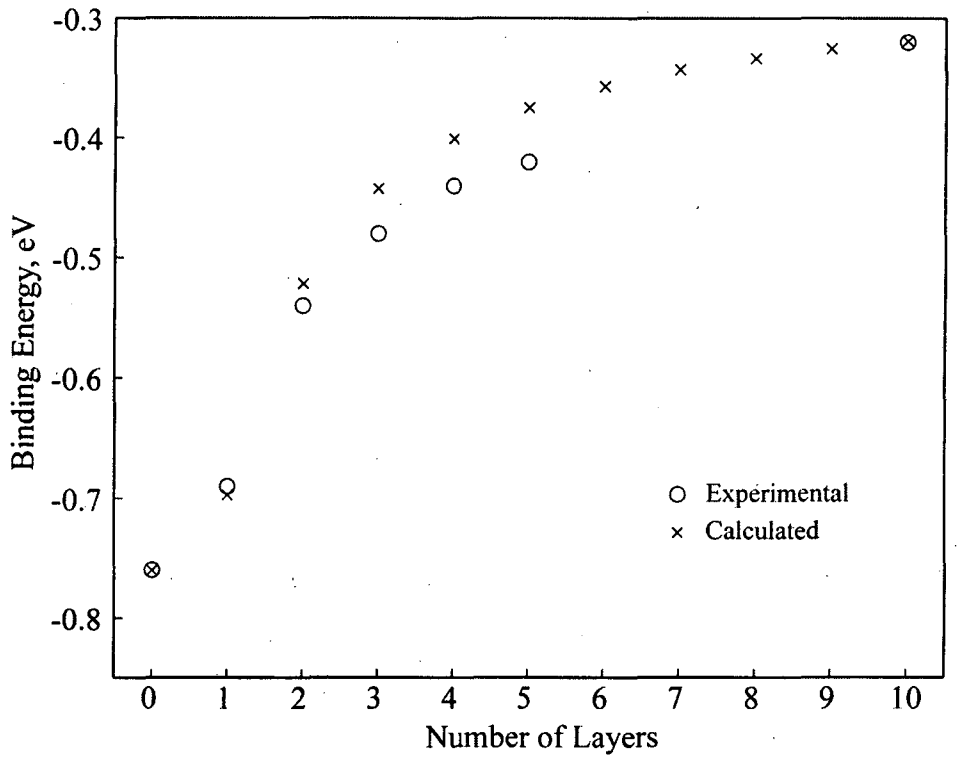

Figure 5.3. Experimentally determined binding energy(o) of $n = 1$ for up to ten layers of n-heptane on Ag(111). The calculated values(×) are determined using the dielectric continuum model as described in the text.

band gap after the workfunction decrease. This also contributes to the decrease in the wavefunction overlap of the image state with the metal substrate as already discussed in Section 2.2. The binding energy of $n = 1$ for up to ten layers of n-heptane is shown in Figure 5.3. The calculated binding energy as a function of layer thickness was determined using the dielectric continuum model with the potential calculated from Equations 5.1 and 5.2. As the layer thickness increases, the interaction of the electron with the metal is reduced and the energy of the image electron approaches an asymptotic value. As shown in Figure 5.3 the change in the binding energy of the electron becomes less dramatic after 3 layers of n-heptane. A more dramatic effect of the n-heptane overlayer is demonstrated by the increase in the lifetime of the image electrons. Since the $n = 1$ state has the lowest energy and is closest to the surface as compared to the higher order image states, the $n = 1$ electron is a more sensitive probe of the changes in the potential caused by the n-heptane overlayer. Its sensitivity to the interfacial potential is manifested both in its binding energy and lifetime as a function of layer thickness. The $n = 1$ has an approximately exponential increase in its lifetime as a function of layer thickness. The experimentally determined lifetimes are 32, 155, 1580, and 17 600 fs for a bare Ag(111) surface, monolayer, bilayer, and trilayer of n-heptane on Ag(111), respectively. As discussed in Section 2.2, the lifetime of the image state electron is inversely proportional to the image electron probability density inside the metal substrate. For the simple case of a square potential barrier, an incident wave function towards the barrier will result in a tunneling probability that is proportional to $e^{-2|\kappa|d}$, where κ is the imaginary part of the wave vector inside the barrier and d is the barrier thickness. The approximate exponential increase in the lifetime as a function of layer thickness reflects the exponential decay of the tunneling probability as a function of the barrier width.

The interfacial potential of n-heptane layer on Ag(111) can be approximated through the use of Equation 5.1 and 5.2. The calculated $n = 1$ image state wavefunctions for one and three layers of n-heptane on Ag(111) are shown Figure 5.4. The slope and value of Equation 2.15 are propagated numerically using a fourth and fifth-order Runge-Kutta integrator with adaptive step sizes through the overlayer potential and out into the vacuum. The trial solutions are evaluated for a range of energies to find solutions for which the wavefunction vanishes at about 120 Å outside the layer. The wavefunctions of

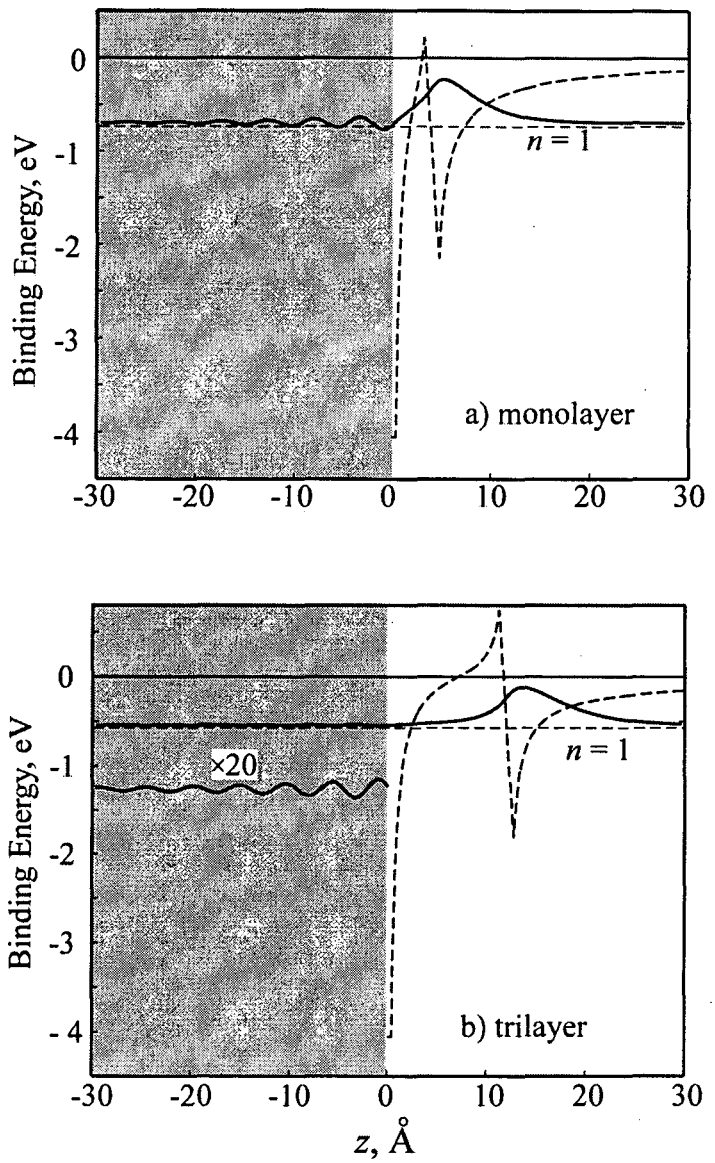

Figure 5.4. Calculated $n = 1$ wavefunction as a function of layer thickness for one and three layers of n-heptane on Ag(111). The evanescent wave in the metal is multiplied by a factor of twenty for the trilayer to demonstrate the dramatic decrease in the wavefunction penetration as the thickness increases.

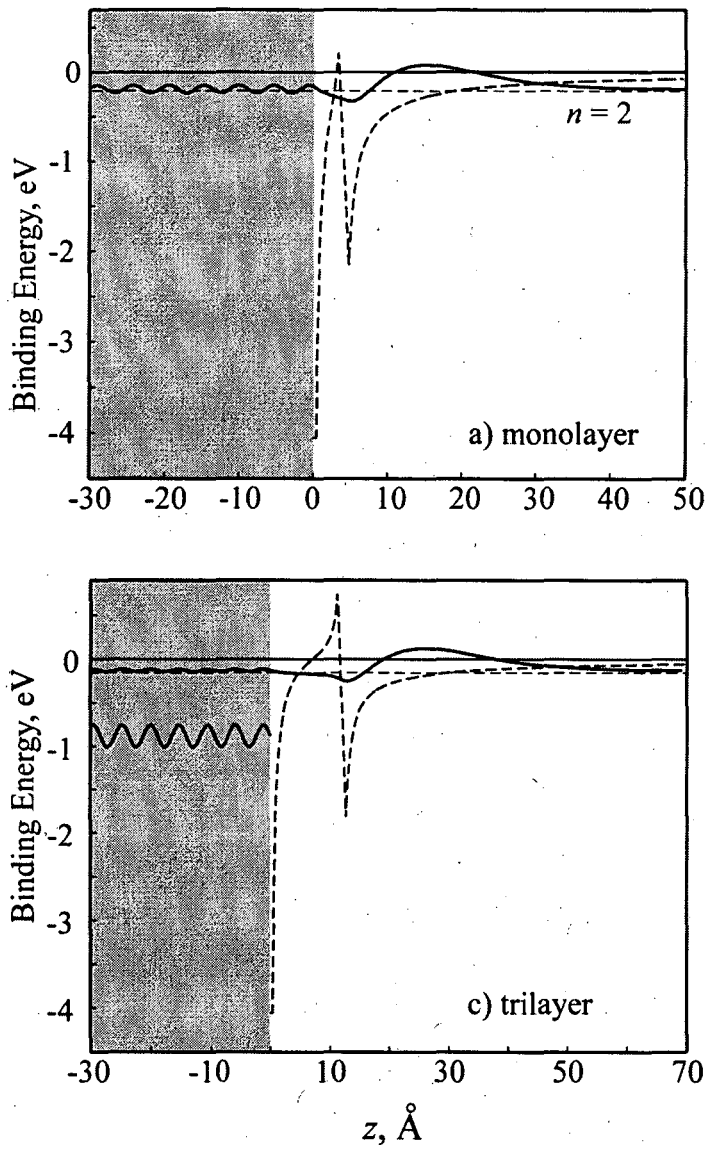

Figure 5.5. Calculated $n = 2$ wavefunction as a function of layer thickness for one and three layers of n-heptane on Ag(111). The wavefunction in the metal is no longer evanescent since $n = 2$ is degenerate with the Ag(111) conduction band. The wavefunction inside the substrate for a trilayer is multiplied by a factor of 10 for clarity.

$n = 1$ in the metal substrate are also shown. The calculated probability density of $n = 1$ in the metal substrate for a monolayer, bilayer and trilayer of n-heptane are 0.018, 0.0015, and 0.00014, respectively. The parameters used were determined from bulk values of n-octane where $\varepsilon = 2.0$, $V_0 = 0.2\,\text{eV}$, and the interplanar distance is 4 Å. As a reminder, the metal substrate band structure is approximated using the NFE model. The most salient effect of the n-heptane on the image state wavefunction is the exclusion of the wavefunction from both the metal substrate and the overlayer. For the comparison to the $n = 1$ wavefunction, the calculated wavefunction for $n = 2$ as a function of layer thickness is shown in Figure 5.5. In this case, the wavefunctions do not decay into the metal substrate since $n = 2$ is still degenerate with the conduction band even after a workfunction decrease of 0.5 eV upon adsorption of n-heptane on Ag(111). As a result, the use of the NFE model in determining the $n = 2$ lifetime is no longer valid.

The lifetime of $n = 2$ in the presence of a dielectric material with a negative electron affinity can be deduced using the classical period of motion that was discussed in Chapter 4 and a tunneling model. The classical oscillation period of the electron T_{cl} out in the vacuum constitutes an "attempt rate" for tunneling through the potential barrier of the adlayer. The tunneling probability P is governed by the layer thickness and the electron affinity, the barrier height, of the overlayer. The lifetime of the electron is comprised of these two factors and is equal to the following expression:

$$\tau = T_{cl} P^{-1}. \tag{5.4}$$

Cole used the WKB approximation to determine the tunneling probability and arrived at the following expressions[106]:

$$P = e^{-2J}, \tag{5.5}$$

$$J = \int_0^d \left(\frac{2m[V_{in}(z) - E]}{\hbar^2} \right)^{1/2} dz$$

$$= \left(\frac{8m(V_0 - E)d^2}{\hbar^2} \right)^{1/2} \left\{ (1 - y^{-2})^{1/2} - y^{-2} \ln[y + (y^2 - 1)^{1/2}] \right\}, \tag{5.6}$$

where $y^2 = 4d\varepsilon(V_0 - E)/e^2$. The classical oscillation period is determined by the potential between the classical turning point at the adlayer surface and the classical turning point of V_{out} out in the vacuum. The expression for T_{cl} can, therefore, be determined by:

$$T_{cl} \approx \frac{1}{2}\left(\frac{2m[z_m - d]}{V'_{out}(z_m)}\right)^{1/2}, \tag{5.7}$$

where z_m is the classical turning point on the vacuum side and $V'_{out}(z_m)$ is the derivative of the potential with respect to z. The presence of the dielectric material reduces the restoring force of the Coulomb potential as compared to the clean surface. The reduced restoring force of the modified Coulomb potential will allow the electron to spend more time out in the vacuum that results in a longer image state lifetime. The classical oscillation period, however, is only a pre-exponential factor to the lifetime(Equation 5.4) and becomes insignificant as the layer thickness increases. In order to determine the image state lifetime at the n-heptane/Ag(111) interface, the calculated lifetime from Equation 5.4 must be scaled by the measured clean surface lifetime. The clean surface n = 2 and 3 lifetimes, however, cannot be used for scaling purposes since their lifetimes are affected by the degeneracy with the conduction band. It has been shown that the n = 2 and 3 lifetimes scale less than n^3 with respect to n = 1 and was determined to be $\tau_{n=2}/\tau_{n=1} \approx 4$ and $\tau_{n=3}/\tau_{n=1} \approx 12$ [123]. The lifetime of the image state is then determined by the following expression:

$$\tau^{adlayer} = \tau^{bare}\left(\frac{T_{cl}^{adlayer}}{T_{cl}^{bare}}\right)\left(\frac{P^{bare}}{P^{adlayer}}\right), \tag{5.8}$$

where we have assumed that P^{bare} = 1. The lifetime calculated for the $n = 1$ and $n = 2$ states as a function of layer thickness are shown in Figure 5.6 along with the experimentally determined values using the two methods described above. For the $n = 1$ state both the lifetime results determined by the probability density in the metal and the classical oscillation/tunneling barrier method are also shown.

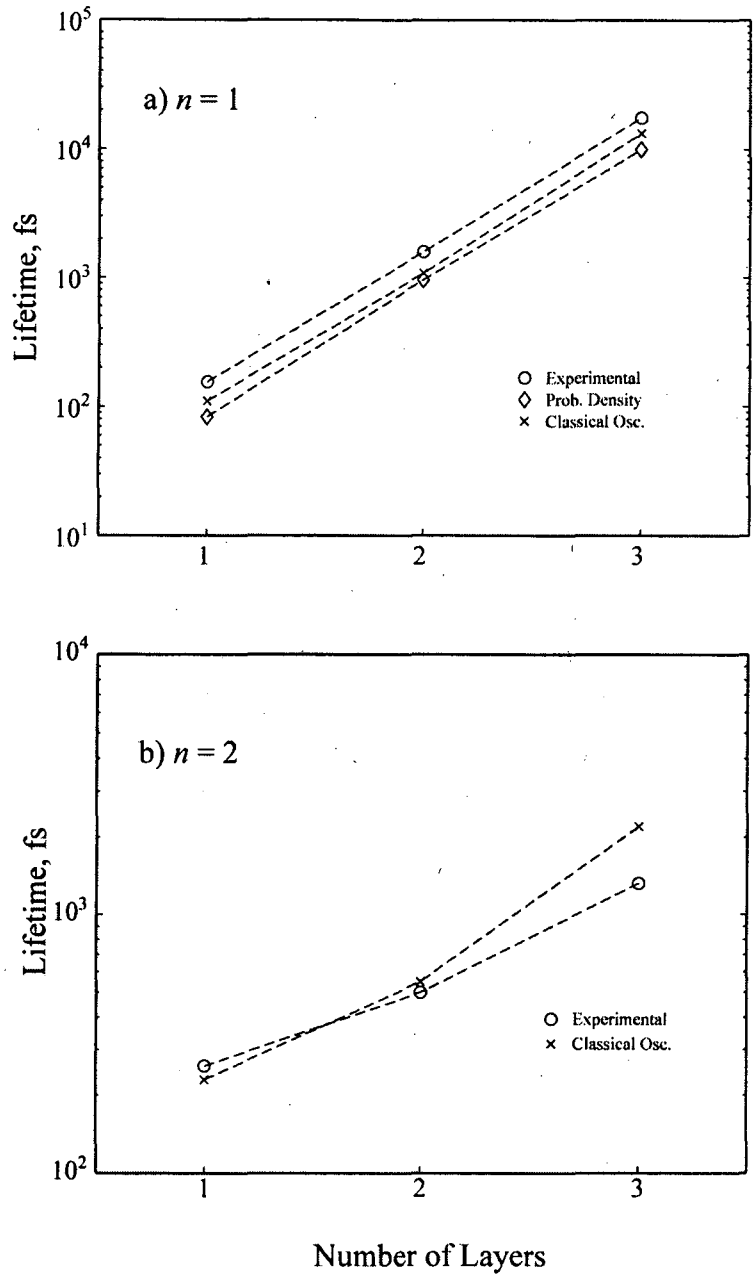

Figure 5.6. Experimentally determined and calculated lifetimes of $n = 1$ and 2. The lifetimes of $n = 1$ and 2 were deduced by determining their classical oscillation period out in the vacuum and the tunneling probability through the layer thickness. The lifetime deduced by calculating the probability density using the NFE model is also shown for $n = 1$.

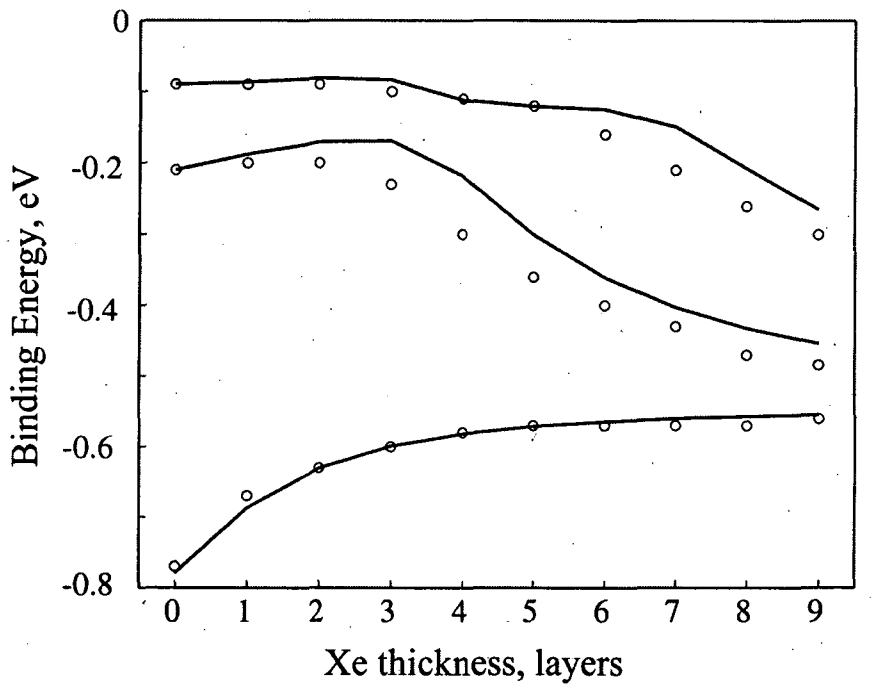

Figure 5.7. Comparison between experimental binding energies for the n = 1, 2, 3 states as a function of layer thickness of Xe(symbols) and the prediction of the quantum well model using the potential shown in Figure 5.2.

5.3 Interband Electron Dynamics at the Xe/Ag(111) Interface

Experimentally determined and calculated binding energies as a function of Xe coverage are plotted in Figure 5.7. Adsorption of a monolayer of Xe decreases the work function by 0.5 eV, which also lowers the n = 1 state to about 0.5 eV below the Ag(111) conduction band minimum and places the n = 1 state further into the band gap. The adsorption of a monolayer of Xe changes the binding energy of n = 1 from –0.77 to –0.68 eV. The n = 1 state, however, is still 0.18 eV below the Xe conduction band minimum. The n = 2 and 3 states, on the other hand, are energetically above the Xe conduction band minimum. These energy levels are shown in Figure 5.8. The experimental results reveal that the binding energy of the n = 1 state decreases by 16% over the range of one to nine layers of Xe. The calculation of the n = 1 wavefunction for a range of Xe coverage shown in Figure 5.9 illustrates that the n = 1 electronic wavefunction is pushed further from the metal substrate by the Xe potential. These results were calculated using a potential represented by Equation 5.3 with $V_{CB,Xe} = -0.55\,\text{eV}$, $\varepsilon = 3.0$, and an interplanar distance of 3.577Å. This affects the n = 1 image state lifetimes since the wavefunction overlap with the metal substrate decreases as the electron probability density is further away from the metal just like in the case of n-heptane on Ag(111). In contrast, the n = 2 and 3 binding energies monotonically increase, as expected for the formation of the Xe conduction band QW. The important difference between the n = 1 state and n = 2, 3 states is that n = 1 is energetically within the Xe band gap, while the n = 2 and 3 states are degenerate with the Xe conduction band. Calculations show that the n = 2 and 3 states evolve into the Xe conduction QW states by moving into the Xe layer. Calculated wavefunctions for n = 2 are also shown in Figure 5.9. At six layers of Xe, the n = 2 wavefunction almost completely move into the Xe layer.

The clean Ag(111) n = 1 image state lifetime was determined to be 32 ± 6 fs at 50 K. Upon adsorption of a monolayer of Xe, the lifetime of n = 1 increases to 240

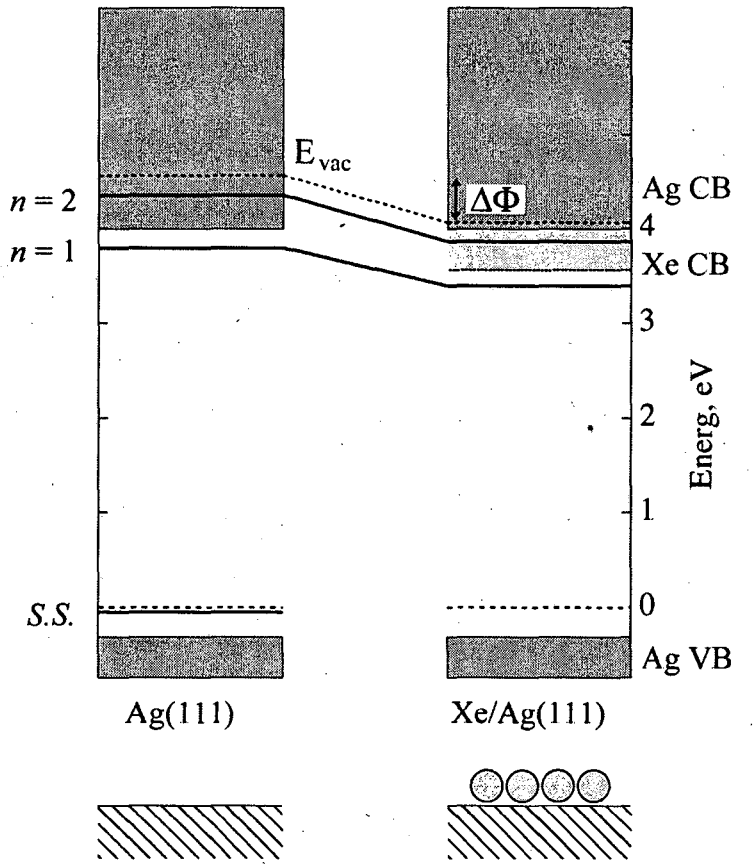

Figure 5.8. The adsorption of a monolayer of Xe decreases the work function of Ag(111) from 4.56 to 4.06 eV. This places the n = 1 state about 0.5 eV below the Ag(111) conduction band minimum, meanwhile, its energy is about 0.18 eV below the Xe conduction band minimum. The $n \geq 2$image states, however, are energetically above the Xe conduction band.

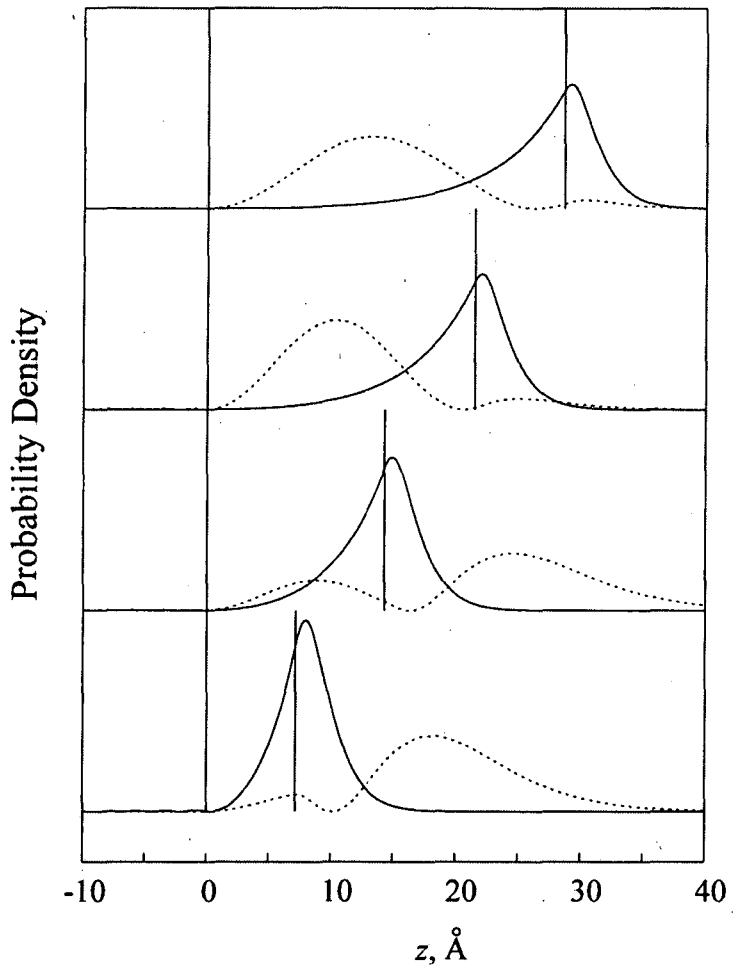

Figure 5.9. Resulting probability densities for the dielectric continuum model for the n = 1(solid lines) and n = 2(dashed lines) states for two, four, six, and eight layers of Xe on Ag(111). The bulk dielectric constant of ε = 3.0 and electron affinity of 0.55 eV were used. This figure illustrates the tendency of the n = 1 state to have significant wavefunction density at the dielectric/vacuum interface rather than in the dielectric slab. Meanwhile, the n = 2 state looks like a hydrogenic n = 2 image state at lower coverages but tends to move inside the layer and have a node near the dielectric/vacuum interface, which is indicative of a quantum well state of the Xe conduction band, for thicker layers.

fs(Figure 5.10). Overlapping features for multilayer and low signal levels at high Xe coverage limited the time-resolved TTPE spectra to one to six layers of Xe. The best fit to the data requires a short exponential rise, which we assume to be attributed to intraband relaxation. A portion of the rise time, however, may be due to the coherence dephasing as discussed in Chapter 4. The $n = 1$ lifetime increases monotonically with each additional layer of Xe and reaches an asymptotic value of about 800 fs above four layers. The calculated lifetime of $n = 1$ increases exponentially since the Xe overlayer potential is represented by a square well. This model does not capture the essential physics that governs the $n = 1$ lifetime after four layers of Xe as will be discussed toward the end of this chapter. The lifetime of the $n = 2$ and 3 states exhibits lifetime oscillations as a function of layer thickness, which is caused by a quantum size effect(Figure 5.10). An understanding of these oscillations can be gained by considering the perpendicular expectation value for the hydrogenic image states. The expectation value of z for $n = 2$ is about 13Å. By looking at the wavefunction of the $n = 2$ image state in Figure 5.9, the crossover of the $n = 2$ image state to a QW state appears at a Xe layer thickness of four layers. Four layers of Xe correspond to a thickness of about 14 Å. This result can be interpreted as follows. For the monolayer, the states are only slightly perturbed from those of the clean surface because of the small spatial overlap of the layer potential with the hydrogenic(zero-order) wavefunction. When the layer is thick enough for significant overlap with the zero-order hydrogenic wavefunction where $d \approx \langle z \rangle$, the image state moves into the layer and the energy is brought down by the attractive Xe layer potential. Since $n = 3$ has $\langle z \rangle \approx 29$ Å, its binding energy is significantly brought down in the range of seven to nine layers. It is also interesting to note that the $n = 2$ lifetime has a minimum at four layers of Xe. Since the $n = 2$ wavefunction can move into the Xe layer at four layers, this allows the wavefunction to be closer to the metal and to increase its overlap with the metal substrate. This higher wavefunction penetration in the metal substrate reduces the lifetime of the $n = 2$ image state, and we see a dip in its lifetime at four layers of Xe(Figure 5.10). After a dip in the lifetime of $n = 2$, the lifetime starts to increase again. The increase in the $n = 2$ lifetime at higher coverage indicates the spreading of the $n = 2$ wavefunction in the Xe overlayer as discussed in Section 2.2

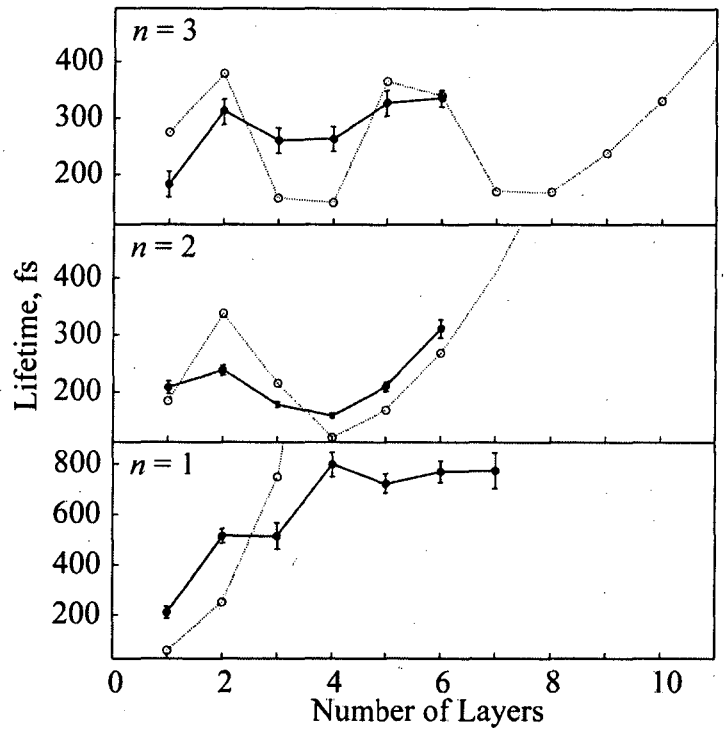

Figure 5.10. Lifetimes of the n = 1, 2, and 3 states for one to six layers of Xe extracted from the time-resolved data (filled circles). Lifetime predictions taken from the 1-D flat potential model (open circles) are in qualitative agreement with the oscillations in lifetime apparent in the data. The experimental error bars are calculated for a 95% confidence limit. The solid and dotted lines are only guide to the eyes for experimental and calculated lifetimes, respectively.

As shown in Figure 5.10, the calculated lifetime of $n = 1$ increases exponentially as a function of layer thickness when using a flat potential for the Xe layer. A more appropriate approximation of the Xe potential experienced by the $n = 1$ electron is given by Equation 5.2. The potential of the Xe layer as given by Equation 5.2 will allow the $n = 1$ wavefunction to reside in the layer. As the layer thickness increases, the $n = 1$ is no longer located in the vacuum and is mainly located in the screened Coulomb potential of the layer as shown in Figure 5.11. This is manifested in a relatively constant lifetime after four layers of Xe. Figure 5.11 depicts the wavefunctions of $n = 1$ for one, three and five layers of Xe. The dotted lines denote the location of the Xe layer boundary. Figure 5.12 reveals the calculated binding energy and lifetime of $n = 1$ as a function of layer thickness using the potential given by Equation 5.2. The binding energy becomes more accurate at higher coverage. The calculated lifetime, however, was scaled by a factor of twelve in Figure 5.12b. The calculated lifetime approaches an asymptotic value after four layer of Xe, which shed some light on the physics that determines $n = 1$ lifetime at higher coverage. The same effect has been observed in the study of electron dynamics at the Benzene/Ag(111) interface[124]. The constant lifetime after four layers of Xe reveals that the electron density is trapped by the screened Coulomb potential in the layer and is not pushed out further into the vacuum with increasing layer thickness.

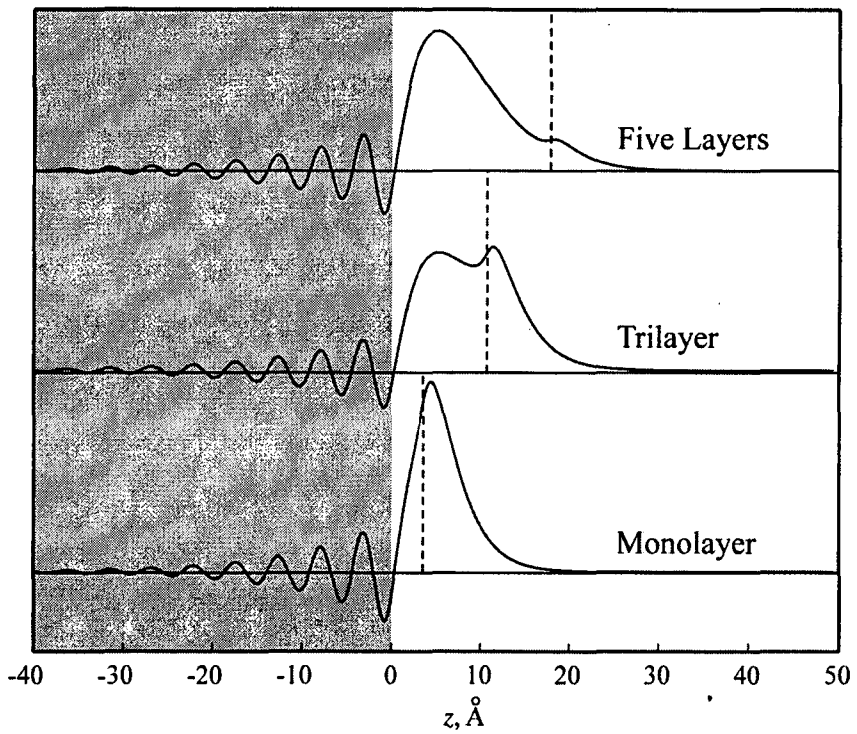

Figure 5.11. Wavefunction of n = 1 for monolayer, trilayer, and five layers of Xe determined using Equation 5.1 and Equation 5.2 to represent the potential at the dielectric/metal interface. The dotted lines denote the Xe layer boundary. The wavefunction of n = 1 has a tendency to move into the layer and evolve very slightly after five layers.

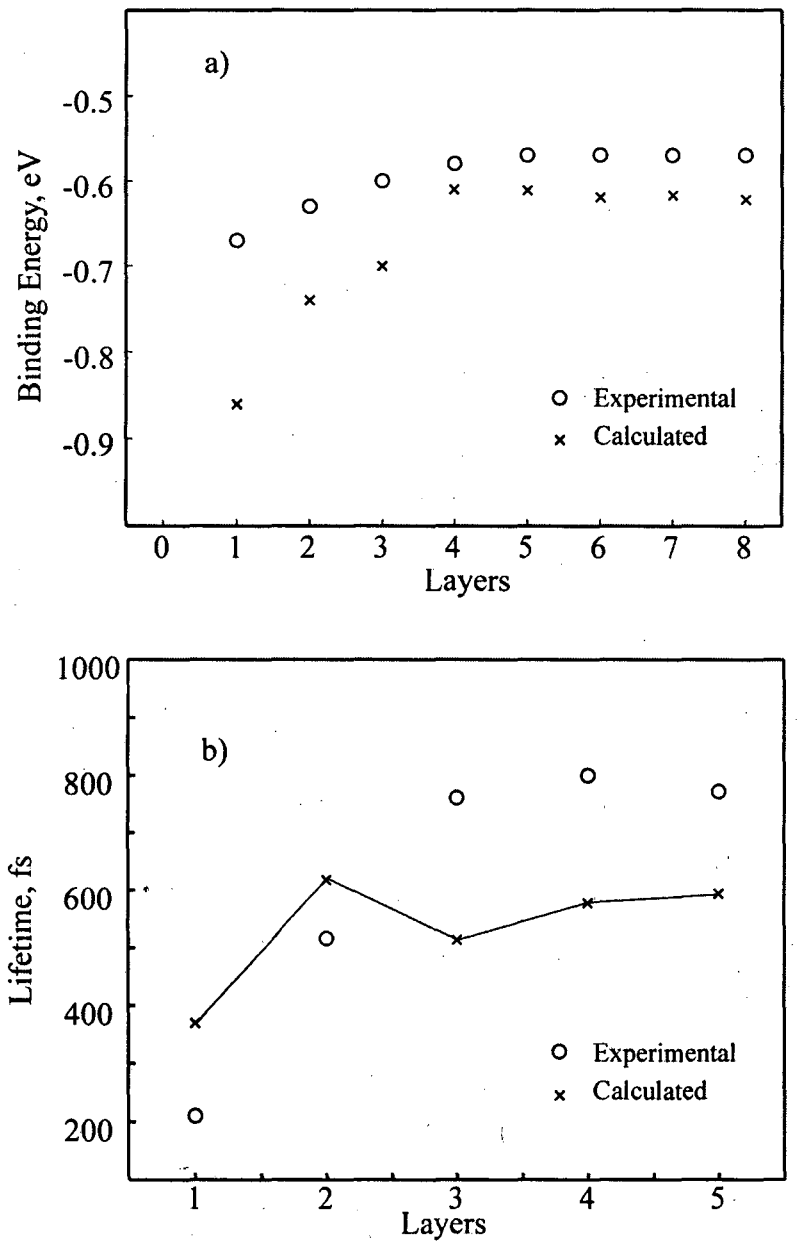

Figure 5.12. Comparison of the experimental and calculated binding energy(a) and lifetime(b) using Equation 5.1 and 5.2 to represent the overlayer potential of Xe. The binding energy becomes more accurate at higher coverage. The calculated lifetimes, however, must be scaled up by a factor of twelve in the figure in order to make a comparison between theory and experimental results.

Chapter 6

Two Dimensional Electron Dynamics

A deeper understanding of the electron dynamics in the degrees of freedom parallel to a metal-dielectric interface is technologically significant such as in the areas of organic light-emitting devices[125] and electron transport in mesoscopic materials[107,126]. The ability to grow thin layers of insulating materials on surfaces provides a means to control the spatial extent of the surface electronic wavefunction which determines both the interband and intraband relaxation of a surface electron. In bulk materials, the physics that governs the transport properties of charge carriers in dielectric solids is markedly different than in metals owing to the strong polarization interaction of the dielectric with electrons and their highly deformable lattice. An electron in a metal is usually free-electron-like, whereas in a dielectric solid, self-trapping is the norm as this process has been reviewed by Song and Williams for self-trapped excitons[127]. An excellent book on the study of polarons has also been written by Alexandrov and Mott[128]. In the study of carrier transport in dielectric materials, questions regarding how the dimensionality and electron confinement affect electron transport arise. By growing insulating materials on a metal substrate in a layer-by-layer fashion, two-dimensional carrier dynamics can be investigated in a controlled fashion. In addition, questions regarding how the separation of the electron from the metal substrate alters the electron dynamics in the degrees of freedom parallel to the surface can be answered. Finally, the transition of the electronic transport properties from thin films all the way to the bulk of the dielectric materials can be studied.

The lifetime of image state electrons shows strong parallel momentum dependence. The analysis of the interband relaxation process via the penetration of the electron wavefunction discussed in Chapter 5 does not explain the strong parallel momentum dependence of the image state lifetimes. The wavefunction penetration

should be dependent on $k_{\parallel}$, since the energy of the state with respect to the conduction band minimum changes as a function of parallel momentum as shown in Figure 2.2. The change in the image state wavefunction overlap off the zone center can only account for a faster interband relaxation rate of a few percent for $n = 1$ at the Xe/Ag(111) interface for the small $k_{\parallel}$ values(< 0.25 Å^{-1}) in this study. As discussed in Chapter 5, the negative electron affinity of n-heptane drastically reduces the interaction of the image electron with the metal substrate and the electron mainly interacts with the insulating material at the dielectric/vacuum interface. At the n-heptane/Ag(111) interface, electron-phonon interaction of the electron with the adsorbed layer significantly alters the image state dynamics and electron self-trapping occurs. In this chapter, we will explore the dynamics of image state electrons in the parallel degrees of freedom at both the Xe/Ag(111) and n-heptane/Ag(111) interfaces. It will be shown below that the high mobility of electrons in bulk Xe increases the mobility of an image electron in the direction parallel to the surface as the number of Xe layer increases[34], whereas the strong polarization interaction of the image electron with the n-heptane layer results in the self-trapping of the image electron into a small polaron state[23,24].

6.1 Self-Trapping of Image Electrons

At the n-heptane/Ag(111) interface, excitation of electrons into image states creates excess electrons at the interface. Angle resolved TPPE provides a powerful tool to measure the dispersion of image states. The normally dispersive image states at the clean metal surface are significantly influenced by the alkane overlayer. Besides observing the normally dispersive feature of the $n = 1$ state, a non-dispersive feature was also observed and is attributed to the self-trapping of the $n = 1$ image electron(Figure 6.1). The localization of the electron signifies a strong coupling between the electron and its environment that results in a large effective mass of the electron as mentioned in Section 2.3. This feature, however, was not observed in neo-pentane, which has a higher electron mobility as compared to n-heptane or any straight-chained alkanes[79,98]. The mobility of an excess electron in liquid n-pentane is about 0.20 cm^2/V sec, whereas in

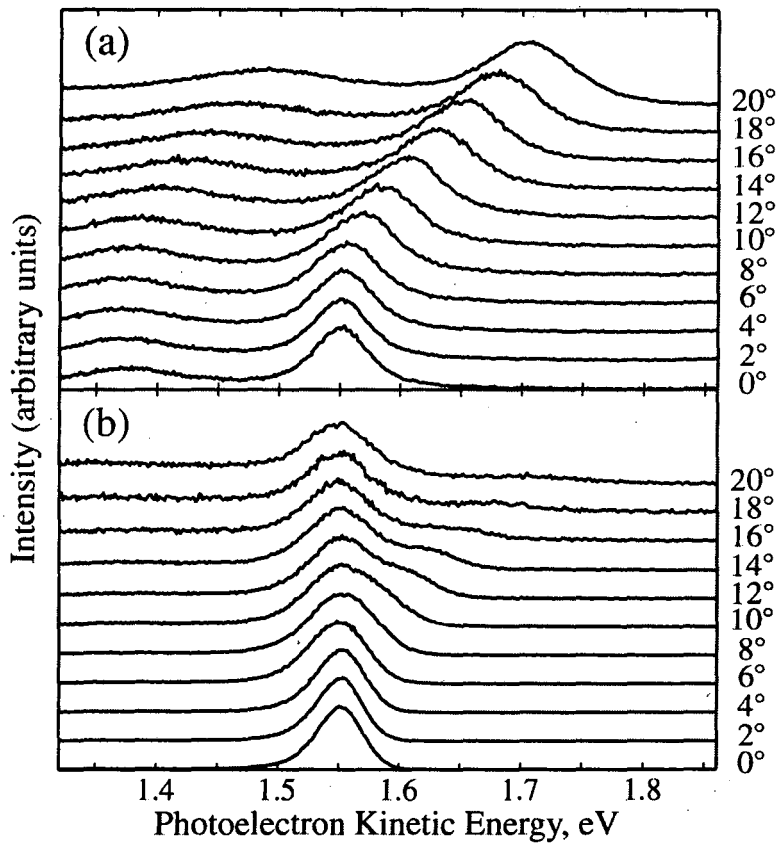

Figure 6.1. Femtosecond angle-resolved TPPE spectra for a bilayer of n-heptane on Ag(111) taken at (a) 0 fs and (b) 1670 fs pump-probe delay time. Initially, the electron is in the delocalized state. After a few hundred femtoseconds, the electrons become localized as manifested by the non-dispersive character of the state as a function of angle.

liquid neo-pentane is about 70 cm^2/V sec[129]. Excess electron mobility in liquid Xe is about two orders of magnitude higher than in liquid neo-pentane. In our study of electron dynamics at dielectric/metal interfaces, a non-dispersive feature was never observed at the Xe/Ag(111) interface even for coverage beyond five layers where the Xe layer must exhibit considerable disorder. The time scale of the localization process is shown in Figure 6.1, which stresses the importance of the interband relaxation time in allowing self-trapping to occur. In other words, if the image electron is short lived, then the probability of self-trapping diminishes. The dispersive feature as shown in Figure 6.1a was taken at a pump-probe delay time of 0 fs. The initially delocalized electrons localize within a few hundred femtoseconds as shown in Figure 6.1b that was taken at 1670 fs pump-probe delay. After about a picosecond, the dispersive feature mostly decayed away leaving the non-dispersive state to be dominant in the spectra. These spectra were taken at 120 K for a bilayer of n-heptane on Ag(111). The difference in energy between the delocalized $n = 1$ state and the localized state is $\leq$ 10 meV. This energy difference is independent of layer thickness which demonstrates the two-dimensionality of the localization process.

The dynamics of the localized and delocalized features as a function of angle are exhibited in Figure 6.2. In Figure 6.2a, a rise time of 360 fs and a decay time of 1600 fs were determined for the localized state. Both the rise time and decay time were independent of angle which is evident for the dynamics of a single localized state. In contrast, the delocalized $n = 1$ state shows a strong parallel momentum dependence whose decay time is on the order of the rise time of the localized state. The temperature study of the electron dynamics at 50 K also reveal a faster rise time of the localized state, which demonstrates a reverse temperature dependence of the localization process. This localization process is attributed to the self-trapping of the image state electron into a small polaron[23].

An excess electron in a deformable lattice creates an attractive potential well by displacing the atoms that surround it. The trapping of the electron in the self-induced potential well is termed a polaron. A polaron is characterized as a small polaron when the spatial extent of the wavefunction of the excess electron or the hole is less than or comparable to the lattice spacing. The notion of a polaron was first set forth by Landau

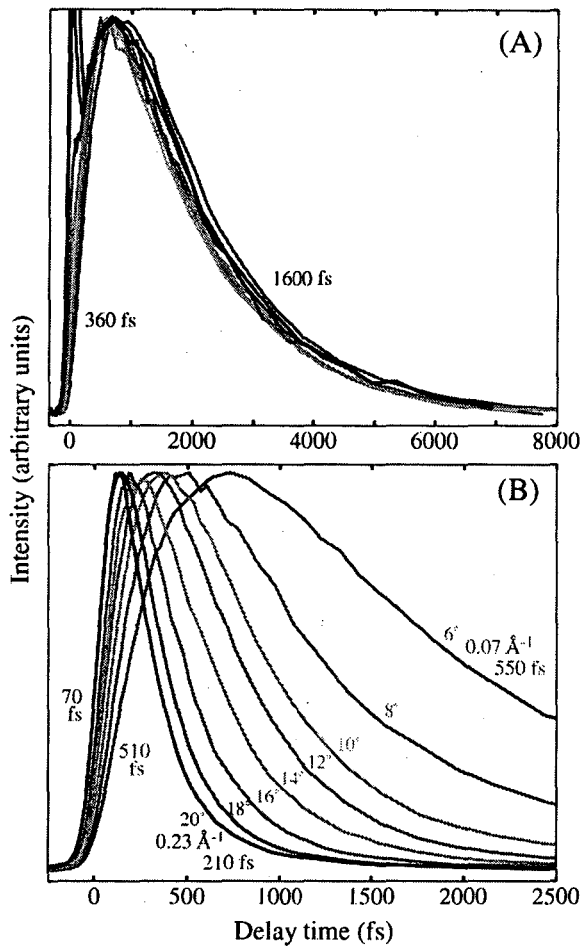

Figure 6.2. Femtosecond time-resolved TPPE traces for (A) the delocalized and (B) the localized state for bilayer n-heptane on Ag(111) at various angles. The spikes near time zero in (A) for data at high angles may come from short-lived electrons on small patches of monolayer.

in 1932. In recent years, there have been rapid increases in evidence supporting the existence of polarons[130]. An interesting observation of polaron formation is manifested in the injection of excess electron into liquid ammonia which produces a blue color upon forming small polarons[131]. Small polarons often have opposite properties as compared with quasi-free charge carriers. The strong interaction of the electron with its surrounding atoms results in a mobility of less than 1 cm^2/V sec for small polarons and has a reverse temperature effect, where the mobility increases with temperature. The increase in the mobility as a function of temperature is a manifestation of the hopping mechanism in the transport of charges trapped in a small polaronic state.

The self-induced potential well of the deformable lattice can be characterized as either short-range or long-range, which mainly arises from electron-acoustic phonon coupling and electron-optical phonon coupling, respectively. Long-range potential involves moderate deformation of the lattice and typically occurs in ionic crystals. Small polaron is formed by larger displacement of atoms and molecules in the crystal that results from the short-range potential. The strength of the electron-acoustic phonon coupling is measured by the deformation potential. Besides the importance of the short-range and long-range coupling in determining whether self-trapping occurs, the dimensionality of the system is also important[127]. It has been shown that localization is energetically more favorable than delocalization for short-range electron phonon coupling in 1-dimension, while delocalization is energetically favorable in 3-dimensions. The 2-dimensional case is often referred to as the marginal case.

The self-trapping dynamics of the image electron at the n-heptane/Ag(111) interface has been discussed in great detail elsewhere[123] and will only be described briefly below. The readers are referred to Reference 123 for further details. A configuration coordinate diagram is shown in Figure 6.3 where each curve in the $V_f(k_{\parallel},Q)$ manifold represents a different $k_{\parallel}$ state and $V_s(Q)$ is the self-trapped state. To localize the electron without lattice distortion along the $Q=0$ axis, the energy requirement is approximately half the bandwidth(B) as determined by the increase in energy upon localizing the electron to the order of a lattice constant. Introducing lattice distortion will allow the electron to induce an attractive potential which stabilizes it(point

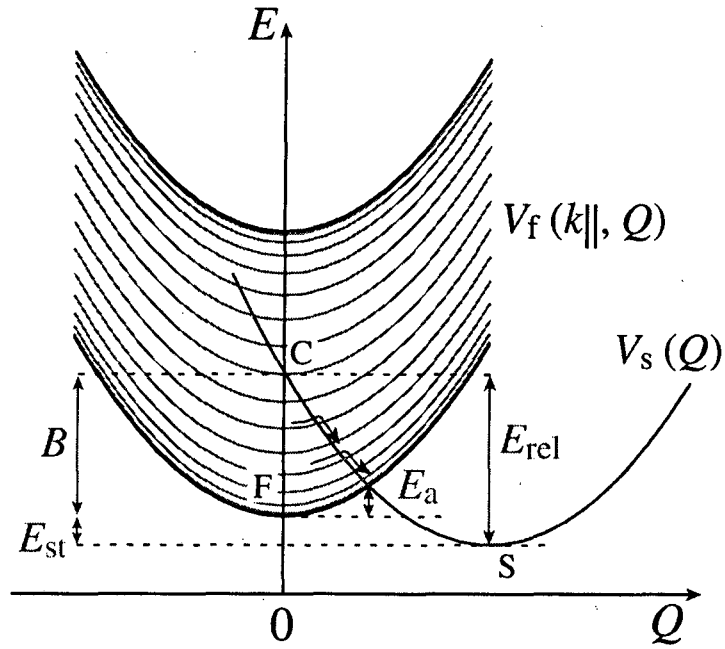

Figure 6.3. Configuration coordinate diagram for self-trapping of an electron. Curves $V_f(k_{\|},Q)$ and $V_s(Q)$ are associated, respectively, with the free states and the self-trapped state. The quantity Q is the phonon coordinate responsible for self-trapping. Each curves in the $V_f(k_{\|},Q)$ manifold represents a different $k_{\|}$ state. The half-width of the band B or the localization energy, lattice relaxation energy E_{rel}, self-trapping energy E_{st}, and the activation E_a are depicted.

S). If the lattice relaxation energy (E_{rel}) is greater than half of the bandwidth, self-trapping will occur. In other words, $E_{st} \equiv E_{rel} - B$ must be positive in order for the self-trapped state to be energetically favorable. It can also be shown via this model that the self-trapping rate is increased with increasing $k_{\parallel}$ until point C is reached where it is referred to as the Marcus inverted region[132]. Only a monotonic increase in the decay of the delocalized $n = 1$ state was observed in our study. The self-trapping dynamics has been analyzed using a path integral technique, which accounts for both the adiabatic and non-adiabatic processes of the electron transfer process[23,123]. In the analysis of the self-trapping of image electrons, the rate of decay of the delocalized electron was assumed to have no contribution from the intraband relaxation process. It will be shown in the next section that momentum relaxation may play an important role in the dynamics of image electrons in the degrees of freedom parallel to the surface.

6.2 Intraband Relaxation of Image Electrons at the Xe/Ag(111) Interface

Some of the first studies of image state electron mobility were done during the early 1970's by Sommer and Tanner[133], and Williams, Crandall and Willis[134] by using either a time-of-flight method to measure the electron mobility or by removing the holding field and measure the charge remaining at the liquid helium surface after a few microseconds. It was found definitively by Brown and Grimes via cyclotron frequency measurements that the mobility of electrons residing on the liquid He surface follows a 2-Dimensional model which is an inherent characteristic of image states[135]. The wavefunction of the image state electron at the surface of liquid helium has an infinitesimal penetration in the liquid helium as a result of the exclusion principle. The mobility of the electron is limited by electron-He scattering at the surface and has been theoretically studied by Cole[136,137]. Electron mobility was also measured for electrons residing at the surface of solid hydrogen and its limit was attributed to electron scattering by microscopic surface defects[138]. Other 2-Dimensional electron systems such as at the semiconductor surface inversion layers have been studied both theoretically

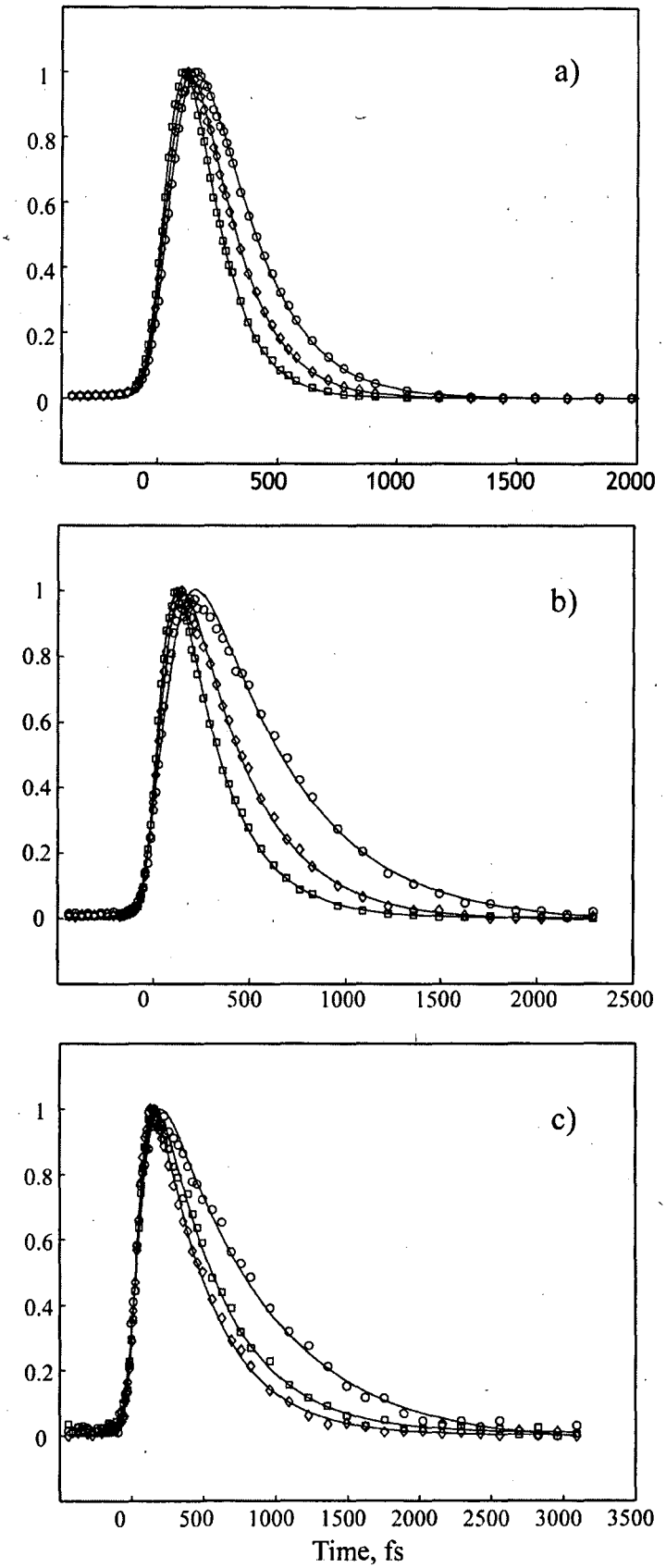
a)
b)
c)
1
0.8
0.6
0.4
0.2
0
0
500
1000
1500
2000
2500
3000
3500
Time, fs

Figure 6.4. Dynamics traces of $n = 1$ as a function of parallel momentum and layer thickness. a) Monolayer of Xe with circles, diamonds, and squares representing the dynamics traces for 0, 0.09, and 0.15 $Å^{-1}$, respectively. b) Bilayer of Xe with circles, diamonds and squares representing the dynamics for electrons with parallel of 0, 0.09, and 0.18 $Å^{-1}$, respectively. c) Trilayer of Xe with circles, diamonds, and squares representing 0, 0.09, and 0.16 $Å^{-1}$, respectively.

and experimentally from conductance measurements and electron mobility determined by Hall effect or magneto-resistance measurements[1,139]. The momentum relaxation time can be deduced through these macroscopic measurements, but they can only give the steady-state momentum relaxation time of all the electrons in the 2-Dimensional band. In our study using angle resolved photoemission, the momentum relaxation time is determined for electrons with a specific parallel momentum. Because of the low laser fluence of our experiment, the number of electrons excited into the image state band is minimal and electron-electron interaction within the band is neglected. A two dimensional electron gas should not be formed after exciting the electrons into the image state band. In addition, the study of the momentum relaxation as a function of layer thickness provides a means to isolate the contribution of different parts of the potential at the interface in causing electron momentum relaxation.

6.2.1 Intraband Relaxation Results

The lifetimes of both $n = 1$ and $n = 2$ for a monolayer, bilayer and trilayer of Xe were measured at various sample angles to study electron momentum relaxation as a function of layer thickness. Traces of the lifetimes at different $k_{\parallel}$ states for the $n = 1$ state are shown in Figure 6.4. For up to three layers of Xe on Ag(111), the lifetime decreases monotonically as the electron parallel momentum increases. The lifetime of the monolayer $n = 1$ decreases from 211±10 to 117±5 fs for $k_{\parallel} = 0$ and $k_{\parallel} = 0.18$ Å^{-1}, respectively. For the bilayer, the $n = 1$ state lifetime decreases from 557±50 to 254±20 fs for states with $k_{\parallel} = 0$ and $k_{\parallel} = 0.18$ Å^{-1}, respectively. The lifetime of the state decreases from 783±70 to 398±22 fs for states with $k_{\parallel} = 0$ and $k_{\parallel} = 0.16$ Å^{-1} upon adsorption of three layers of Xe. The rise time for the monolayer $n = 1$ state decreases from 60 to 37 fs for states with $k_{\parallel} = 0$ and $k_{\parallel} = 0.18$ Å^{-1}, respectively. For the bilayer, the rise time decreases from 86 to 42 fs. The rise time for a trilayer decreases from 93 to 52 fs for states with $k_{\parallel} = 0$ and $k_{\parallel} = 0.16$ Å^{-1}. These dynamics traces are shown in Figure 6.4

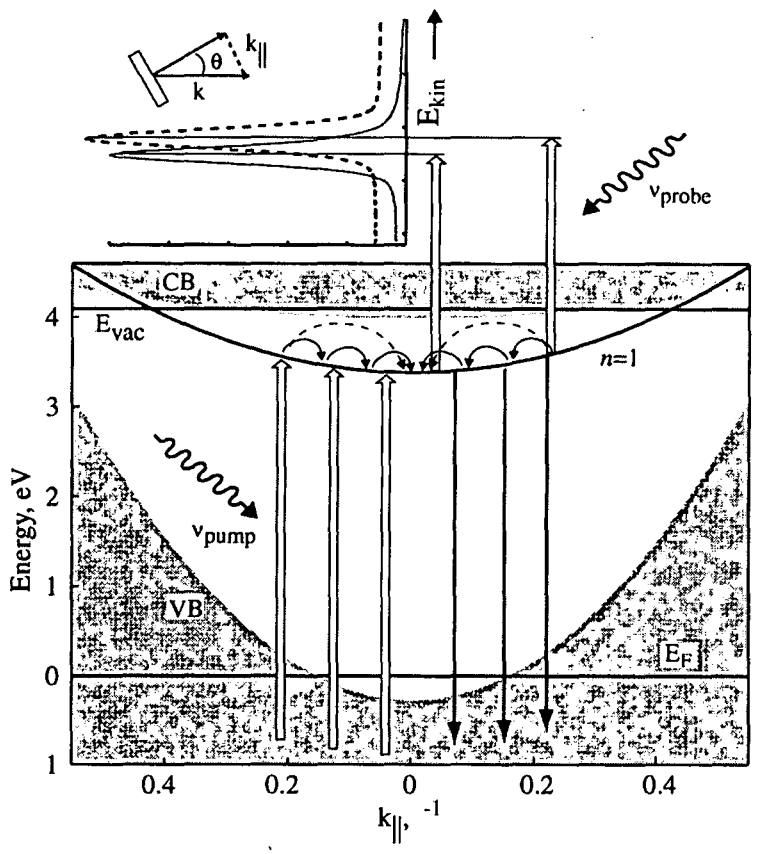

Figure 6.5. The *L*-gap PBBS of Ag(111) upon adsorption of a monolayer of Xe. The workfunction decreases to 4.06 eV and moves the $n = 1$ state further into the band gap. The left and the right side of the PBBS are used to illustrate the pumping and the probing process, respectively. Pump pulse (ν_{pump}) excites a distribution of $k_{||}$ states. Intraband relaxation processes occur after electron excitation into the image states, as shown by the curved solid and dashed arrows in the $n = 1$ image band. Interband relaxation can occur at every point in the $n = 1$ band, as shown by the downward solid-line arrows. Photoemission with the probe pulse (ν_{probe}) at various sample angles (θ) from the electron detector axis allows the mapping of the image state band and provides the opportunity to study electron momentum relaxation. k and $k_{||}$ are the total wave vector and parallel wave vector of the photoemitted electron, respectively.

Monolayer		Bilayer		Trilayer	
$k_{\parallel}$(Å^{-1})	lifetime(fs)	$k_{\parallel}$(Å^{-1})	lifetime(fs)	$k_{\parallel}$(Å^{-1})	lifetime(fs)
0.00	207±12	0.00	557±50	0.00	783±70
0.05	189±10	0.05	440±30	0.05	611±60
0.07	176±10	0.09	352±18	0.09	510±18
0.09	168±9	0.18	254±8	0.14	432±18
0.11	161±9	-	-	0.16	400±22
0.13	149±9	-	-	-	-
0.15	142±8	-	-	-	-
0.18	133±8	-	-	-	-
0.20	123±8	-	-	-	-

Table 6.1: $n = 1$ dynamics as a function of layer thickness and parallel momentum.

along with their best fit. The decrease in the rise time is consistent with a process that feeds population from higher momentum states into lower momentum states as depicted in Figure 6.5. The energy of the pump pulse at 305 nm will populate a distribution of $k_{\parallel}$ states all the way to the vacuum energy level at approximately $k_{\parallel} = 0.4$ Å^{-1} for $n = 1$. The electron dynamics results for $n = 1$ as a function of parallel momentum and layer thickness are tabulated in Table 6.1.

The decay pathways for states with finite parallel momentum can mainly be separated into two parts as follows. One can assume that the total lifetime depends on the interband relaxation and the intraband relaxation processes. Figure 6.5 shows these possible relaxation mechanisms for an image state electron. To separate out the intraband contribution to the lifetime, we first converted lifetimes to line widths. The total lifetime is related to the linewidth broadening due to the interband and intraband relaxation processes by

$$\Gamma_{\perp} + \Gamma_{\parallel} = \Gamma_T = \frac{660}{\tau} \text{ meV·fs}, \qquad (6.1)$$

where τ is the measured lifetime, $\Gamma_{\perp}$ is the line width attributed to interband relaxation, $\Gamma_{\parallel}$ is the line width contribution from intraband relaxation, and Γ_T is the total linewidth. The line width due to intraband relaxation $\Gamma_{\parallel}$ is calculated as follows. Assuming $\Gamma_{\perp}$ is

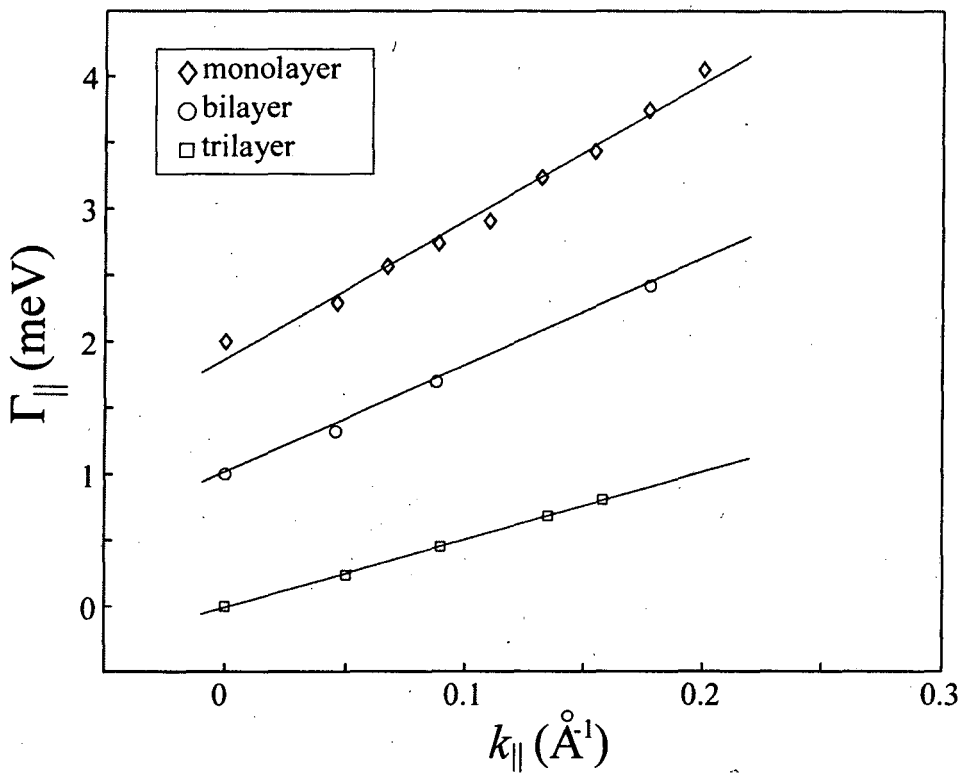

Figure 6.6. Linewidth as a function of parallel momentum of the $n = 1$ state for a monolayer, bilayer, and trilayer of Xe. The plot has a linear momentum dependence. The monolayer slope is steeper than the bilayer and trilayer, which shows that electrons are scattered more effectively for the monolayer Xe/Ag(111) interface. The slopes for the monolayer, bilayer, and trilayer are 11, 8, 5 meV·Å, respectively.

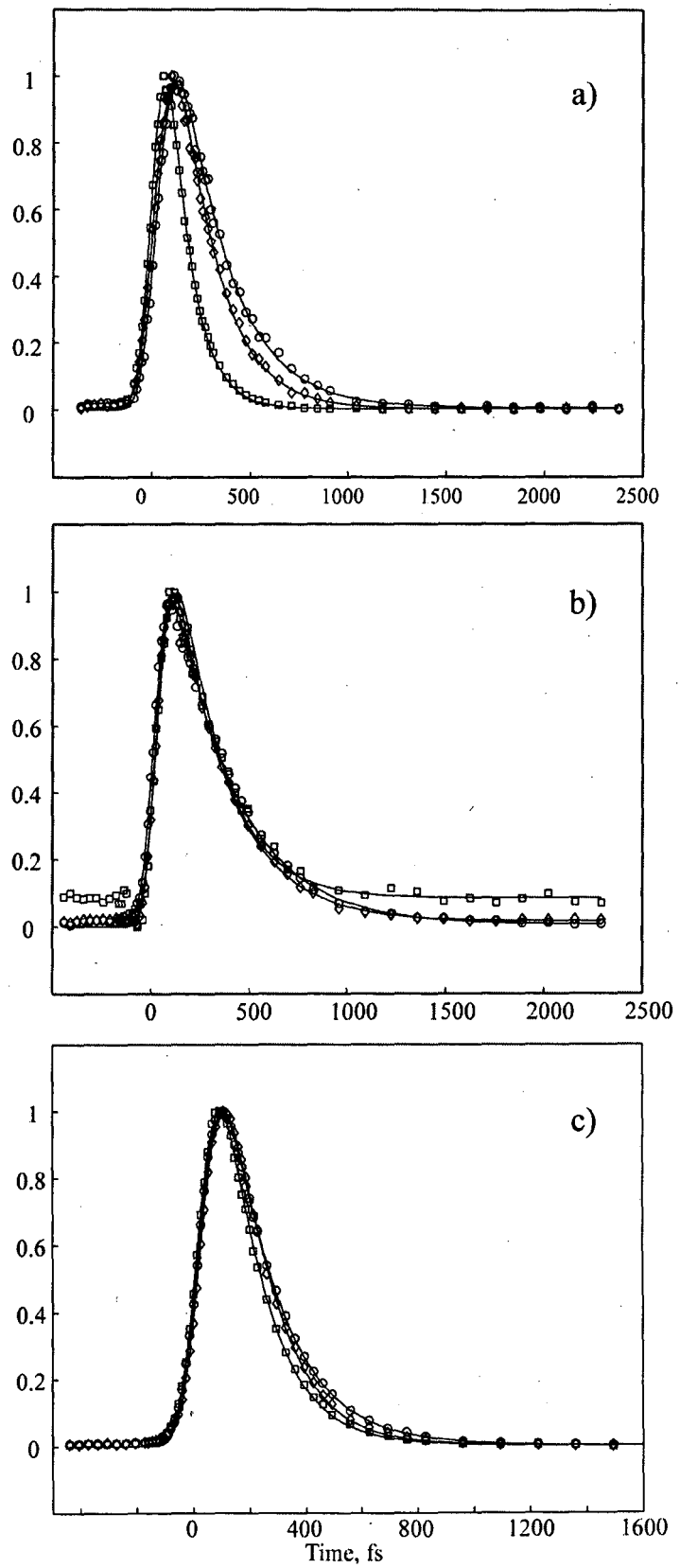
a)
b)
c)
1
0.8
0.6
0.4
0.2
0
0
500
1000
1500
2000
2500
400
800
1200
1600
Time, fs

Figure 6.7. Dynamics traces of $n = 2$ as a function of parallel momentum and layer thickness. a) Monolayer of Xe with circles, diamonds, and squares representing the dynamics traces for 0, 0.08, and 0.13 $Å^{-1}$, respectively. For the 0.13 $Å^{-1}$ dynamics trace, the $n = 2$ image band has crossed the Ag conduction band which results in a much faster decay. b) Bilayer of Xe with circles, diamonds and squares representing the dynamics for electrons with parallel of 0, 0.06, and 0.12 $Å^{-1}$, respectively. Notice that the dynamics only shows a slight change for increasing parallel momentum. This is reflected in the small slope for $n = 2$ for a bilayer of Xe. c) Trilayer of Xe with circles, diamonds, and squares representing 0, 0.05, and 0.10 $Å^{-1}$, respectively.

Monolayer		Bilayer		Trilayer	
$k_{\parallel}$(Å^{-1})	$\Gamma_{\parallel}$ (meV)	$k_{\parallel}$(Å^{-1})	$\Gamma_{\parallel}$ (meV)	$k_{\parallel}$(Å^{-1})	$\Gamma_{\parallel}$ (meV)
0.00	0.00	0.00	0.00	0.00	0.00
0.05	0.29	0.05	0.32	0.05	0.24
0.07	0.56	0.09	0.70	0.09	0.45
0.09	0.74	0.18	1.42	0.14	0.68
0.11	0.09	-	-	0.16	0.81
0.13	1.23	-	-	-	-
0.15	1.43	-	-	-	-
0.18	1.74	-	-	-	-
0.20	2.05	-	-	-	-

Table 6.2: $\Gamma_{\parallel}$ as a function of layer thickness and parallel momentum for $n = 1$.

independent of parallel momentum, $\Gamma_{\perp}$ is equal to Γ_T at $k_{\parallel} = 0\,\text{Å}^{-1}$. Using Equation 6.1, $\Gamma_{\parallel}$ is determined by subtracting $\Gamma_{\perp}$ from Γ_T for data taken off angle where the state has finite parallel momentum. These values are shown in Table 6.2 for $n = 1$. Linewidth due to intraband relaxation $\Gamma_{\parallel}$ as a function of parallel momentum is plotted in Figure 6.6. For thicker layers of Xe, the number of data points is more sparse since more scans must be taken to compensate for the reduced signal to noise ratio. In addition, the time of an experimental run is limited by how long a 100-liter Dewar of liquid helium will last. The ordinate for the bilayer and monolayer are offset by 1 and 2 meV, respectively, to improve the clarity of the figure. The slope in Figure 6.6 is a measure of the rapidity of the intraband relaxation as a function of $k_{\parallel}$. The slope for the monolayer, bilayer and trilayer are 11, 8 and 5 meV·Å, respectively, which suggest that $k_{\parallel}$ relaxation occurs faster for a monolayer than both the bilayer and trilayer.

The dynamics traces for $n = 2$ as a function of angle for up to three layers of Xe are shown in Figure 6.7. The intraband line width $\Gamma_{\parallel}$ as a function of parallel momentum is plotted in Figure 6.8a. In this figure, it is evident that at about $k_{\parallel} = 0.15\,\text{Å}^{-1}$ the line width increases drastically. This sudden jump in the decay rate is the result of band crossing of the $n = 2$ state into the bulk conduction band states. Two slopes are shown in the figure which also reveal the drastic change in the intraband relaxation rate as a

function of $k_{\parallel}$. It is important to note that this jump in the angle resolved lifetime is not observed for the $n = 2$ state at the n-heptane/Ag(111) interface, even when $n = 2$ is energetically above the Ag(111) conduction band. This result confirms that the image state electron probability density is mainly located at the n-heptane/vacuum interface owing to the negative electron affinity of bulk n-heptane. The linewidth representations of the $n = 2$ dynamics for a bilayer and trilayer of Xe on Ag(111) are shown in Figure 6.8b. Their slopes determined, with the limited number of data points for higher coverage and before the state crosses the conduction band for a monolayer, are 6, 4 and 10 meV·Å for a monolayer, bilayer, and trilayer, respectively. The data points for a trilayer of Xe are offset by 1 meV in Figure 6.8b. The important distinction between $n = 1$ and $n = 2$ is that the intraband relaxation rate as a function of $k_{\parallel}$ does not decrease monotonically. This should be compared to the oscillations in the interband relaxation rate as discussed in Chapter 5 for the higher order image state electrons. The lifetime and linewidth of $n = 2$ are recorded in Table 6.3 and Table 6.4, respectively.

6.2.2 Discussion

In order to understand the cause of the electron relaxation processes, it is important to determine the spatial extent of the image state electrons. The monotonic decrease in the slope of the momentum relaxation rate as a function of $k_{\parallel}$ for the $n = 1$ image state suggest that the Xe overlayer acts as a spacer layer which separates the charge from the substrate and consequently increases the mobility of the electron. Charge separation has led to extremely high transconductance in modulation-doped structures of GaAs/(Al,Ga)As heterojunction field-effect transistors as reviewed by Drummond, Masselink, and Morkoç[1]. The conduction path at the GaAs/(Al,Ga)As interface is a quantized two-dimensional electron gas with a gate-to-channel separation of about 100 atomic layers. The current studies reveal the limit of the electron mobility for a minimum thickness of a spacer layer.

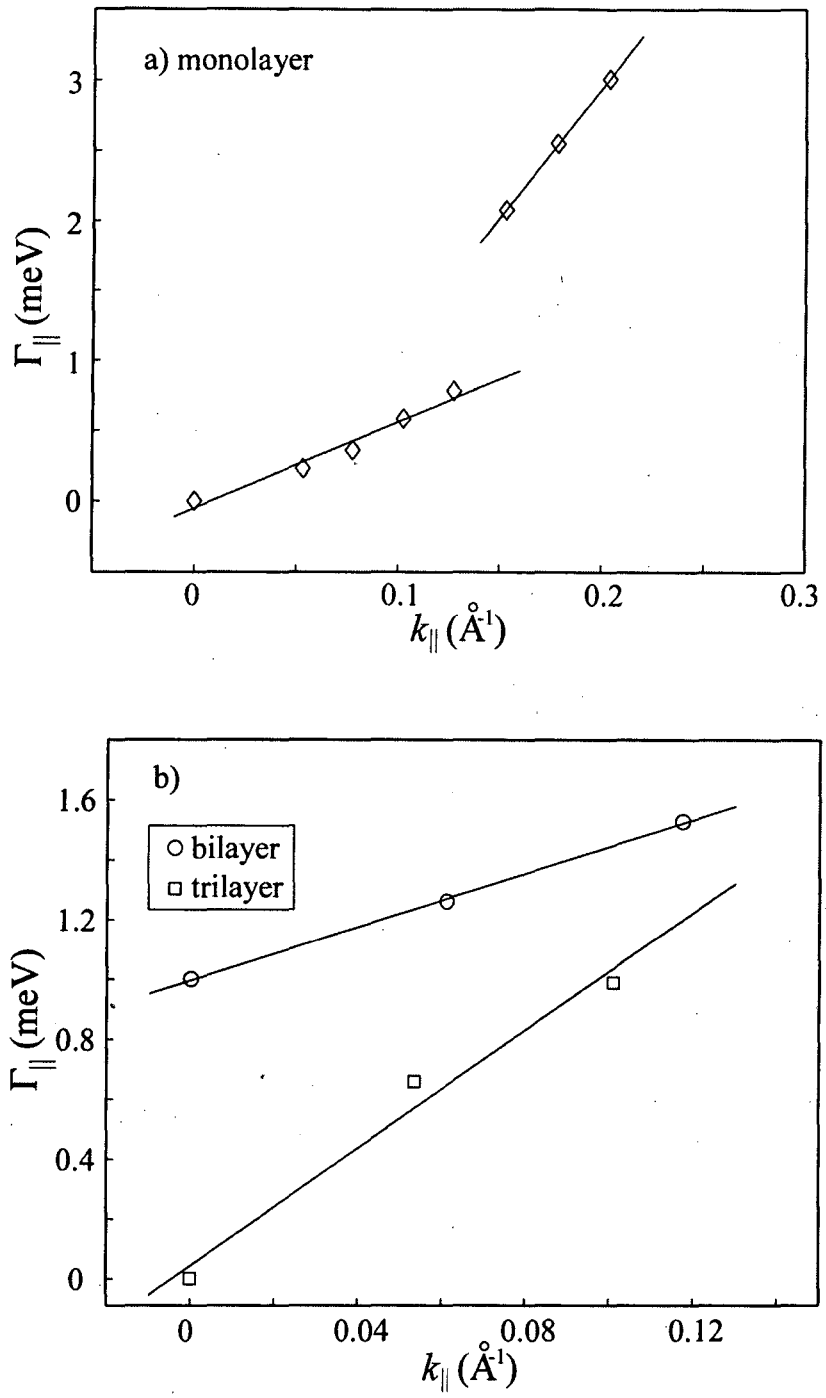

Figure 6.8. Linewidth as a function of parallel momentum of the $n = 2$ state for a monolayer, bilayer, and trilayer of Xe. The plot has a linear momentum dependence. a) The slope for the monolayer before crossing the conduction band is 6 meV·Å. After crossing the conduction band, the slope increases dramatically to 18 meV·Å. b) The slopes for a bilayer and trilayer are 4 and 10 meV·Å, respectively.

Monolayer		Bilayer		Trilayer	
$k_{\parallel}$(Å^{-1})	lifetime(fs)	$k_{\parallel}$(Å^{-1})	lifetime(fs)	$k_{\parallel}$(Å^{-1})	lifetime(fs)
0.00	251±16	0.00	336±17	0.00	186±5
0.05	230±14	0.06	296±13	0.05	156±6
0.08	220±14	0.12	264±20	0.10	145±8
0.10	205±11	-	-	-	-
0.13	193±11	-	-	-	-
0.15	140±5	-	-	-	-
0.18	128±5	-	-	-	-
0.20	117±5	-	-	-	-

Table 6.3: $n = 2$ dynamics as a function of layer thickness and parallel momentum.

Monolayer		Bilayer		Trilayer	
$k_{\parallel}$(Å^{-1})	$\Gamma_{\parallel}$ (meV)	$k_{\parallel}$(Å^{-1})	$\Gamma_{\parallel}$ (meV)	$k_{\parallel}$(Å^{-1})	$\Gamma_{\parallel}$ (meV)
0.00	0.00	0.00	0.00	0.00	0.00
0.05	0.23	0.05	0.26	0.05	0.66
0.08	0.36	0.12	0.53	0.10	0.99
0.10	0.59	-	-	-	-
0.13	0.78	-	-	-	-
0.15	2.08	-	-	-	-
0.18	2.54	-	-	-	-
0.20	3.00	-	-	-	-

Table 6.4: $\Gamma_{\parallel}$ as a function of layer thickness and parallel momentum for $n = 2$.

Using the flat potential as a representation of the Xe overlayer potential, the overlap of the image state wavefunction with both the metal and the Xe adlayer can be determined. The intraband relaxation linewidth can be broken down further into the following expression:

$$\Gamma_{\parallel} = (S_{Xe}P_{Xe} + S_{metal}P_{metal})k_{\parallel}, \tag{6.2}$$

where S_{Xe} and S_{metal} represents the intraband relaxation rate as a function of $k_{\parallel}$ as a result of the electron interaction with the Xe and the metal, respectively. The overlap of the wavefunction in the Xe overlayer and the metal are represented by P_{Xe} and P_{metal}. In Table 6.5, the normalized wavefunction overlap with the respective layer thickness for

both $n = 1$ and $n = 2$ are recorded. Because the $n = 1$ electron sees a square potential, its wavefunction penetration in the metal decreases rapidly from 1.6% to 0.07% from a monolayer to trilayer of Xe, respectively. The $n = 2$ wavefunction overlap in the metal decreases from a monolayer to a bilayer and increases again for a trilayer of Xe as the state evolve into a quantum well state. By setting the terms in parenthesis of Equation 6.2 to equal the experimentally determined slope along with the calculated wavefunction overlap, the magnitude of both S_{Xe} and S_{metal} are deduced. Since we have three equations and two unknowns, the equations were solved by means of least square under Matlab. For the $n = 1$ state, the slopes determined for S_{Xe} and S_{metal} are about 20 meV·Å and 500 meV·Å, respectively. While for $n = 2$, they are 3 meV·Å and 400 meV·Å. The slopes determined by using $n = 2$ data are least accurate due to the small number of data points.

Quantum Number n	Monolayer		Bilayer		Trilayer	
	S_{metal}	S_{Xe}	S_{metal}	S_{Xe}	S_{metal}	S_{Xe}
1	0.016	0.1245	0.0027	0.2458	0.0007	0.2987
2	0.015	0.0300	0.0100	0.1140	0.0230	0.4400

Table 6.5: Calculated wavefunction overlap in the metal substrate and Xe overlayer as a function of layer thickness for $n = 1$ and $n = 2$.

6.2.3 Electron Scattering Processes

Intraband relaxation can be caused by electron-electron, electron-phonon, and electron-defect scattering. The scattering of electrons with acoustic phonons and impurities are often termed as quasi-elastic scattering since the energy change after collision is on the order of a few meV[43]. Scattering of electrons will cause an increase in photoemission linewidths. Linewidths as a function $k_{\parallel}$ of the Cu(111) occupied surface state were measured by Kevan and coworkers[140, 141]. They found a broadening of the photoemission linewidth as a function of $k_{\parallel}$, which they attributed to a non-lifetime effect or a pure dephasing effect, an electron-impurity elastic scattering

process. Recent studies of the occupied surface state at the (111) surface of Cu, however, revealed the importance of intraband relaxation within the occupied surface state band in determining the lifetime of a hole in a surface state[110]. This study also showed that a transition from within a 2-D band is more efficient in filling a hole in the surface state band as compared to a transition from a 3-D band because of the higher wavefunction overlap among the surface states with different parallel momentum. Echenique *et al.* have discussed the possibility of electron-electron interactions, which cause momentum relaxation of image state electrons[55]. Image state electrons can interact with the high density of electrons in the metal substrate. This interaction is a Coulomb interaction, which gives rise to an Auger process and a linewidth contribution that is proportional to $k_{\parallel}^4$. The linewidth of both $n=1$ and $n=2$, however, linearly depends on $k_{\parallel}$ instead of $k_{\parallel}^4$, as shown in Figure 6.6 and Figure 6.7. For an increased number of layers, the adlayer will weaken the effect of electron-electron interaction between the image state electrons and the bulk electron density and weaken the effect of the $k_{\parallel}^4$ dependence of the line width.

Electron-defect scattering may also play an important role in the electron momentum relaxation process. Defects due to structural disorder of the Xe layer can be introduced by growing Xe at low temperatures such that the possibility of obtaining an annealed Xe layer is reduced as shown by Sanche and coworkers[142]. Structural disorder of the Xe layer may arise from vacancies in the Xe film[143]. Neutral impurity scattering in semiconductor for slow electrons have been modeled by Erginsoy[144] as scattering of electrons with hydrogen atoms. The electron mean-free-path in solid Xe which results from electron-acoustic phonon interaction can be determined using the theory developed by Conwell and Brown for lattice mobility of hot electrons in Germanium[145]. These models have been applied by Plenkiewicz *et al.* to calculate the impurity scattering and acoustic phonon scattering contributions to the electron mean-free-path in bulk Xe[143]. The energy dependence of the mean free path was implicitly accounted for by the energy dependence of the effective mass at electron energy up to 8 eV. The scattering rate calculated using the neutral impurity model is independent of the

electron energy as shown by Erginsoy[144] for electron with a constant effective mass in a given energy range.

Momentum relaxation via electron-phonon scattering can occur in the subpicosecond time scale. The efficiency of electron scattering with phonons in the bulk depends on the deformation potential, the softness of the phonon modes, and the temperature of the sample. Bulk Xe has a soft phonon mode, as indicated by its low Debye temperature of 65 K[146]. The deformation potential represents the electron-phonon coupling strength. Study of the temperature dependence of the momentum resolve $n=1$ lifetime was attempted for a monolayer of Xe. Due to the minimum attainable temperature of the experimental setup and the temperature at which the monolayer of Xe will desorb rapidly, the study was done at both 50 and 66 K. The lifetime of $n=1$ at a given parallel momentum, however, did not change in this temperature range. A larger temperature range may be required in order to distinguish the importance of electron-electron interaction versus electron-phonon interaction in determining the momentum relaxation time. This preliminary result, however, suggest that electron-phonon interaction may not be the primary momentum relaxation mechanism for the image electron. With respect to the defect scattering which may arise from the disorder in the Xe overlayer, the higher mobility of $n=1$ for three layers of Xe does not support defect scattering as being an important contribution to momentum relaxation of the image electron. As the number of layers increases, the Xe adlayer becomes more disordered as manifested in our TPPE static spectra.

The large discrepancies between S_{Xe} and S_{metal} allow us to conclude that the intraband relaxation is mainly caused by the interaction of the image state electron with the metal substrate. The Xe overlayer acts primarily as a spacer layer which reduces this interaction. Within the band gap of the metal substrate, the penetration of the wavefunction with the substrate is small. Upon crossing the conduction band, two important results are observed in the $n=2$ dynamics. The sharp rise in $\Gamma_{\parallel}$ is the consequence of leakage of carriers into the conduction band of the metal substrate. After crossing the conduction band, the slope of the intraband relaxation rate as a function of parallel momentum increases dramatically from 6 meV·Å to about 18 meV·Å. This result also revealed the sharpness of the bulk band edge. The current observations suggest that

electron-electron interaction may be the dominant mechanism in determining the momentum relaxation rate at the Xe/Ag(111) interface for image state electrons. Further theoretical investigation must be performed in order to understand the physics that governs the intraband relaxation of the image state electrons and their interaction with the metal substrate.

Chapter 7

Conclusions

This dissertation presents the studies of interband and intraband electron relaxation at the Xe/Ag(111) interface. For the purpose of comparison, the results of n-heptane on Ag(111) were also discussed. The difference in electron affinity of the two materials, whether the electron affinity is positive or negative, presents a barrier or quantum well for image state electrons depending on their energies with respect to the affinity level. The bulk properties of the dielectric, such as the static dielectric constant, conduction band minimum, and the effective mass, account for the essential physics involved in determining the interband relaxation of image electrons. The nearly free electron model is an effective model for the determination of the wavefunction overlap of the image state electron with the metal substrate. The wavefunction overlap governs both the interband and intraband electron relaxation at the Xe/Ag(111) interface. The projected bulk band structure provides the essential parameters that were used to calculate the wavefunction overlap. The main perturbation on the electronic structure of the metal substrate upon adsorption of Xe and n-heptane was regarded as minimal and was accounted by the change in the workfunction of the substrate, which in this case, moves the image states closer to the middle of the band gap. The electron dynamics is markedly different at the n-heptane/Ag(111) interface. The negative electron affinity of the n-heptane overlayer results in a barrier for the surface electrons. The polarization interaction of the image electrons with the n-heptane overlayer causes three-dimensional electron localization at the n-heptane/vacuum junction. A non-dispersive state becomes the prominent feature in the static TPPE spectra after setting the time delay between the pump and the probe pulse to about 1.7 ps. The relatively long lifetime of $n = 1 (\approx 1.3$ ps) allows the electron localization process to be observed at this interface.

The study of interband and intraband electron relaxation at interfaces requires the understanding of the electron dynamics at the clean surface. The Ag(111) surface has important characteristics that facilitates these studies. Particularly this surface exhibits an occupied surface state band, which provides a means to accurately determine the instrument function and time zero of the pump-probe laser pulses. Without these measurements, it will be impossible to deduce the lifetimes that are on the order of tens of femtoseconds since the instrument function itself is usually around 100 fs. The lifetime of the image states does not follow an n^3 lifetime dependence between the $n = 1$ state and the higher order image states. This is the result of the degeneracy of the higher image states with the conduction band. The states that are degenerate with the conduction band, however, do follow the n^3 lifetime dependence, which demonstrates that the image electrons spend most of their time out in the vacuum after excitation into the image states. The relatively long dephasing time between $n = 4$ and $n = 5$ of about 400 fs as measured via quantum oscillations confirms the above observations. The number of round trips between the image potential and the metal surface for the higher order image electrons is about an order of magnitude lower than for the $n = 1$ electron. Since $n = 1$ resides in the band gap, the surface reflectivity is increased for this state as compared to the higher order image states.

The interband relaxation times of image state electrons were measured for up to 6 layers of Xe. The layer-by-layer growth provides the opportunity to study the effects of quantum confinement on electron dynamics. The oscillations in the higher order image state electrons is a direct manifestation of the quantum confinement effects on electron dynamics at interfaces. For the $n = 1$ state, however, the interband relaxation time approaches a value of around 800 fs. The flat potential model, in this case, cannot account for this asymptotic lifetime of the $n = 1$ state at higher coverage. Instead the dielectric continuum model shows that electrons in this state can be one dimensionally localized near the surface by a screened image potential in the Xe overlayer. The lifetime of the higher order image states reaches a minimum upon the crossing of the overlayer boundary with a node in the image state electron wavefunction. This results in the observation of a single minimum lifetime value for $n = 2$ upon increasing the coverage. For $n = 3$, which has two nodes, a second minimum was not observed since this will

require lifetime measurements for up to 7 or 8 layers of Xe. At such high coverage, the Xe layer is no longer ordered and different coverage will intersperse throughout the surface. The spectral congestion corresponding to different layers for the higher order image states will make analysis and interpretation of the lifetimes above 6 layers of Xe impossible. After observing the minimum lifetime for the quantum well states, subsequent increase in the lifetime as a function of layer thickness results from the spreading of the probability density in the overlayer. These processes affect the wavefunction probability density in the metal substrate. The lifetime, as discussed in Chapter 5, is also dependent on the energy of the states with respect to the Fermi level. Linewidth measurements of bulk electronic states reveal that the lifetime is inversely proportional to the energy of the state[66].

The lifetime of image state electrons shows strong parallel momentum dependence. The analysis of the wavefunction penetration away from the Brillouin zone center cannot account for the decrease in the lifetime as a function of parallel momentum of the image states for the small $k_{\parallel}$ values of less than $0.25\,\text{Å}^{-1}$ in this study. The lifetimes of both $n=1$ and $n=2$ for a monolayer, bilayer, and trilayer of Xe were measured at various sample angles to study electron momentum relaxation as a function of layer thickness. The decay pathways for the states were assumed to arise from intraband relaxation and interband relaxation, where the rate for the latter process can be determined by measuring the lifetimes at $k_{\parallel}=0$ Å^{-1}. It is shown that the $n=1$ electrons are scattered less effectively with increasing Xe layer thickness. The effectiveness in the scattering of $n=2$ shows an increase between a bilayer and trilayer of Xe. The non-monotonic decrease in the slope of $\Gamma_{\parallel}$ versus $k_{\parallel}$ is the result of electron confinement in the Xe overlayer of $n=2$. The sudden decrease in the $n=2$ lifetime at around $k_{\parallel}=1.5$ Å^{-1} is the result of the crossing of the image state band with the Ag(111) conduction band. After the crossing of the band, the slope of $\Gamma_{\parallel}$ versus $k_{\parallel}$ increases by a factor of three. The analysis of the wavefunction overlap with both the Xe and the metal substrate as a function of layer thickness for $n=1$ and $n=2$ reveals that the Xe primarily acts as a spacer layer which reduces electron scattering. The momentum relaxation is currently

attributed to electron-electron interaction between the image electrons and the electrons in the bulk of the metal.

In the past, linewidth analysis in static TPPE and inverse photoemission spectra were used to estimate the lifetime of image states. Both surface contamination and disorder, however, contribute to inhomogeneous spectral broadening, a broadening with a Gaussian functional form, which complicates the extraction of the relaxation dynamics of the surface electrons via linewidth analysis. Momentum dependent electron dynamics were also analyzed through linewidth measurements, which exhibit further complications from the variation of the detector width with electron kinetic energy. Momentum-resolved femtosecond TPPE is a power technique that can directly measure the electron dynamics of unoccupied surface states at interfaces. This technique along with the ability to grow thin layers of insulating materials on the surface provide a unique opportunity to study the evolution of the electronic band structure and electron dynamics as a function of layer thickness. It is shown that the confinement of the electrons in a Xe quantum well causes unexpected results in both the interband and intraband relaxation of surface electrons. By using this technique, the time scale of three-dimensional localization of surface electrons can also be directly measured. The image state electrons are sensitive probes of the interfacial electronic band structures. The change in the interfacial electronic band structures is manifested in both the binding energies and the lifetimes of the image electrons. By studying the change in the binding energies and lifetimes of the image state progression, it is demonstrated that the shape of the potential can be determined. Femtosecond TPPE can also be utilized to study coherent dephasing of surface electrons. Quantum oscillations were also observed at the Xe/Ag(111) interface for a bilayer and trilayer of Xe. These oscillations do not appear at a higher coverage since the surface becomes disordered. Other investigations, such as the mapping of unoccupied bands at chemisorbed alkane-thiol metal interfaces and the study of two-dimensional electron solvation at the alcohol/metal interfaces are currently underway in our laboratory. These studies further demonstrate the power and versatility of the momentum-resolved femtosecond TPPE technique.

References

[1] Drummond, T. J.; Masselink, W. T.; Morkoç, H. *Proc. IEEE*, **1986**, *74*, 773.

[2] Avouris, P.; Walkup, R. E. *Annu. Rev. Phys. Chem.* **1989**, *40*, 173.

[3] Ho, W. *J. Phys. Chem.* **1996**, *100*, 13 050.

[4] Busch, D. G.; Gao, S.; Pelak, R. A.; Booth, M. F.; Ho, W. *Phys. Rev. Lett.* **1995**, *75*, 673.

[5] Bonn, M.; Funk, S.; Hess, Ch.; Denzler, D. N.; Stampfl, C.; Scheffler, M.; Wolf, M.; Ertl, G. *Science* **1999**, *285*, 1042.

[6] Prybyla, J. A.; Tom, H. W. K.; Aumiller, G. D. *Phys. Rev. Lett.* **1992**, *68*, 503

[7] Gadzuk, J. W. *Phys. Rev. Lett.* **1996**, *76*, 4237.

[8] Gadzuk, J. W. *Femtochemistry* eds. Manz, J.; Woste, L. VCH: Weinheim, 1995.

[9] Y. Yang, *MRS Bulletin* **1997**, *22*, 31.

[10] Sheats, J. R.; Antoniadis, H.; Hueschen, M.; Leonard, W.; Miller, J.; Moon, R.; Roitman, D.; Stocking, A. *Science* **1996**, *273*, 884.

[11] O'Regan, B.; Grätzl, M. *Nature* **1991**, *353*, 737.

[12] Ellington, R. J.; Asbury, J. B.; Ferrer, S.; Ghost, H. N.; Sprague, J. R.; Lian, T; Nozik, A. J. *J. Phys. Chem. B* **1998**, *102*, 6455.

[13] Dai, P.; Angot, T.; Ehrlich, S. N.; Wang, S. K.; Taub, H. *Phys. Rev. Lett.* **1994**, *72*, 685.

[14] Harris, C. B.; Ge, H.-H.; Lingle, R. L., Jr.; McNeill, J. D.; Wong, C. M. *Annu. Rev. Phys. Chem.* **1997**, *48*, 711.

[15] Haight, R. *Surf. Sci. Rep.* **1995**, *21*, 275.

[16] Fauster, Th.; Steinmann, W. In Electromagnetic Wave: Recent Developments in Research; *Photonic Probes of Surfaces*; Halevi, P., Ed.; Elsevier: Amsterdam, 1995; Vol. 2, p. 347.

[17] Ueba, H. *Surf. Sci.* **1995**, *334*, L719.

[18] Bokor, J.; Storz, R.; Freeman, R. R.; Bucksbaum, P. H. *Phys. Rev. Lett.* **1986**, *57*, 881.

[19] Baeumber, M.; Haight, R. *Phys. Rev. Lett.* **1991**, *67*, 1153.

[20] Grimes, C. C.; Brown, T. R. *Phys. Rev. Lett.* **1974**, *32*, 280.

[21] Fischer, R.; Fauster, Th.; Steinmann, W. *Phys. Rev. B* **1993**, *48*, 15 496.

[22] Ortega, J. E.; Himpsel, F. J.; Haight, R.; Peale, D. R. *Phys. Rev. B* **1994**, *49*, 13859.

[23] Ge, N.-H., Wong, C. M.; Lingle, R. L., Jr.; McNeill, J. D.; Gaffney, K. J.; Harris, C. B. *Science* **1998**, *279*, 202.

[24] Ge, N.-H., Wong, C. M.; Harris, C. B. *Acc. Chem. Res.* **2000**, *33*, 111-118.

[25] Grimes, C. C.; Adams, G. *Phys. Rev. Lett.* **1979**, *42*, 795.

[26] Andrei, E. Y. *Phys. Rev. Lett.* **1984**, *52*, 1449.

[27] Ogawa, S.; Nagano, H.; Petek, H. *Phys. Rev. B* **1997**, *55*, 10 869.

[28] Schmuttenmaer, C. A.; Aeschlimann, M.; Elsayed-Ali, H. E.; Miller, R. J. D.; Mantell, D. A.; Cao, J.; Gao, Y. *Phys. Rev. B* **1994**, *50*, 8947.

[29] Aeschlimann, M.; Bauer, M.; Pawlik, S. *Chem. Phys.* **1996**, *205*, 127.

[30] Cao, J.; Gao, Y.; Miller, R. J. D.; Elsayed-Ali, H. E.; Mantell, D. A. *Phys. Rev. B* **1997**, *56*, 1099.

[31] Schoenlein, R. W.; Lin, W. Z.; Fujimoto, J. G.; Eesley, G. L.*Phys. Rev. Lett.* **1987**, *58*, 1680.

[32] Fann, W. S.; Storz, R.; Tom, H. W. K.; Bokor, J. *Phys. Rev. Lett.* **1992**, *68*, 2834.

[33] McNeill, J. D.; Lingle, R. L., Jr.; Ge, N.-H.; Wong, C. M.; Jordan, R. E.; Harris, C. B. *Phys. Rev. Lett.* **1997**, *79*, 4645.

[34] Wong, C. M., McNeill, J. D., Gaffney, K. J., Ge, N.-H., Miller, A. D., Liu, S. H., Harris, C. B. *J. Phys. Chem. B* **1999**, *103*, 282.

[35] Bokor, J.; Storz, R.; Freeman, R. R.; Bucksbaum, P. H. *Phys. Rev. Lett.* **1986**, *57*, 881.

[36] Haight, R.; Baeumler, M. *Phys. Rev. B* **1992**, *46*, 1543.

[37] Höfer, U.; Shumay, I. L.; Reuβ, Ch.; Thomann, U.; Wallauer, W.; Fauster, Th. *Science* **1997**, *277*, 1480.

[38] Fauster, Th.; Reuβ, Ch.; Shumay, I. L.; Weinelt, M. *Chem. Phys.* **2000**, *251*, 111.

[39] Aeschlimann, M.; Bauer, M.; Pawlik, S.; Weber, W.; Burgermeister, R.; Oberli, D.; Siegmann, H. C. *Phys. Rev. Lett.* **1997**, *79*, 5158.

[40] Ogawa, S.; Nagano, H.; Petek, H.; Heberle, A. P. *Phys. Rev. Lett.* **1997**, *78*, 1339.

[41] Petek, H.; Ogawa, S. *Prog. Surf. Sci.* **1997**, *56*, 239.

[42] Reuβ, Ch.; Shumay, I. L.; Thomann, U.; Kutschera, M.; Weinelt, M.; Fauster, Th.; Höfer, U *Phys. Rev. Lett.* **1999**, *82*, 153.

[43] Yu, P. Y.; Cardona, M. *Fundamentals of Semiconductors: Physics and Material Properties* Springer-Verlag: Berlin, 1995.

[44] Davison, S. G.; Stęślicka, M. *Basic Theory of Surface States*; Oxford University Press Inc.: New York, 1992.

[45] Memmel, N. *Surf. Sci. Rep.* **1998**, *32*, 91.

[46] Smith, N. V. *Phys. Rev. B* **1985**, *32*, 3549.

[47] Griffiths, D. J. *Introduction to Electrodynamics 2nd Edition*; Prentice-Hall, Inc.: New Jersey, 1989, p. 121.

[48] Landau, L. D.; Lifshiftz, E. M. *Electrodynamics of Continuous Media*; Oxford: Pergamon, 1984.

[49] Plummer, E. W.; Eberhardt, W. *Adv. Chem. Phys.* **1982**, *49*, 533.

[50] Aschroft, N. W.; Mermin, N. D. *Solid State Physics*; Saunders: New York, 1976; p. 367.

[51] Giesen, K.; Hage, F.; Himpsel, F. J.; Riess, H. J.; Steinmann, W.; Smith, N. V. *Phys. Rev. B* **1987**, *35*, 205.

[52] Fuggle, J. C.; Inglesfield, J. E., Eds., *Unoccupied Electronic States, Topics in Applied Physics* **1992**, *69*, Springer, Berlin.

[53] Smith, N. V. *Rep. Prog. Phys.* **1988**, *51*, 1227.

[54] Echenique, P. M.; Pendry, J. B. *J. Phys. C: Solid State Phys.* **1978**, *11*, 2065.

[55] Echenique, P. M.; Pendry, J. B. *Prog. Surf. Sci.* **1990**, *32*, 111.

[56] de Andrés, P.; Echenique, P. M.; Flores, F. *Phys. Rev. B* **1987**, *35*, 4529.

[57] Weinert, M.; Halbert, S. L.; Johnson, P. D. *Phys. Rev. Lett.* **1985**, *55*, 2055.

[58] Bausells, J.; Echenique, P. M.; Flores, F. *Surf. Sci.* **1987**, *178*, 268.

[59] Maue, A. W. *Z. Phys.* **1935**, *94*, 717.

[60] Goodwin, E. T. *Proc. Camb. Phil. Soc.* **1939**, *35*, 205.

[61] Goodwin, E. T. *Proc. Camb. Phil. Soc.* **1939**, *35*, 221.

[62] Townsend, J. S. *A Modern Approach to Quantum Mechanics* McGraw-Hill: New York, 1992.

[63] Straub, D.; Himpsel, F. J. *Phys. Rev. Lett.* **1984**, *52*, 1922.

[64] Giesen, K.; Hage, F. ; Himpsel, F. J. ; Riess, H. J. ; Steinmann, W. *Phys. Rev. B* **1987**, *35*, 971.

[65] de Andrés, P. L. ; Echenique, P. M. ; Flores, F. Phys. Rev. B **1989**, *39*, 10 356.

[66] Goldman, A.; Altmann, W.; Dose, V. *Solid State Commun.* **1991**, *79*, 511.

[67] Wolf, M.; Knoesel, E.; Hertel, T. *Phys. Rev. B* **1996**, *54*, R5295.

[68] Schoenlein, R. W.; Fujimoto, J. G.; Eesley, G. L.; Capehart, T. W. *Phys. Rev. Lett.* **1988**, *61*, 2596.

[69] Schoenlein, R. W.; Fujimoto, J. G.; Eesley, G. L.; Capehart, T. W. *Phys. Rev. B* **1990**, *41*, 5436.

[70] Schoenlein, R. W.; Fujimoto, J. G.; Eesley, G. L.; Capehart, T. W. *Phys. Rev. B* **1991**, *43*, 4688.

[71] Chulkov, E. V.; Sarría, I., Silkin, V. M.; Pitarke, J. M.; Echenique, P. M. *Phys. Rev. Lett.* **1998**, *80*, 4947.

[72] Lingle, R. L.; Padowitz, D. F.; Jordan, R. E.; McNeill, J. D.; Harris, C. B. *Chem. Phys.* **1996**, *205*, 191; *Chem. Phys.* **1996**, *208*, 297.

[73] Johnson, P. D.; Smith, N. V. *Phys. Rev. Lett.* **1984**, *52*, 1922.

[74] Straub, D.; Himpsel, F. J. *Phys. Rev. B* **1986**, *33*, 2256.

[75] Binnig, G.; Frank, K. H.; Fuchs, H.; Garcia, N.; Reihl, B.; Rohrer, H.; Salvan, R.; Williams, A. R. *Phys. Rev. Lett.* **1985**, *55*, 1985.

[76] Giesen, K.; Hage, F.; Himpsel, F. J.; Riess, H. J.; Steinmann, W. *Phys. Rev. Lett.* **1985**, *55*, 300.

[77] Giesen, K.; Hage, F.; Himpsel, F. J.; Riess, H. J.; Steinmann, W. *Phys. Rev. B* **1986**, *33*, 5241.

[78] Giesen, K.; Hage, F, Himpsel, F. J., Riess, H. J.; Steinmann, W. *Phys. Rev. B* **1987**, *35*, 971.

[79] Padowitz, D. F., Merry, W. R.; Jordan, R. E.; Harris, C. B. *Phys. Rev. Lett.* **1992**, *69*, 3583.

[80] Hüfner, S. *Photoelectron Spectroscopy 2nd Edition*, Springer-Verlag: Berlin, 1996.

[81] Kevan, S. D., Ed., *Angle-Resolved Photoemission,* Bd. 74 of *Studies in Surface Science and Catalysis*, Elsevier: Amsterdam, 1992.

[82] Paggel, J. J.; Miller, T.; T.-C. Chiang, *Phys. Rev. Lett.* **1998**, *81*, 5632.

[83] Paggel, J. J.; Miller, T.; T.-C. Chiang, *Science* **1999**, *283*, 1709.

[84] Luh, D.-A.; Paggel, J. J.; Miller, T.; Chiang, T.-C. *Phys. Rev. Lett.* **2000**, *84*, 3410.

[85] Shakeshaft, R.; Spruch, L. *Phys. Rev. A* **1985**, *31*, 1535.

[86] Lüth, H. *Surfaces and Interfaces of Solids*, Springer-Verlag: Berlin, 1993.

[87] Wolf, M.; Hotzel, A.; Knoesel, E.; Velic, D. *Phys. Rev. B* **1999**, *59*, 5926.

[88] Merry, W. R., Jordan, R. E.; Padowitz, D. F.; Harris, C. B. *Surf. Sci.* **1993**, *295*, 393.

[89] McNeill, J. D.; Lingle, R. L., Jr.; Jordan, R. E.; Padowitz, D. F.; Harris, C. B. *J. Chem. Phys.* **1996**, *105*, 3883.

[90] Merry, W. R. Ph.D Thesis, University of California at Berkeley, 1992.

[91]Norris, T. B. *Opt. Lett.* **1992**, *17*, 1009.

[92] Reed, M. K.; Steiner-Shepard, M. K.; Negus, D. K. *Opt. Lett.* **1994**, *19*, 1855.

[93] Unguris, J.; Bruch, L. W.; Moog, E. R.; Webb, M. B. *Surf. Sci.* **1979**, *87*, 415.

[94] Fischer, R.; Schuppler, S.; Fischer, N., Fauster Th.; Steinmann, W. *Phys. Rev. Lett.* **1993**, *70*, 654.

[95] Fischer, R.; Fauster, Th.; Steinmann, W. *Phys. Rev. B* **1993**, *48*, 15 496.

[96] Fischer, R; Fauster, Th. *Phys. Rev. B* **1995**, *57*, 7112.

[97] Wallauer, W; Fauster, Th. *Surf. Sci.* **1995**, *333*, 731.

[98] Lingle, R. L., Jr.; Padowitz, D. F.; Jordan, R. E.; McNeill, J. D., Harris, C. B. *Phys. Rev. Lett.* **1994**, *72*, 2243.

[99] Firment, L. E.; Somorjai, G. A. *J. Chem. Phys.* **1978**, *69*, 3940.

[100] Pendry,J. B. *Photoemission and the Electronic Properties of Surfaces*, ed. Feuerbacher, B.; Fitton, B., Willis, R. F., Wiley: New York, 1978.

[101] Smith, N. V.; Thiry, P.; Petroff, Y. *Phys. Rev. B* **1993**, *47*, 15 476.

[102] Barkhuysen, H.; De Beer, R.; Deogendijk, A. C.; Van Ormondt, D., Van Der Veen, J. W. C. *Quantitative Analysis of NMR Signals in the Time Domain.*

[103] Press, W. H.; Teukolsky, S. A.; Vetterling, W. T.; Flannery, B. P. *Numerical Recipes in C: The Art of Scientific Computer 2nd Edition* **1992**, Cambridge University Press: New York Chapter 2.

[104] McNeill, J. D.; *Ultrafast Dynamics of Electrons at Interfaces*, Ph.D. Thesis, University of California at Berkeley, 1999.

[105] Knoesel, E., Hotzel, A., Wolf, M. *J. Electron Spectrosc. Relat. Phenom.* **1998**, *88-91*, 577.

[106] Cole, M. W. *Phys. Rev. B* **1971**, *3*, 4418.

[107] Datta, S. *Electronic Transport in Mesoscopic Systems*, Cambridge University Press: New York, 1995.

[108] Shumay, I. L.; Höfer, U.; Reuβ, Ch.; Thomann, U., Wallauer, W., Fauster, Th. *Phys. Rev. B* **1998**, *58*, 13 974.

[109] Chulkov, E. V.; Silkin, V. M.; Echenique, P. M. *Surf. Sci.* **1997**, *391*, L1217.

[110] Osma, J.; Sarría, I.; Chulkov, E. V., Pitarke, J. M.; Echenique, P. M. *Phys. Rev. B* **1999**, *59*, 10 591.

[111] Palmer, R. E. *Prog. Surf. Sci.* **1992**, *41*, 51.

[112] Borisov, A. G.; Kazansky, A. K.; Gauyacq, J. P. *Phys. Rev. Lett.* **1998**, *80*, 1996.

[113] Guillemot, L.; Esaulov, V. A. *Phys. Rev. Lett.* **1999**, *82*, 4552.

[114] Nauenberg, M.; *Sci. Am.* **1994**, *270*, 24.

[115] Diels, J.-C.; Wolfgang, R. *Ultrashort Laser Pulse Phenomena*, Academic Press: San Diego, 1996, Chapter 4.

[116] Loudon, R. *The Quantum Theory of Light*, 1983, Oxford University Press: New York.

[117] Hertel, T., Knoesel, E., Wolf, M., Ertl, G. *Phys. Rev. Lett.* **1996**, *76*, 535.

[118] Slichter, C. P. *Principles of Magnetic Resonance 3rd Edition*, Springer-Verlag: Berlin, 1996, page 199.

[119] Schwentner, N.; Himpsel, F.-J.; Saile, V.; Skibowski, M.; Steinmann, W.; Koch, E. E. *Phys. Rev. Lett.* **1975**, *34*, 528.

[120] Allen, A. O. *Drift Mobilities and Conduction Band Energies of Excess Electrons in Dielectric Liquids*, NBS Report No. NSRDS-NBS 58, U.S. Department of Commerce, 1976.

[121] Cole, M. W.; Cohen, M. H. *Phys. Rev. Lett.* **1969**, *23*, 1238.

[122] Jackson, J.D. Private Communication.

[123] Ge, N. –H..; *Ultrafast Studies of Electron Dynamics at Metal-Dielectric Interfaces*, Ph.D. Thesis, University of California at Berkeley, 1998 and references therein.

[124] Gaffney, K. J.; Wong, C. M.; Liu, S. H.; Miller, A. D.; McNeill, J. D.; Harris, C. B. *Chem. Phys.* **2000**, *251*, 99.

[125] Sheats, J. R.; Antoniadis, H.; Hueschen, M.; Leonard, W.; Miller, J.; Moon,r.; Roitman, D.; Stocking, A. *Science* **1996**, *273*, 884.

[126] Ando, T.; Arakawa, Y.; Furuya, K.; Komiyama, S., Nakashima, H. *Mesoscopic Physics and Electronics*, Springer-Verlag: Berlin, 1998.

[127] Song, K. S.; Williams, R. T. *Self-Trapped Excitons, 2nd Edition*, Spring-Verlag: Berlin, 1996.

[128] Alexandrov, A. S.; Mott, S. N. *Polarons and Bipolarons*, World Scientific: Massachussets, 1995.

[129] Chandler, D.; Leung, K. *Annu. Rev. Phys. Chem.* **1994**, *45*, 557.

[130] Shluger, A. L.; Stoneham, A. M. *J. Phys.: Condens. Matter* **1993**, *5*, 3049.

[131] Emin, D. *Phys. Today* **1982**, *35*, 34.

[132] Marcus, R. A.; Sutin, N. *Biochimica et Biophysica Acta.* **1985**, *811*, 265.

[133] Sommer, W. T.; Tanner, D. J. *Phys. Rev. Lett.* **1971**, *27*, 1345.

[134] Williams, R.; Crandall, R. S.; Willis, A. H. *Phys. Rev. Lett.* **1971**, *26*, 7.

[135] Brown, T. R.; Grimes, C. C. *Phys. Rev. Lett.* **1972**, *29*, 1233.

[136] Cole, M. W. *Phys. Rev. B* **1970**, *2*, 4239.

[137] Cole, M. W. *Rev. Mod. Phys.* **1974**, *46*, 451.

[138] Troyanovskiĭ, A. M.; Khaĭkin, M. S. *Sov. Phys. JETP* 1981, *54*, 214.

[139] Stern, F.; Howard, W. E. *Phys. Rev.* **1967**, *163*, 816.

[140] Kevan, S. D. *Phys. Rev. Lett.* **1983**, *50*, 526.

[141] Tersoff, J.; Kevan, S. D. *Phys. Rev. B* **1983**, *28*, 4267.

[142] Bader, G.; Perluzzo, G.; Caron, L. G.; Sanche, L. *Phys. Rev. B* **1982**, *26*, 6019.

[143] Plenkiewicz, B.; Plenkiewicz, P.; Jay-Gerin, J.-P. *Phys. Rev. B* **1986**, *33*, 5744.

[144] Erginsoy, C. *Phys. Rev. B* **1950**, *79*, 1013.

[145] Conwell, E. M.; Brown, A. L.; *J. Phys. Chem. Solids* **1960**, *15*, 208.

[146] Kittel, C *Introduction to Solid State Physics*, Wiley: New York, 1986.

Ernest Orlando Lawrence Berkeley National Laboratory
One Cyclotron Road | Berkeley, California 94720

Prepared for the U.S. Department of Energy under Contract No. DE-AC03-76SF00098